



**HAL**  
open science

# Strain fields measurements to study the nonlinear mechanical behaviour of refractory materials

Younès Belrhiti

► **To cite this version:**

Younès Belrhiti. Strain fields measurements to study the nonlinear mechanical behaviour of refractory materials. Materials. Université de Limoges, 2015. English. NNT : 2015LIMO0128 . tel-01362983

**HAL Id: tel-01362983**

**<https://theses.hal.science/tel-01362983>**

Submitted on 9 Sep 2016

**HAL** is a multi-disciplinary open access archive for the deposit and dissemination of scientific research documents, whether they are published or not. The documents may come from teaching and research institutions in France or abroad, or from public or private research centers.

L'archive ouverte pluridisciplinaire **HAL**, est destinée au dépôt et à la diffusion de documents scientifiques de niveau recherche, publiés ou non, émanant des établissements d'enseignement et de recherche français ou étrangers, des laboratoires publics ou privés.

# UNIVERSITE DE LIMOGES

ECOLE DOCTORALE Science et Ingénierie en Matériaux, Mécanique,

**Energétique et Aéronautique SI-MMEA (522)**

Science des procédés céramiques et de traitements de surface

Thèse

pour obtenir le grade de

DOCTEUR DE L'UNIVERSITÉ DE LIMOGES

Discipline / Spécialité : Matériaux céramiques et traitements de surface

Présentée et soutenue par

**Younès BELRHITI**

le 09/12/2015

## **Etude de matériaux réfractaires à comportement mécanique non linéaire par mesure de champs de déformations**

**Thèse dirigée par:** M. Thierry CHOTARD et M. Marc HUGER

**Co-encadrée par:** M. Octavian POP

### **JURY:**

#### **Président du jury**

M. Thierry CUTARD, Professeur des universités, ICA Albi (ICAA), Ecole des Mines d'Albi (France)

#### **Rapporteurs**

M. Zoheir ABOURA, Professeur des universités, Roberval UMR 7337, Université de Technologie de Compiègne (France)

M. Alain GASSER, Professeur des universités, PRISME, Polytech Orléans (France)

#### **Examineurs**

M. Thierry CHOTARD, Professeur des universités, SPCTS UMR 7315, Université de Limoges (France)

M. Pascal DOUMALIN, Maître de conférences, PPRIME, ENSMA, Université de Poitiers (France)

M. Renaud GRASSET-BOURDEL, Dr. Ingénieur R&D, RHI Leoben (Autriche)

M. Marc HUGER, Professeur des universités, SPCTS UMR 7315, Université de Limoges (France)

M. Octavian POP, Maître de conférences HDR, GEMH, Université de Limoges (France)



# UNIVERSITE DE LIMOGES

ECOLE DOCTORALE Science et Ingénierie en Matériaux, Mécanique,

**Energétique et Aéronautique SI-MMEA (522)**

Science of Ceramic Processing and Surface Treatments

Thesis

submitted for the degree of

DOCTOR OF PHILOSOPHY OF THE UNIVERSITY OF LIMOGES

Discipline: Ceramic Materials and Surface Treatment

Presented by

**Younès BELRHITI**

09/12/2015

## **Strain fields measurements to study the nonlinear mechanical behaviour of refractory materials**

**Supervised by:** M. Thierry CHOTARD, M. Marc HUGER

**Co-supervised by:** M. Octavian POP

### **JURY:**

#### **President**

M. Thierry CUTARD, Professor, ICA Albi (ICAA), Ecole des Mines d'Albi (France)

#### **Reviewers**

M. Zoheir ABOURA, Professor, Roberval UMR 7337, University of Technology of Compiègne (France)

M. Alain GASSER, Professor, PRISME, University of Orléans (France)

#### **Examiners**

M. Thierry CHOTARD, Professor, SPCTS UMR 7315, University of Limoges (France)

M. Pascal DOUMALIN, Lecturer, PPRIME, University of Poitiers (France)

M. Renaud GRASSET-BOURDEL, Dr. R&D Engineer, RHI Leoben (Austria)

M. Marc HUGER, Professor, SPCTS UMR 7315, University of Limoges (France)

M. Octavian POP, Lecturer, HDR, GEMH, University of Limoges (France)

*A ma famille*

# Acknowledgments

This PhD work has been accomplished in the Science of Ceramic Processing and Surface Treatments laboratory (SPCTS - UMR CNRS 7315). I gratefully acknowledge the director of the SPCTS laboratory Professor Thierry Chartier for giving me the opportunity to realize this work in the SPCTS laboratory.

This great experience was realized in the framework of FIRE project D (Federation for International Refractory Research and Education) entitled: “Refractories with enhanced flexibility for thermal shock” through collaboration with RWTH Aachen University (Germany), ALTEO (France), RHI (Austria), TATASTEEL (Netherland) and TENARIS (Argentina). I would like to express my utmost gratitude for all members of the project.

I would like to express my deep gratitude to M. Pascal Doumalin, M. Jean Christophe Dupré and M. Arnaud Germaneau for welcoming me into their research team Photomechanics & Experimental Analysis in Solid Mechanics (PEM) in the Pprime institute of Poitiers (France) and for their strong contribution to the achievement of this thesis.

I am grateful for all members of the jury and especially Professor Thierry Cutard (*Ecole des Mines d’Albi*) for being a president of the jury, Professor Zoheir Aboura (University of Technology in Compiègne) and Professor Alain Gasser (University of Orléans) for accepting to be the reviewers of my work.

I would like to thank my supervisors who had the idea to propose this new thematic of research in the SPCTS, who trusted me to carry out this project and directed the work:

I want to express a deep sense of thanks and gratitude to the director of my PhD, Professor Marc Huger (Leader of FIRE project D - SPCTS) for giving me the opportunity to undertake this project and his confidence, for providing me with the greatest support advice, for his scientific rigor and for the constructive comments during the writing of the manuscript of the thesis.

I am indebted to the co-director of my PhD, Professor Thierry Chotard (Leader of FIRE project D - SPCTS) for his guidance, encouragement and helpful criticism in my write-up. For his help in various scientific and administration aspects.

I also acknowledge Dr. Octavian Pop (University of Limoges), who shared his passion of research during this work. I am grateful for his various remarks, wise advices, and for his great scientific and human qualities.

I would like to thank also all the staff of the SPCTS laboratory and the ENSCI for their help. I am grateful to the region of Limoges for the financial support.

These years of PhD wouldn't be the same without my friends and colleagues with whom I shared memorable moments: Adel, Amine, Andrey, Anthony, Arnaud, Charles, Cyril, Daniel, Danièle, Diane, Emilie, Fabrice, Fahouzi, Fanny, Fateh, Hervé, Ibrahim, Ismail, Jean-Michel, Joseph, Lucas, Mickaël, Mouna, Najet, Renaud, Youssef ...

Last but not least, I would like to thank my mother Lalla Khadija, my father Moulay Ismail, my dear sisters Maryam, Fatima-Zahra, my dear brother Zakaria and all members of my family for their encouragement and support.

# Table of Content

<b>General introduction.....</b>	<b>1</b>
<b>Chapter I: State of the art concerning the non-linear mechanical behaviour of refractory materials and the measurement techniques for kinematic fields .....</b>	<b>4</b>
<b>I. Introduction .....</b>	<b>5</b>
<b>II. Thermal shock resistance and non-linear mechanical behaviour of refractories .....</b>	<b>6</b>
<b>II.1. Origin of thermal stresses.....</b>	<b>6</b>
<b>II.2. Crack growth process in refractories submitted to a thermal shock.....</b>	<b>8</b>
II.2.1. Crack growth mechanisms .....	9
II.2.2. Energetic approach.....	11
II.2.3. R-curve approach .....	13
<b>III. Optical and numerical approaches in mechanical characterization of refractories .....</b>	<b>15</b>
<b>III.1. Optical methods .....</b>	<b>16</b>
III.1.1. Digital image correlation.....	16
III.1.2. Mark tracking method .....	19
III.1.3. Accuracy of kinematic measurements and sources of errors.....	20
<b>III.2. Finite element method updating (FEMU): identification of material properties .....</b>	<b>21</b>
III.2.1. Introduction to identification methods .....	21
III.2.2. Finite element method updating .....	22
<b>IV. Conclusion .....</b>	<b>24</b>
<b>Chapter II: Experimental techniques and materials selection .....</b>	<b>26</b>
<b>I. Introduction .....</b>	<b>27</b>
<b>II. Determination of elastic properties: Ultrasonic technique at room temperature .....</b>	<b>27</b>
<b>III. Characterization of mechanical behaviour .....</b>	<b>29</b>
<b>III.1. Four-points bending test.....</b>	<b>29</b>
<b>III.2. Brazilian test.....</b>	<b>32</b>
<b>III.3. Wedge splitting test .....</b>	<b>36</b>
<b>IV. Application of optical methods .....</b>	<b>39</b>
<b>IV.1. Digital image correlation .....</b>	<b>39</b>
IV.1.1. Sample preparation.....	40
IV.1.2. Image acquisition .....	42
IV.1.3. Images treatment .....	43
IV.1.4. Experimental key points .....	44
<b>IV.2. Mark tracking method.....</b>	<b>48</b>
<b>V. Materials selection .....</b>	<b>50</b>
<b>V.1. Why flexible ceramics? .....</b>	<b>50</b>
<b>V.2. Aluminum titanate as a model flexible refractory.....</b>	<b>51</b>
<b>V.3. Industrial flexible magnesia refractories .....</b>	<b>53</b>

V.3.1.	Materials containing spinel .....	53
V.3.2.	Magnesia spinel refractories.....	54
V.3.3.	Magnesia hercynite refractories .....	55
V.3.4.	Magnesia carbon refractories .....	55
<b>VI.</b>	<b>Conclusion .....</b>	<b>57</b>

**Chapter III: First application of DIC for the non-linear mechanical characterization of a model material : “very flexible aluminium titanate” .....** **58**

<b>I.</b>	<b>Introduction .....</b>	<b>59</b>
<b>II.</b>	<b>AT as model material of flexible refractories .....</b>	<b>59</b>
II.1.	Flexible AT preparation .....	59
II.2.	AT VF microstructure characterization .....	61
<b>III.</b>	<b>The application of DIC to investigate the non-linear mechanical behaviour of AT VF .....</b>	<b>64</b>
III.1.	Introduction.....	64
III.2.	Mechanical behaviour.....	65
III.3.	Asymmetric behaviour .....	67
III.4.	Neutral fibre evolution.....	70
III.5.	Stress-strain behaviour.....	73
III.6.	Energetic approach .....	75
III.7.	Bending device behaviour.....	76
<b>IV.</b>	<b>Conclusion .....</b>	<b>78</b>

**Chapter IV: Application of DIC to characterize the non-linear mechanical behaviour of industrial refractories : case of magnesia based materials .....** **80**

<b>I.</b>	<b>Introduction .....</b>	<b>81</b>
<b>II.</b>	<b>Analysis of spinel addition influence on fracture mechanisms in magnesia spinel refractories using DIC.....</b>	<b>81</b>
II.1.	Magnesia spinel materials description .....	81
II.2.	Non-linear mechanical behaviour of magnesia spinel refractories.....	85
II.2.1.	Load-displacement curves obtained by WST.....	85
II.2.2.	Energy and fracture analysis .....	86
II.2.3.	DIC as an efficient tool to bring out fracture mechanisms during WST .....	89
<b>III.</b>	<b>The non-linear behaviour of magnesia hercynite refractories .....</b>	<b>94</b>
III.1.	Microstructure characterization.....	94
III.2.	Mechanical behaviour using DIC at room temperature.....	97
III.2.1.	Four-points bending test.....	97
III.2.2.	Brazilian test.....	98
III.2.3.	Wedge Splitting test .....	105
<b>IV.</b>	<b>Conclusion .....</b>	<b>108</b>

<b>Chapter V: Finite element method updating: an approach to identify material properties</b>	<b>110</b>
<b>I. Introduction</b>	<b>111</b>
<b>II. Global approach of FEMU-U</b>	<b>111</b>
<b>III. Numerical implementation</b>	<b>112</b>
<b>III.1. Selection of numerical tools</b>	<b>112</b>
<b>III.2. From experimental geometry to FEM simulation</b>	<b>112</b>
<b>III.3. Pertinence of DIC results using control cards</b>	<b>114</b>
<b>III.4. Objective function</b>	<b>115</b>
<b>III.5. Newton Raphson optimization method</b>	<b>117</b>
<b>IV. Applications</b>	<b>121</b>
<b>IV.1. Case of aluminium</b>	<b>121</b>
<b>IV.2. Case of AT VF sample</b>	<b>123</b>
<b>V. Conclusion</b>	<b>127</b>
<b>Conclusion and perspectives</b>	<b>128</b>
<b>Appendixes</b>	<b>132</b>
<b>Appendix A</b>	<b>132</b>
<b>Appendix B</b>	<b>135</b>
<b>Appendix C</b>	<b>140</b>
<b>Publications and presentations</b>	<b>143</b>
<b>References</b>	<b>144</b>

# General introduction

Refractory materials are present in a large panel of industrial applications due to their specific properties. They are applied in several parts of many installations designed to face severe working environments such as high temperature, corrosion and thermal shock solicitations. Among the required properties, thermal shock resistance is a key parameter to enhance their service life. This thermal shock resistance is usually directly related to a specific mechanical behaviour induced by a voluntary micro-cracked microstructure. Indeed, depending on micro-cracking level, the mechanical behaviour will change from pure elastic to a “non-linear” one.

In order to accurately determine constitutive laws for such materials to feed finite element method (FEM), it was necessary, during the past 15 years, to develop uniaxial tests taking into account that these materials are characterized by a low level of strain-to-rupture. Nowadays, accurate instrumented tensile test using extensometers are available. However, such tensile devices involve some complexity for tests management (sample machining and well aligned loading grips). Fortunately, the occurrence of optical techniques such as digital image correlation (DIC) which allows to obtain the overall strain fields on a given loaded sample, coupled to FEM modelling, give today new opportunities for experimental investigations of refractory materials exhibiting a non-linear mechanical behaviour.

In this context, the main objective of the present PhD was to enrich the mechanical characterization of refractory materials by evaluating the efficiency of DIC applied on quite common mechanical tests in this scientific community: such as four-points bending test, Brazilian test and Wedge splitting test. For this purpose, it was necessary first for SPCTS laboratory to master this new DIC measurement tools and to apply them on refractory materials which exhibit low level of strain-to-rupture.

This research activity has been developed in the framework of the Federation for International Refractory Research and Education (**F.I.R.E**) which aims to promote a worldwide collaboration between academic institutes and industrial companies to pool the expertise at master and PhD levels in the field of refractories. In this purpose, multi-partners programs are regularly launched to support research activities. The present PhD (funded by the region of Limoges) has been part of F.I.R.E project D which took place between 2011 and



2014 and which was devoted to “dense refractories with enhanced flexibility for thermal shock”. This research program was organized through a collaboration between two laboratories (**SPCTS-Limoges-France**, **RWTH-Aachen-Germany**) and four industrial partners (**Alteo-France**, **RHI-Austria**, **Tatasteel-Netherland** and **Tenaris-Argentina**).

Even if the objective of the present PhD was to apply DIC techniques to refractory characterization, one should note here that absolutely no DIC expertise was present at SPCTS laboratory before the present work. Thus, in addition to the previously indicated partnerships, and in order to take advantage of the great expertise in photo-mechanics which has been developed for many years in Pprime Institute-Poitiers, a close collaboration has been also established with these colleagues. Nevertheless, due to the very low level of strain-to-rupture of refractory materials, it has been necessary to improve DIC techniques for our own purpose.

The first chapter is dedicated to establish the state of the art concerning thermal shock of refractories and non-linear behaviour by mechanical and energetic approaches. Then, optical methods used to complete the mechanical investigation of refractories such as DIC and mark tracking method have been introduced. Besides, in order to overcome the problem of mechanical characterization of the non-linear behaviour, kinematic fields obtained by DIC are conjugated to FEM in the framework of the identification technique by finite element method updating (FEMU-U).

The chapter II aims to present different experimental characterization techniques. The mechanical ones are associated to optical methods which are here described in details. Then, the studied materials chosen in order to develop and to valid efficiency of DIC are introduced. Among these materials, a model one based on aluminium titanate (AT) developed for academic purposes, and some industrial ones based on magnesia spinel systems delivered by industrial partners.

The main objective of the first investigation, detailed in chapter III, is to demonstrate the efficiency of the DIC technique as an effective tool to complete the mechanical analysis of refractory materials. This first study highlights the specific non-linear mechanical behaviour of AT during four-points bending test at room temperature.

In chapter IV, the acquired DIC expertise has been used to complete the characterization of industrial magnesia spinel refractories. Even if spinel inclusions are used

to promote micro-cracking by thermal expansion mismatch with the magnesia matrix, the low level of flexibility of these industrial materials which is less accentuated than AT, pushed us to improve the accuracy of DIC measurements.

After having studied experimentally the non-linear mechanical behaviour of several refractories, chapter V is dedicated to the numerical development of FEMU-U for linear elastic behaviour materials under four-points bending test, then, the developed approach has been applied for flexible AT materials.

# Chapter I

State of the art concerning the non-linear mechanical  
behaviour of refractory materials and the measurement  
techniques for kinematic fields

## I. Introduction

Refractories, widely used in many industrial areas such as steel, cement, lime, non-ferrous metals and glass processing, are known for their ability to resist to high temperature loading and to sustain, in the same time, significant levels of mechanical stress and strain. These materials can also develop improved resistance against corrosion mechanisms to face their severe working environments. In a same way, the knowledge concerning their thermal shock resistance, but more specifically, their thermal shock behaviour is of prime importance to enhance lifetime. This property of thermal shock resistance is known to be closely related to the crack growth behaviour of such materials. Consequently, the occurrence of a significant micro-cracked network within the material will lead to the change in the mechanical behaviour, from pure elastic to a “non-linear” one as well as the level of strain increases. Until today, the characterization of this non-linear behaviour in many cases is still done using classical mechanical techniques which identify some parameters thanks to equation that are only valid for materials whose behaviour is pure elastic. That is why, the occurrence of optical methods for kinematic fields’ measurement and numerical methods is considered as a promising support for allowing to perform the characterization of materials with such specific non-linear behaviours.

The following items will detail and present initially the relationships between the onset of micro cracking, the induced mechanical behaviour and the thermal shock resistance. Secondly, a gathering and a discussion of the applied techniques to measure the kinematic fields for the investigation of the specific “non-linear behaviour” of these materials will be done.

## II. Thermal shock resistance and non-linear mechanical behaviour of refractories

### II.1. Origin of thermal stresses

Thermal stresses is a well-known phenomenon and its influence on ceramics has been highlighted for a long time (Norton, 1925). In this paragraph, some sources of thermal stresses are described and detailed.

Firstly, for a homogeneous, isotropic sample completely restrained from expanding by application of restraining forces, when temperature rises from  $T_0$  to  $T_1$ , stresses appear and arise. According to Kingery (Kingery, 1955), the expression of these stresses in the case of two dimensional solid is:

$$\sigma = -\frac{E.\alpha.(T_1 - T_0)}{(1 - \nu)} \quad \text{Eq. I-1}$$

where  $E$  is Young's modulus,  $\alpha$  is the thermal expansion coefficient and  $\nu$  is Poisson ratio of material.

Secondly, for multi-phased (heterogeneous) materials constituted by crystals with anisotropic behaviour at a uniform temperature, stresses will occur due to the difference of thermal expansion between phases or between crystal's directions. The magnitude of stresses will depend on elastic properties and  $\alpha$  of components in different directions. These stresses have been investigated in connection with material's properties and can lead to serious weakening or fracture in extreme cases (Laszlo, 1943; Buessem et al., 1952). At a larger scale, a similar effect can be observed for example between enamel and the ceramic substrate.

Heterogeneous material's behaviour is difficult to describe because of the presence of numerous mechanisms taking place at the same time during heating or cooling. To clarify this, the most convenient approach consists on simplifying the microstructure to two isotropic constituents only: two phases materials obtained by sintering step and composed of a matrix (m) and spherical inclusions (i). Matrix and inclusions are constituted of two different isotropic phases. Depending on the thermal expansion mismatch between the two phases

( $\Delta\alpha = \alpha_m - \alpha_i$ ) and on the microstructure, three different configurations are possible when a sample is cooled to room temperature (Figure I-1).

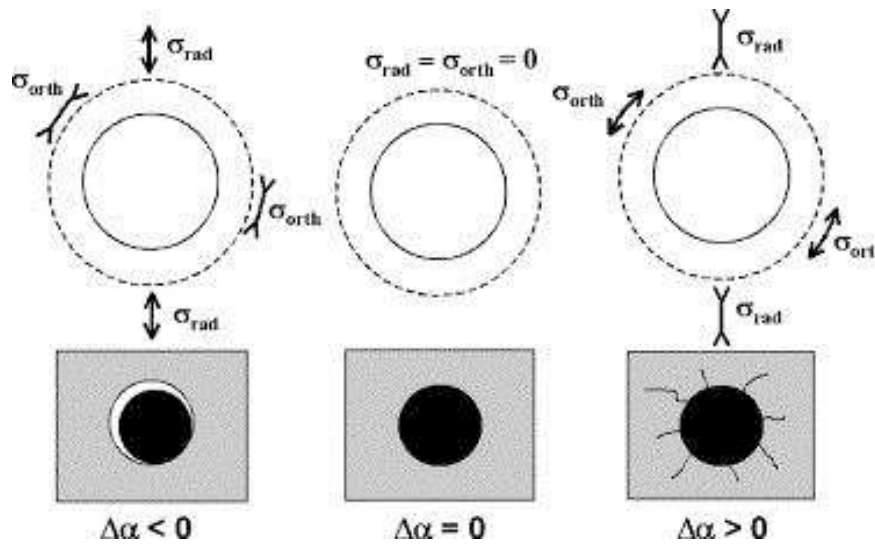


**Figure I-1: Different configurations of internal thermal stresses field which can occur according to  $\alpha$  differential between the two phases of a glass alumina sintered materials (Tessier-Doyen et al., 2006)**

- $\Delta\alpha = 0$  (quite thermal expansion coefficient equality), the inclusion and matrix are subjected to the same strain state, and so no internal stress appears during cooling, and thus, no damage is observed.
- $\Delta\alpha < 0$ , a debonding of the interface can occur as the matrix is subjected to radial tensile stresses. The interfacial gap can increase with the  $\Delta\alpha$  range.
- $\Delta\alpha > 0$ , there is a presence of radial compressive stresses and circumferential (orthoradial) tensile stresses. The arising of these circumferential tensile stresses leads to radial micro cracking.

Whatever the case is ( $\Delta\alpha < 0$  or  $\Delta\alpha > 0$ ), the defects induced by thermal stresses lead to Young's modulus decrease.

Finally, thermal shock is another origin of thermal stresses. It may occur under specific conditions such as the presence of severe thermal gradient resulting from sudden heating or cooling. It has an influence on material properties and on components service life.

In some cases, it can be severe and can induce the total ruin of the component (Peruzzi, 2000) as illustrated in Figure I-2.

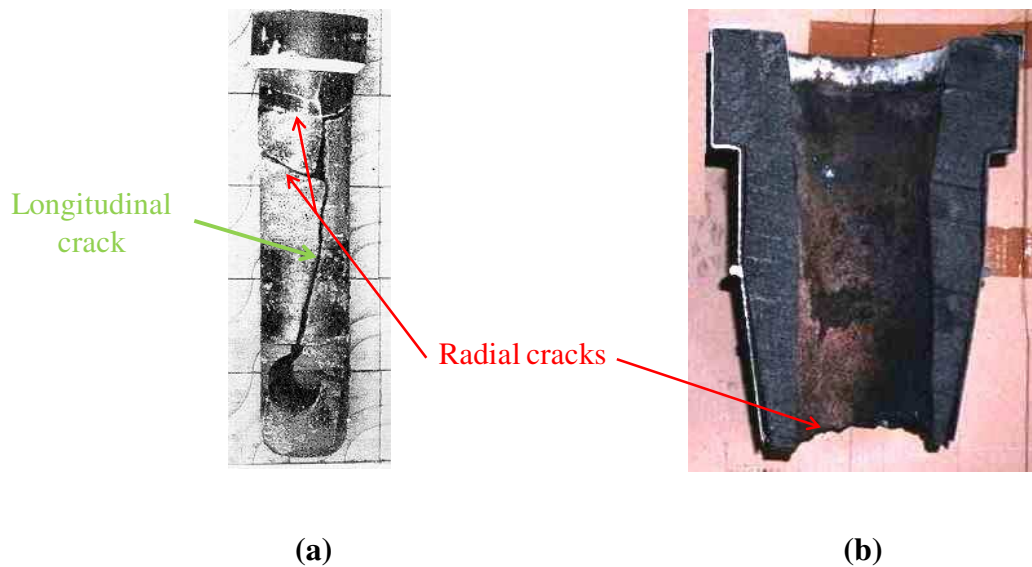


**Figure I-2: Examples of ruin due to thermal shock on some refractory products such as nozzle (a) and ladle shroud (b) used in continuous casting (Peruzzi, 2000)**

In fact, during a sudden hot thermal shock, the surface in direct contact with heat source (e.g. steel) becomes hotter than the other locations whose temperature remains lower. This may induce compressive and tensile stresses (Peruzzi, 2000; Grasset-Bourdel, 2011) respectively at the inner and the outer surfaces.

## **II.2. Crack growth process in refractories submitted to a thermal shock**

As shown previously, in industrial applications of refractories, fracture is one of the two most common modes of failure. The other one is chemical attack, or corrosion by the material that refractories are containing within the process vessel, as example molten metal slag or glasses at very high temperature. In this study, we will focus on the fracture aspects of these materials.

### II.2.1. Crack growth mechanisms

All refractory materials were considered for a long time as ceramics which exhibit a linear elastic mechanical behaviour. In the last decades, a deviation from this linear elastic behaviour called “non-linear character” has been introduced with specific concepts (Gogotsi et al., 1978; Harmuth et al., 1997; Huger et al., 2007). Non-linear mechanical behaviour of specific developed ceramics associated to their type of microstructure leads to the increase of their strain-to-rupture level. This allows a better accommodation of the high level of strain induced by thermal shock solicitations. It is characterized with a low stress-to-rupture (Figure I-3) and a presence of an irreversible strain when unloading in comparison with pure elastic behaviour of classical ceramic materials.

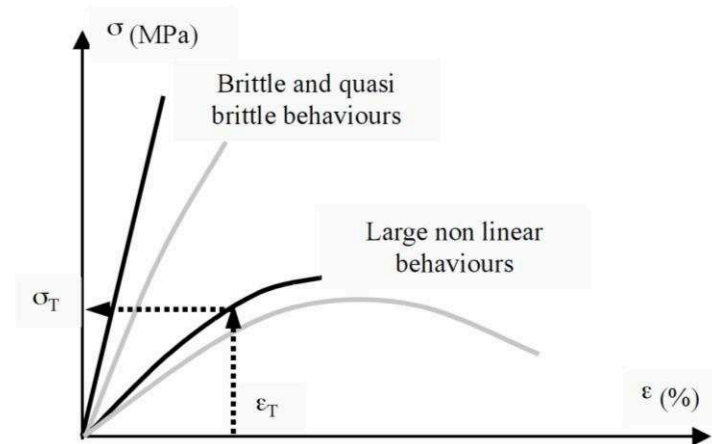


Figure I-3: Typical stress/strain behaviours observed on refractory materials (Huger et al., 2007)

This non-linear mechanical behaviour results of the complexity of the different inelastic phenomena occurring in crack region. The variety of these mechanisms are behind an important energy dissipating phenomenon, occur around the cracks and consume a large amount of energy as the crack front is progressing (Bradt, 1981).

According to the theory of linear elastic fracture mechanics, a crack propagates when the stress intensity factor  $K$  ( $\text{MPa}\cdot\text{m}^{1/2}$ ), at the crack tip, reaches the critical constant value  $K_{IC}$  of the material.  $K$  characterises material fracture toughness which describes its ability to resist failure in the presence of a crack.



The crack region can be divided to two areas: the frontal process zone and the following wake region as represented in Figure I-4.

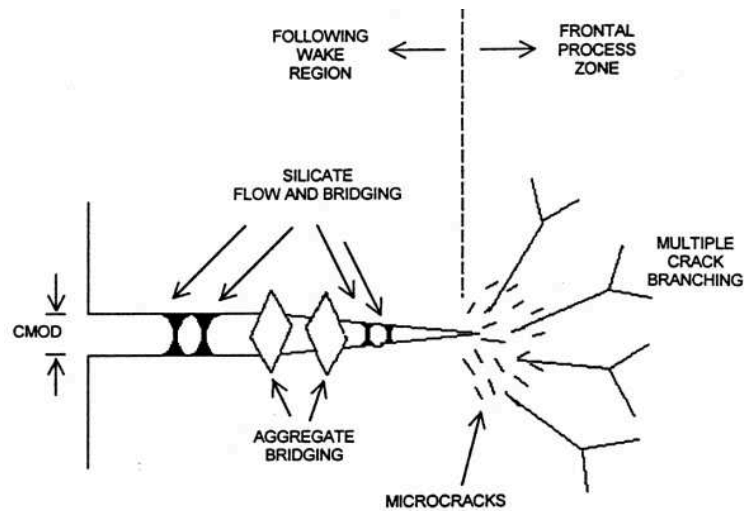


**Figure I-4: Schematic representation of the crack propagation zone for refractories (Bradt, 2004)**

The frontal process zone is localized ahead of the main crack and corresponds mainly to micro-cracking. It may lead to a large crack branching phenomenon depending on the microstructure and involving high energy consumptions. The size of this frontal process region depends on the type of refractory.

The following wake region is located behind the crack front and across the fracture surface. The phenomena occurring in this region are the most important from an energetic point of view. The main mechanisms are bonding of silicate ligament and bridging of aggregates (Figure I-4).

The bonding of silicate ligament is a consequence of refractory fracture at elevated temperatures where the glassy silicates become viscous and can flow and form bonding ligaments between the newly created fracture surfaces. In the other hand, the bridging of aggregates can appear at room temperature and contributes also to the crack growth resistance, but details about its mechanisms are still not fully clear (Bradt, 2004). Nevertheless, among the most common mechanisms are the bridging across the created crack

surfaces and the frictional effects of pull-out of the aggregates from one side of the passing crack.

As the phenomena which occur behind the advancing crack front have the most important effects to the crack growth resistance of refractories, some researchers have proposed numerous solutions to improve such property. It can be done by enhancing the fracture mechanisms using structural and microstructural design of aggregates such as particle size, geometrical aspects and strength of aggregates.

In fact, an aggregate must be at least as large as the crack mouth opening displacement (CMOD) so as to bridge the crack (Homeny et al., 1985). It is preferable to have angular aggregates as they can afford a mechanical interlocking effect greater than spherical aggregates. Besides, larger aspect ratio of the aggregates (ratio between their sizes in different dimensions) will give improved crack growth resistance. In addition to that, stronger aggregates are better than weak ones, and rough surfaces on the aggregates are preferred to smooth ones. In fact, when aggregates are stronger than their matrix bonding, the crack circumvents the aggregates and loops around them. This encourages the dissipation of energy during the bridging phenomena following the crack (Bradt, 2004).

### **II.2.2. Energetic approach**

After a reminder about the relationship between the possible origin of thermal stresses (mechanical constraints, thermal expansion mismatch and thermal gradient) and microstructural crack growth mechanisms, this paragraph links these crack growth mechanisms with thermal shock resistance of materials.

Thermal shock resistance is the ability of the material to withstand thermal stresses with minimal cracking (Baxendale, 2004). It can be characterized using experimental testing such as thermal cycling method (ASTM C1171-96) or calculations from material properties using Hasselman parameters (Hasselman, 1963, 1969). Hasselman proposed an attempt to rank materials quantitatively according to their thermal shock resistance using the parameters  $R'''$  and  $R_{st}$ . They allow forecasting the behaviour of defects inside the material during a temperature variation  $\Delta T$ .

$R''''$  (in m) is the thermal shock damage resistance parameter that compares the degree of damage after a given number of thermal shocks. It corresponds to the case of initially damaged materials with small cracks. In a first step, before  $\Delta T_c$  is reached, this crack propagates in an unstable way. In a second step, since the initial crack is much larger the crack extends in a stable way. The maximization of this parameter  $R''''$  is expected to reduce dynamic (or unstable) crack propagation.

$R_{st}$  ( $K.m^{1/2}$ ) is a quasi-static (or quasi-stable) crack growth damage resistance parameter defined to characterize thermal shock resistance of materials with large initial cracks.

$$R'''' = \frac{E \cdot \gamma_s}{\sigma_r^2} \quad \text{Eq. I-2}$$

$$R_{st} = \sqrt{\frac{\gamma_s}{E \cdot \alpha^2}} \quad \text{Eq. I-3}$$

where  $\gamma_s$  ( $N.m^{-1}$ ) is the surface fracture energy of the material and  $\sigma_r$  (MPa) material strength.

Hasselmann approach supposes that the material is initially damaged and this thermal shock causes the propagation of already existing cracks in unstable ( $R''''$ ) or stable ( $R_{st}$ ) ways.

From the expression of these two parameters, we can notice that they depend on elastic modulus and strength. Using simple form for stress expression and simple approximations such as  $E \cdot \alpha^2 \approx \frac{\sigma^2}{E}$ , it seems that both  $R''''$  and  $R_{st}$  are inversely related to  $\frac{\sigma^2}{E}$  which corresponds to the stored elastic strain energy in a sample at the stress level  $\sigma$  (Popov, 1999). This energy can be considered as the driving force for fracture or crack growth whether the thermal shock damage is either kinetic or quasi-static.

It is worth mentioning that thermal shock damage resistance parameter decreases as strength increases which means that high-strength refractories are much more sensitive to thermal shock damage. For this reason, industrials did not focus only on producing or developing high-strength refractories (Bradt, 2004) but they took into account their thermal shock resistance.

### II.2.3. R-curve approach

After detailing crack growth mechanisms and the energetic approach, this paragraph links these two aspects by introducing the R-curve concept of refractories.

The R-curve concept describes the evolution of the energy consumed for crack propagation as a function of the crack extension  $\Delta c$ . This concept was proposed in 1954 by Irwin and Kies (Irwin et al., 1954). Its major developments and initial experimental applications date from 1960 and were mainly devoted to metal and alloys (Boyle, 1962; Lauta et al., 1965; Forman, 1966). It was noticed in such kind of materials that a slow stable crack growth takes place prior to catastrophic failure for a cracked thin metal sheet.

It was then applied for different materials such as ceramics and especially refractories when Adams and Bradt noticed that long cracks were much more difficult to extend than short cracks by experimenting alumino-silicate refractories (Adams et al., 1981). Marshall and Swain (Marshall et al., 1988) pointed out that there was no unique R-curve for a material since it depends on experimental conditions of testing, size of sample and the location and depth of initial crack  $c$ . Currently, R-curve concept is becoming recognized as a basis for useful test methods applicable to less brittle materials (Mat et al., 1986; Evans, 1990; Saadaoui, 1991). Figure I-5 illustrates the R-curve evolution for different kinds of ceramics (Steinbrech, 1992).

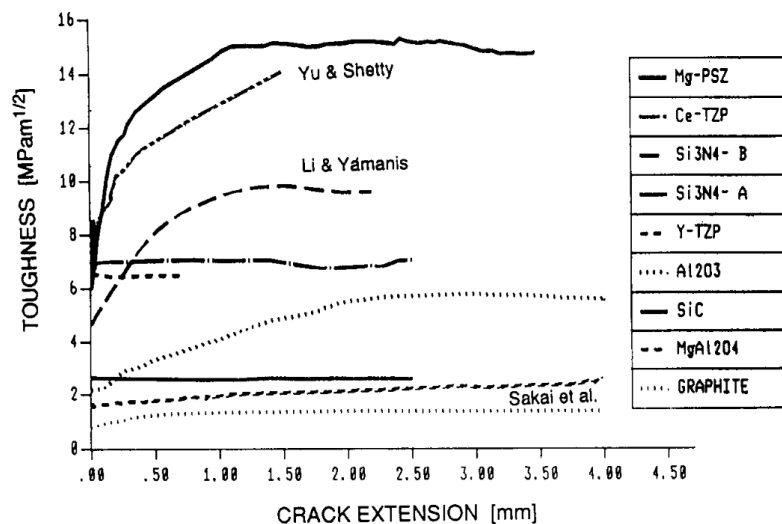


**Figure I-5: R-curves of ceramic materials results of measurements on long cracks in compact tension samples (Steinbrech, 1992)**

For brittle materials, the R-curve is flat that means that the crack growth resistance is constant with crack length. In this case, the R-value is just  $2\gamma_s$  (Bradt, 2004).

For large grained ceramics such as refractories, the R-curve is rising. As the crack extends, it gets more difficult for it to grow, due to the occurrence of new mechanisms in the following wake region of the crack (Figure I-4). These curves confirm that few phenomena are activated at crack initiation. During its propagation, the number of activated mechanisms increases and so the total energy release rate becomes higher. These mechanisms make the refractory stronger before its failure and generate a non-linear mechanical behaviour. This non-linear behaviour has been related to the improvement of thermal shock resistance in the late 1970s (Gogotsi et al., 1978; Gogotsi, 1993). So, the rising R-curves can be directly associated to thermal shock resistance of refractory materials.

In fracture mechanics, by definition, crack propagation occurs when the total energy release rate per unit surface of propagation (or strain energy release rate)  $G$  is higher than  $R$  which corresponds to the crack growth resistance (or energy dissipation rate).

According to Griffith approach,  $G$  can be obtained using the following equations in plane stresses case for a thin rectangular plate with a crack perpendicular to the load:

$$G = \frac{\pi.c.\sigma^2}{E} \quad \text{Eq. I-4}$$

To understand easily the relation between the R-curve and fracture mechanisms, Figure I-6 represents a typical rising R-curve associated to the one of  $G$  at two different states  $\sigma_1$  and  $\sigma_2$  ( $\sigma_1 < \sigma_2$ ).  $G$  is linear for a given state of stress  $\sigma$  (Green, 1998).

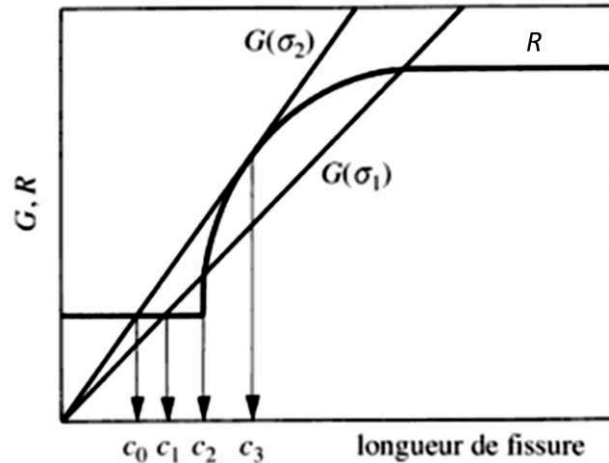


**Figure I-6: Schematic R-curve representation (Green, 1998)**

According to the stress level, different cases can be observed (Wachtman et al., 2009). For an initial crack  $c_0$  under  $\sigma_1$ , no crack propagation will occur ( $G(\sigma_1) < R$ ). An initial crack  $c_1$  under the same stress, an extension with unstable crack propagation will occur ( $G(\sigma_1) > R$ ) until reaching  $c_2$  ( $G(\sigma_1) < R$ ). As the applied stress  $\sigma$  is increasing (from  $\sigma_1$  to  $\sigma_2$ ), the extension of crack propagation will occur in a stable way until  $c_3$  where  $G(\sigma) = R$ . Then,  $G(\sigma_2)$  becomes higher than  $R$ , so unstable crack extension happens and induces the rupture of material.

### III. Optical and numerical approaches in mechanical characterization of refractories

In the last decades, numerous numerical methods of simulation have been developed to investigate mechanical issues with different degrees of complexity at both a macro and a micro-scale. These techniques allow the prediction of the mechanical behaviour of materials during their service life.

Besides, the appearance of optical methods to achieve kinematic measurements is considered as a promising support in the real characterisation of mechanical behaviour of heterogeneous materials at different scales. It can investigate the mechanical behaviour without using classical techniques such as strain gages and extensometers which still limited

in terms of measured area. Thanks to the efficiency of these techniques, their application can be extended to components under mechanical solicitations such as slide gates and ladle shroud.

### **III.1. Optical methods**

Aside from classical techniques widely used for characterisation, various non-contact optical methods have been developed and applied for this purpose. These methods are now appreciated by the researcher community as they provide efficient pieces of information on the analysed surface, in addition to their other advantages such as their simple experimental setup and low cost implementation.

#### **III.1.1. Digital image correlation**

Among the most common optical techniques, digital image correlation (DIC) is one of those that this thesis is focused on. DIC measurements accuracy has been improved in the last researches according to the application used for.

##### **III.1.1.1. Context**

DIC appeared in the early 80s and was developed by a group of researchers at the university of South Carolina (Peters et al., 1982, 1983; Chu et al., 1985; Sutton et al., 1986). It is based on mathematical computations and progresses taking into account the optical devices evolution. Then, the technique has been simplified and optimized in terms of calculation parameters in order to be applied by different kinds of users. Many names have been given to this practice such as: DIC (Chu et al., 1985), electronic speckle photography (Sjödahl et al., 1993), texture correlation (Bay, 1995), digital speckle correlation method (DSCM) (Zhang et al., 1999) and computer-aided speckle interferometry (CASI) (Gaudette et al., 2001). Nevertheless, the method is called DIC in this study, considering its popularity in most of the published literature.

It allows measuring kinematic fields by operating digital images obtained before and after deformation using different means of non-contact optical acquisitions (Figure I-7).

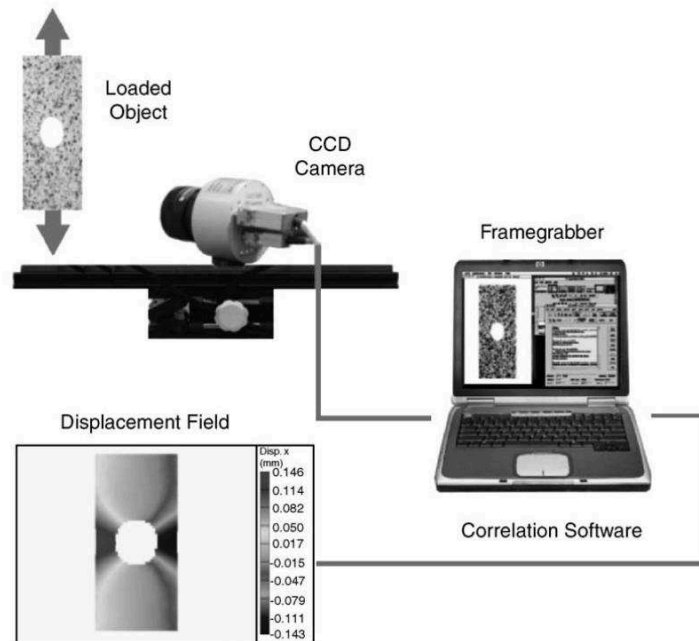


**Figure I-7: Schematic of DIC (Lecompte et al., 2006)**

This technique can be applied at different scales depending on acquisition device. CCD cameras (Lecompte et al., 2006) (Figure I-7) or various high-spatial-resolution devices such as optical microscopy (Sun et al., 1997) and scanning electron microscopy (SEM) (Sabate et al., 2006) can be used to process the technique. Recent released cameras allow instantaneous deformation measurement thanks to high-speed digital image recording equipment (Barthelat et al., 2003). From recorded images, kinematic fields can be obtained using appropriate correlation software.

DIC has been significantly improved for expanding its application range. It can be directly applied for the characterisation of deformation mechanism of various materials (e.g. metal, composite, polymer, wood, biological materials) subjected to different types of loadings (thermal, mechanical or other) (Bastawros et al., 2000; Wattrisse et al., 2001; Abanto-Bueno et al., 2002; Périé et al., 2002; Chevalier et al., 2001; Xiang et al., 2007; Chiang, 2008; Feissel et al., 2009, 2012, 2013). Recently, numerous works were carried out to better understand the behaviour of refractory materials thanks to this technique such as the characterisation of mechanical behaviour of fiber reinforced refractory castables (Orteu et al., 2007; Robert et al., 2007; Dusserre et al., 2013), the thermal strain behaviour of  $\text{Al}_2\text{O}_3\text{-MgO}$  castables (Kamio, 2011; Kamio et al., 2011) or the asymmetric behaviour of aluminium



titanate  $\text{Al}_2\text{TiO}_5$  ceramics and identification of their stress-strain law (Leplay et al., 2010, 2012).

### III.1.1.2. Measurement of kinematic fields

In this paragraph, the measurement of displacement and strain fields using DIC is introduced.

After recording images, a computation allows the comparison between two images. One corresponding to the reference state and the other corresponding to the deformed one (Figure I-8). The zone of interest (ZOI), in which the calculation is carried out, is divided into a numerous correlation windows which are a part of a virtual grid (Figure I-8). The number and size of those windows determine the measurements accuracy. Each window contains a given grey level values. These grey level values (positive integers) are considered as input data for DIC computation and vary between 0 and 256 for an 8-bit sensor which is the most used.

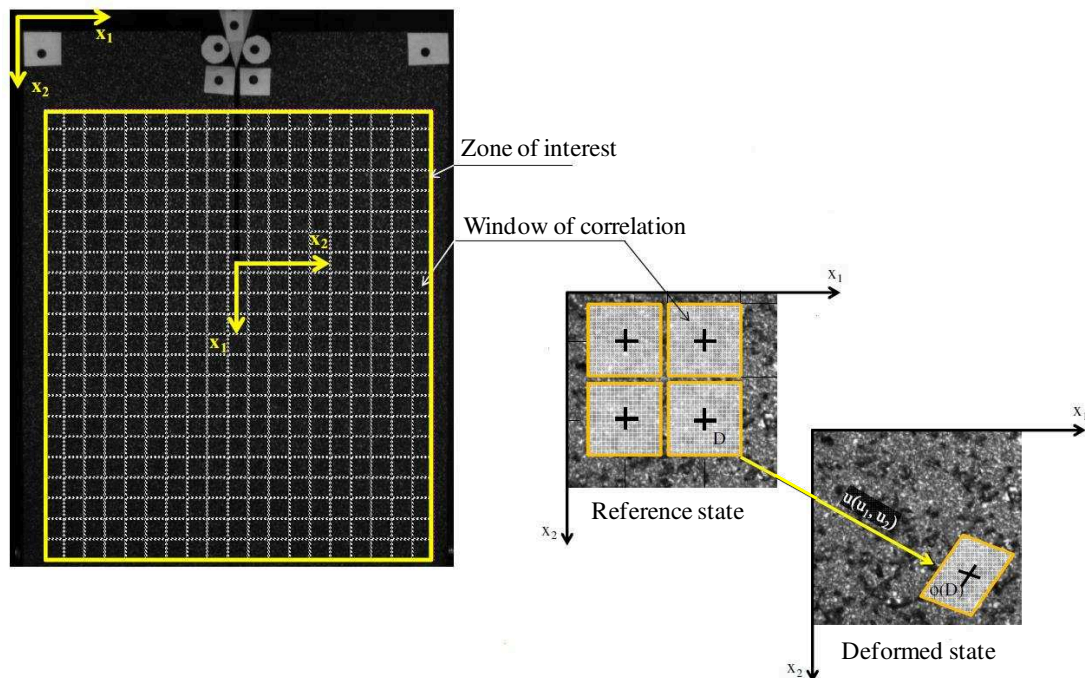


Figure I-8: Description of computational state between reference and deformed state (Pop, 2013)

Displacements are computed within correlation windows in order to obtain displacement field measurements in the ZOI. These displacements are defined by a plane material transformation linking the reference state coordinates to the deformed state ones. The computation principle will be more detailed in chapter 2.

Displacement field is useful for detecting cracks presence as it induces a discontinuous displacement field (Grédiac et al., 2011). However, for other applications, such as describing deformation behaviour, strain fields estimated from displacement fields can be more relevant.

Strain field is evaluated from displacement field using finite differences as will be detailed in chapter 2. This means that strain field accuracy depends on the quality of the displacement measurements.

### III.1.2. Mark tracking method

Among the optical techniques which allow the characterisation of material behaviour, mark tracking method can be quoted. Unlike DIC, regular markers deposited on the studied surface are used instead of speckles. This method consists in tracking these markers during the test. It can be used for instance to evaluate displacements and strains on a surface under mechanical solicitation. The measurements resolution depends on the size and the distance between these markers. From these average strains and using the applied stresses, an average value of Young's modulus and Poisson ratio on the area of interest can be determined as represented in Figure I-9 on a PET plastic under tensile test (Brémand et al., 2011).

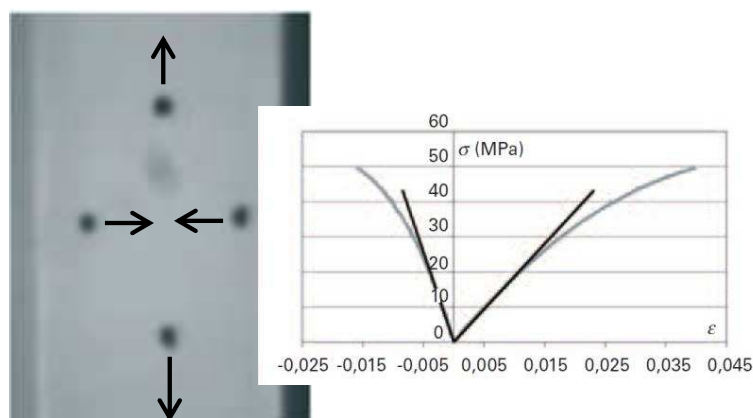


**Figure I-9: An example of mark tracking application in the characterisation of local material properties from (Brémand et al., 2011)**

### III.1.3. Accuracy of kinematic measurements and sources of errors

Kinematic measurements quality depends on sample preparation, experimental conditions and on images numerical processing.

Firstly, a great attention must be paid to the sample surface preparation. For example, to enhance the contrast of this surface, a random speckle pattern is applied. It provides a unique texture or signature to every element on the recorded surface. This pattern can be the natural specimen texture or may be obtained artificially by spraying black and/or white paints or other techniques. The quality of speckles can be evaluated using various parameters such as the number of pixels per droplet, the mean speckle size (Lecompte et al., 2006) and the grey level distribution in the ZOI which should cover a wide range (Robert et al., 2007) (Figure I-10).

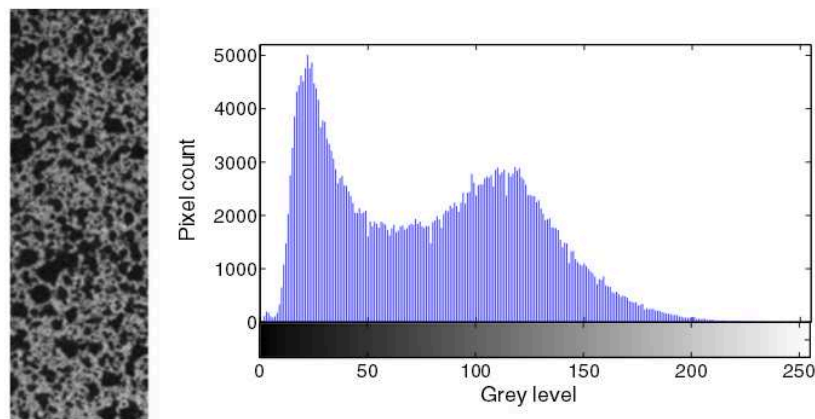


**Figure I-10: Example of a random grey pattern and its associated grey level distribution (Robert et al., 2007)**

Secondly, sample surface has to be flat and parallel to the CCD camera sensor. Out-of-plane motion of the specimen during loading should be small enough to be neglected. This is due to the fact that out-of-plane motion can cause the presence of additional in-plane displacements. Obviously, this condition is difficult to achieve experimentally.

Finally, after recording images, the choice of correlation parameters, such as the position and size of correlation windows, has a great influence on determined results quality. To achieve a reliable correlation analysis using DIC, the size of the correlation window has to be large enough to distinguish the windows between the others so as to obtain distinctive information. Small correlation window leads to high accuracy in displacement values and the distance between these windows determines the strain measurements accuracy. The above two properties imply that there is a compromise to find to be satisfied.

## **III.2. Finite element method updating (FEMU): identification of material properties**

Although mechanical analytical approaches allow getting valuable pieces of information on the required material properties, classical equations used for such purpose are still only available for the characterization of elastic linear behaviours of classic ceramics but cannot really be applied for refractories which often refer to a non-linear mechanical one. During the last decades, Finite Element Method (FEM) was and still a useful technique to predict material behaviour during its application. Besides, the apparition of optical methods leads scientists to conjugate them with FEM to propose new areas of investigation to enrich the mechanical characterisation of materials.

### **III.2.1. Introduction to identification methods**

Identification methods are divided into updating and non-updating ones. Among the updating techniques, finite element method updating (FEMU), constitutive equation gap method (CEGM), reciprocity gap method (RGM) can be quoted. In the other hand, as example of non-updating methods, equilibrium gap method (EGM) and virtual field method (VFM) may be cited.

Coupling these identification techniques with digital image correlation methods make it possible these last to increase significantly their potential of characterization. Various mechanical parameters of a material can be further identified based on the computed displacement field or strain field. Identified parameters include Young's modulus and Poisson ratio (Cho et al., 2005; Zhang et al., 2006), in addition to stress intensity factor (McNeill et

al., 1987; Roux et al., 2006), residual stress (Sabate et al., 2007) and thermal expansion coefficient (Lyons et al., 1996; Bing et al., 2009).

In updating methods, displacement fields are numerically computed, usually by FEM analyses, using an initial guess. Then the identification is done by minimizing an objective function. It can lead to iterative computational procedures, which may be CPU-intensive, and besides tend to become sensitive to measurement scattering if based on insufficient experimental data (thus regularization approaches are required). Non-updating methods have the advantage of usually leading to fast computational procedures. Besides, they specifically require full-field displacement data determination with sufficiently spatial resolution. A recent study (Avril et al., 2008) compared these different identification methods in order to determine elastic properties (Young's modulus and Poisson ratio) of a composite material. Based on this study outputs, it appears that, using the same data, each method can provide quite different results, especially for Poisson ratio. They are sensitive to error sources in data, and this sensitivity to error sources is higher for non-updating approaches which may fail to provide a solution when data have low spatial resolution.

Among updating methods, the FEMU (Haddadi et al., 2005; Lecompte, 2007; Cooreman et al., 2008; Decultot, 2009) is still one of the most used for material properties identification of heterogeneous and homogeneous materials whose geometry is the cause of the generation of heterogeneous stresses (Grédiac et al., 2011). This is why it will be considered in this study.

### **III.2.2. Finite element method updating**

#### **III.2.2.1. Overview of finite element method (FEM)**

The finite element method (FEM) is a useful engineering tool for numerical approximating of physical systems which are too complex for an analytical solution or governed by behaviour that is highly complicated. It is used in engineering to estimate a solution to partial differential equations and integral equations.

The value of studied parameters for a specific element is approximated and depends on the element size and estimating technique. Simple models with large elements are quickly

computed and complex models with fine resolution (small elements, fine mesh) can yield more realistic results at the cost of increased computational time.

### **III.2.2.2. Description of FEMU**

FEMU is based on a coupling of a finite element model and an optimization algorithm. It was presented in 1971 by Kavanagh (Kavanagh et al., 1971) and has known important evolutions. FEMU consists in performing iteratively finite element simulations (FEM) in order to minimize the difference between experimental and simulation results using an objective function. Many iterations may be required for convergence, thus models should be simplified as much as possible in order to reduce the computational time at each iterations (Jonsson et al., 2007). Different approaches of FEMU exist and are mainly based on the comparison between experimental and simulated data. These data can be an applied load (FEMU-F) or a displacement (FEMU-U). It is also carried out in the identification of thermo-mechanical models where temperature fields are used (FEMU-T) (Figure I-11).

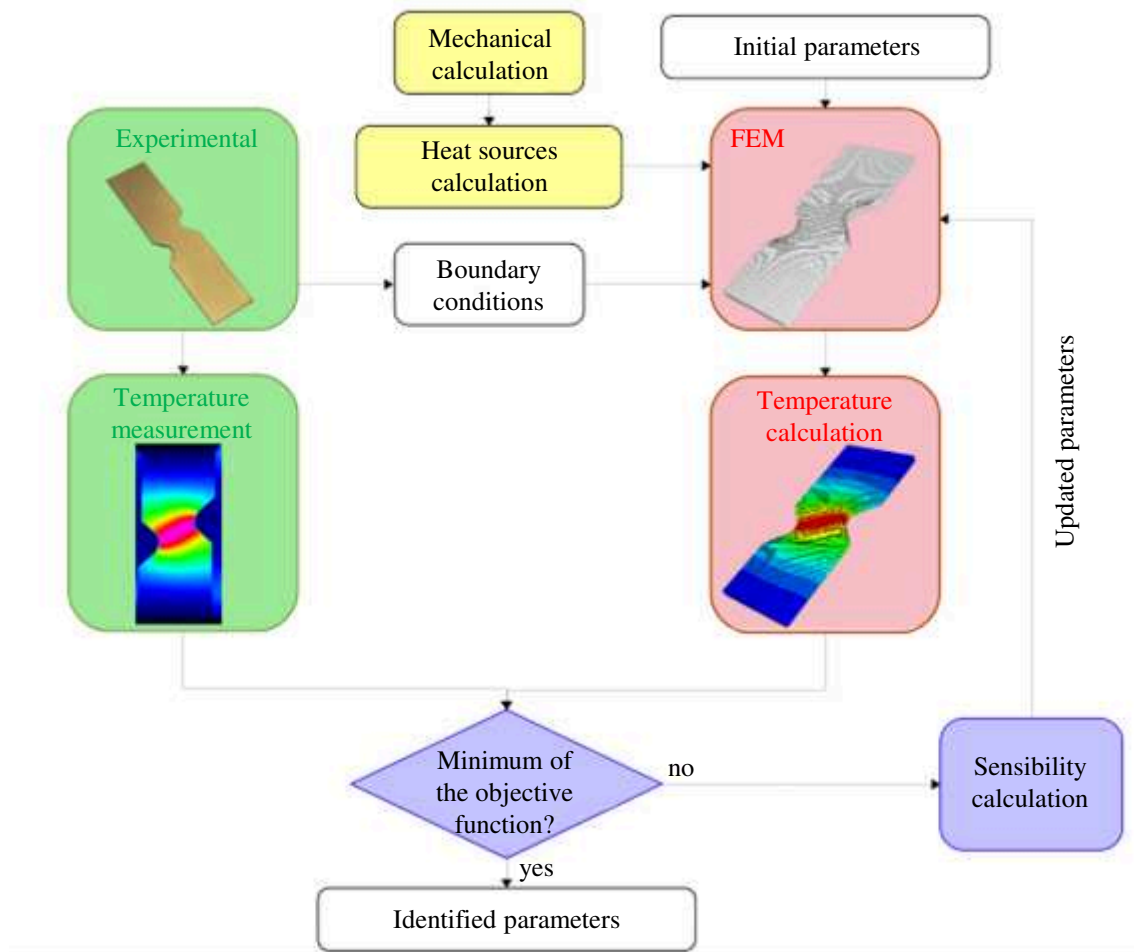


**Figure I-11: Principle of identification method using FEMU-T (Pottier, 2010)**

FEMU-U can be associated with DIC in order to determine material elastic properties. Displacement fields obtained using DIC were preferred to strain fields in order to avoid additional scattering obtained by differentiating displacement fields (Decultot, 2009).

## IV. Conclusion

This first chapter allowed us to establish the state of the art concerning thermal shock resistance of refractory materials and non-linear mechanical behaviour of these materials by analysing both energetic and mechanical approaches. This deviation from linear elastic behaviour can be considered as a solution to improve thermal shock resistance of refractory materials. However, to characterize such materials, it is necessary to develop some experimental techniques in order to evaluate in the best reliable way their specific properties.

Besides, the occurrence of optical methods that allow non-contact full-field measurements such as digital image correlation and numerical techniques like finite element method updating provides the advantage to investigate refractory materials. In the present work, different refractory materials chosen in purpose for their non-linear mechanical behaviour will be studied using different mechanical tests. Some of these tests are commonly applied for elastic linear materials. Here, the originality of the study is to achieve the coupling of non-contact optical methods in order to better understand the overall behaviour of these non-linear refractory materials.



# Chapter III

## Experimental techniques and materials selection

## I. Introduction

Fracture of granular materials in general and refractories in particular is usually associated with the concept of strength. Refractories strength can be determined using different mechanical tests. As examples, we can quote the three-point bending test which permit to investigate flexural strength, frequently called “modulus of rupture MOR” (ASTM C133-97) or the Wedge Splitting Test (WST) that provides a nominal notch tensile strength (Brühwiler et al., 1990) to be determined or the Brazilian test allowing the evaluation of tensile strength (ASTM D3967-95a) thanks to indirect sollicitation (compression).

However, the parameters extracted from these experimental tests cannot be sufficient to perform a full mechanical characterisation of some materials which exhibit singular behaviours such as non-linear ones. For this reason, in order to feed FEM, the knowledge of constitutive laws was necessary. To do so, it was important to develop uniaxial tests taking into account that these materials are characterized with a low level of strains. Nowadays, to determine local material constitutive laws to feed finite elements method, accurate instrumented tensile test with extensometers are used (Marzagui, 2005; Kakroudi, 2007).

Besides, the occurrence of optical techniques such as DIC and the development of identification methods like FEMU-U over the last decades give new areas and opportunities of investigation of refractories showing a non-linear mechanical behaviour. These techniques were developed for various materials, but few applications were applied on refractories.

This chapter aims to present the different techniques of characterization used and associated to DIC. To do so, a development of the technique is required and was done on a model material, then applied on several industrial ones. These materials will be introduced at the end of this chapter.

## II. Determination of elastic properties: Ultrasonic technique at room temperature

The first properties needed for material characterization are elastic properties (Young’s modulus  $E$ , Shear modulus  $G$  and Poisson ratio  $\nu$ ).

After calculating material density according to ASTM C830-00, elastic properties have been determined thanks to ultrasonic technique at room temperature in transmission mode as the materials are heterogeneous and porous. This technique has been used here in order to obtain reference values of elastic properties. It is based on measuring wave propagation time within sample between two transducers in transmission configuration as represented in Figure II-1. One transducer (transmitter) is applied on one sample face and sends directly ultrasonic waves across it. A second transducer (receiver) collects the waves on the front face. A coupling agent (Sofranel SWC) is used to optimize the contact between sample and transducers. A coupling agent (Sofranel SWC) is used to optimize the contact between sample and transducers.

The received signal is recorded on a digital oscilloscope. The propagation velocities of both longitudinal and transversal acoustic waves ( $V_L$  and  $V_T$  respectively) are needed here to calculate the elastic properties in infinite mode. To achieve that, the time of flight  $\Delta\tau$  between two echoes (one related to signal evaluated with sample and the other without sample) corresponds to the wave propagation time within the sample (Figure II-1). An alumina buffer is used to be sure that the maximum of the signal is in the Fraunhofer zone.

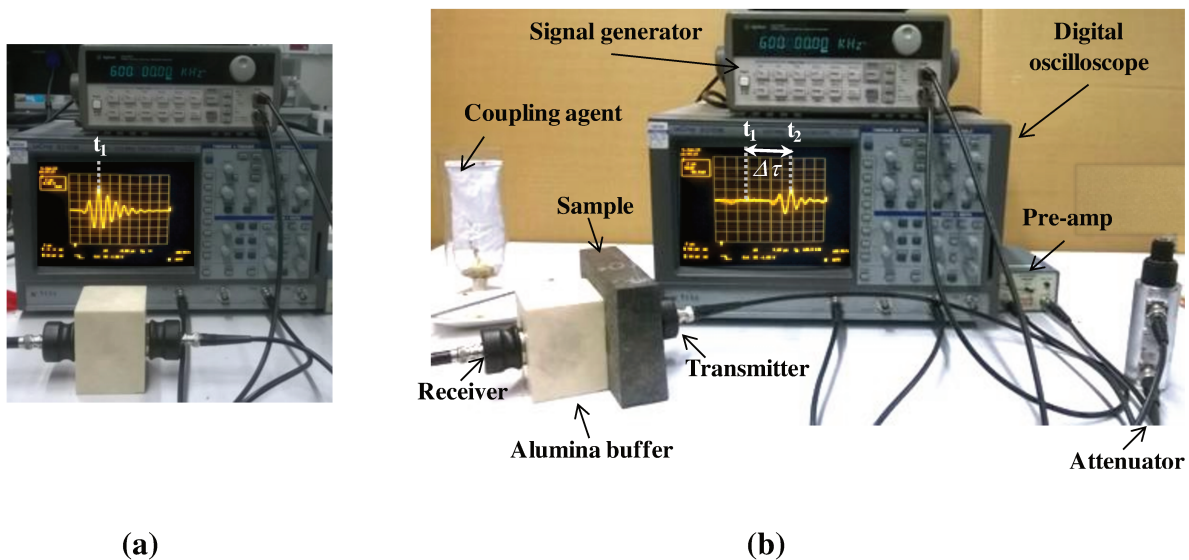


**Figure II-1: Experimental setup for measuring the ultrasonic velocities by transmission method at room temperature: (a) without sample, (b) within sample**

In infinite medium, two propagation modes exist, Longitudinal (Pressure waves P) and Transversal ones (Shear waves S). The associated velocities are respectively estimated according to the following expressions:

$$V_L = \frac{e}{\Delta\tau_L} \quad \text{Eq. II-1}$$

$$V_T = \frac{e}{\Delta\tau_T} \quad \text{Eq. II-2}$$

where  $e$  (m) is sample thickness.  $\Delta\tau_L$  (s) and  $\Delta\tau_T$  (s) were measured respectively by a pair of longitudinal and transversal transducers.

Then, Young's modulus  $E$  (Pa) and shear modulus  $G$  (Pa) can be calculated using the following equations

$$E = \rho \cdot \frac{(3V_L^2 - 4V_T^2)}{\left(\frac{V_L^2}{V_T^2} - 1\right)} \quad \text{Eq. II-3}$$

$$G = \rho \cdot V_T^2 \quad \text{Eq. II-4}$$

From  $E$  and  $G$ , Poisson ratio  $\nu$  is deduced thanks to the equation below:

$$\nu = \frac{E}{2G} - 1 \quad \text{Eq. II-5}$$

### III. Characterization of mechanical behaviour

#### III.1. Four-points bending test

In some specific applications, four-points bending test can be preferred to three-point bending test which is the most commonly applied experiment to refractory materials (ASTM C133-97). In fact, the difference lies in the stress distribution within the loaded sample. Unlike three-points bending test, it has a uniform stress distribution in the central part of sample (Figure II-2a) which is better to access easily to reliable elastic properties.

From ASTM C1161-02c, a bending device was designed to test large size samples. Due to a lack of machining sample surface quality, additional degrees of freedom are needed in order to balance mechanical loading on sample. For instance, rolls 2, 3 and 4 can rotate along X-axis (Figure II-2a). The upper or lower pairs of rolls are free to rotate around Z-axis in order to avoid additional frictional stresses. This test permits the application of compression and tension stresses in the central part between the upper rolls (Figure II-2b).

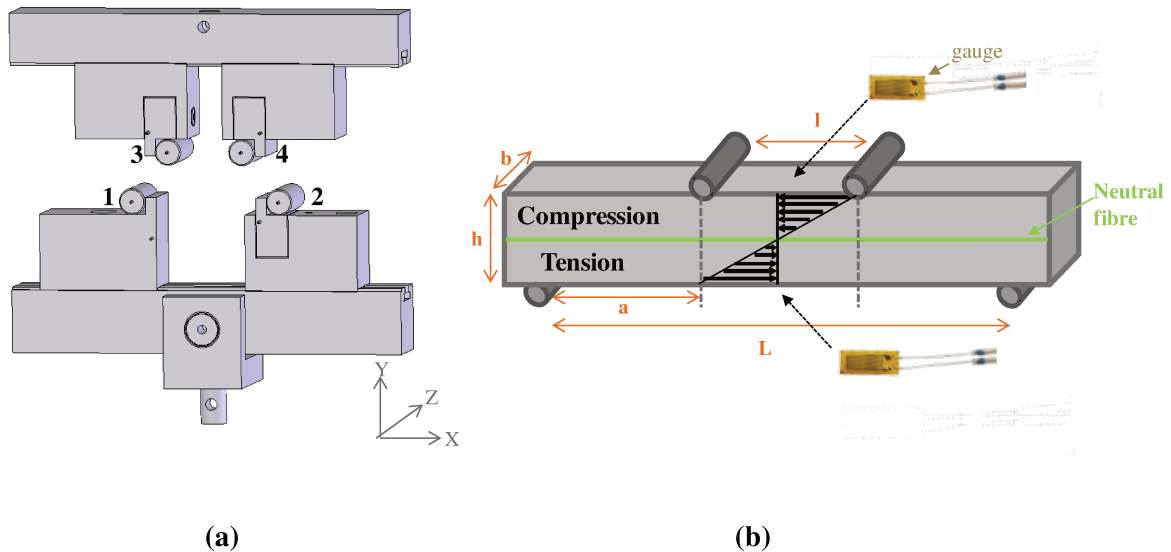


**Figure II-2: Four-points bending test: (a) bending device, (b) distribution of stresses**

Stresses distribution is symmetric with respect to the middle of the sample. The maximum stresses area corresponds to the surface in contact with rolls, and the part of sample with no applied stress is localised in the centre of the sample and constitutes the so-called “neutral fibre”. Unlike three-points bending test, this test allows avoiding the presence of shear stresses in the area located between the upper rolls.

The tensile stress  $\sigma$  (Pa) obtained on the tensile loaded surface is calculated using the following equation for a linear behaviour symmetrical between tension and compression:

$$\sigma = \frac{3 P \cdot (L - l)}{2 b \cdot h^2} \quad \text{Eq. II-6}$$

where  $P$  (N) is the applied load,  $b$  (m) and  $h$  (m) are respectively the width and the thickness of the specimen,  $L$  (m) and  $l$  (m) are the distances between the lower and the upper rolls. Using the Eq.II-6 stress-to-rupture can be calculated.

Theoretically speaking, Young's modulus  $E$  is given by the following equation:

$$E = \frac{L-1}{8.bh^3} \cdot \frac{P}{\delta} \cdot (2L^2 + 2Ll - l^2) \quad \text{Eq. II-7}$$

where  $\delta$  (mm) is the deflection.

Nevertheless, during experimental test, material depression under rolls is inevitable and usually leads to an overestimation of  $\delta$  which induces an underestimation of  $E$ . For this reason, strain gauges are often preferred to measure deformation. One can be glued on the upper surface of sample and another one on the lower surface. Elastic properties can be then determined using stress-strain values. In such case, Figure II-3 is an example of stress-strain curve of recorded values. From this figure,  $E$  is calculated using the slope at the very early part of the curve; it corresponds to an elastic linear behaviour. It assumes a symmetric tensile-compressive behaviour.

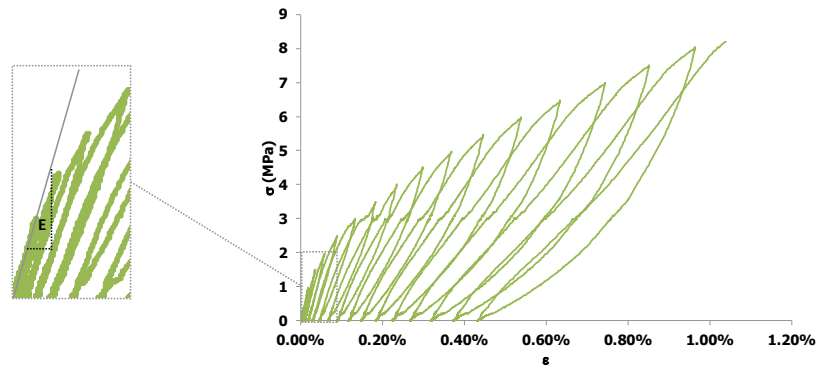


**Figure II-3: Example of stress-strain curve obtained for an aluminum titanate sample**

The two equations (Eq.II-6 and Eq.II-7) are established within the framework of linear elasticity theory. As a consequence, it leads to incorrect estimations in the case of asymmetric non-linear tensile-compressive mechanical behaviours. It can contribute to a gap between effective and estimated values which can reach around 40% for strength at room temperature (Leplay et al., 2012).

### III.2. Brazilian test

Brazilian test has been developed in the early 1940's to face a challenging engineering problem: a church was located in the axis of a new avenue to be built in Rio de Janeiro. The engineering solution that was found to avoid the demolition of the church was to move it on concrete rolls as the production of steel was directly focused to the war effort.

Concrete rolls testing were done by a Brazilian team which was in charge of testing the cylindrical concrete rolls. This induced the development of a test for the tensile strength that could be performed on normalized cylinders defined by the Brazilian standards for compressive tests ( $\phi=150$  mm,  $L=300$  mm). The method was presented in 1943 at the 5<sup>th</sup> meeting of the Brazilian Association for Technical Rules (ABNT) (Carneiro, 1943). For the records, two months later, a similar method was independently presented in Japan by Akazawa (Akazawa, 1943) without any communication between researchers (Brazil and Japan were on opposite sides in World War II).

Then, in the following years, some researches were focused on the comparison between Brazilian disc, and uniaxial tensile tests as well on the validity of tensile strength of rocks and rock-like materials obtained by Brazilian test (Fairhurst, 1964; Hobbs, 1965; Hiramatsu et al., 1966). Indirect tensile test of anisotropic rocks were experimentally and investigated (Barla et al., 1973). The Brazilian test had become then very popular to measure tensile strength of rocks all over the world (Andreev, 1991). The improvement of this test has been extensively studied and discussed.

The principle of the test consists of applying a diametrical compressive force along the length of a cylindrical concrete specimen until failure occurs (Fairhurst, 1964; Andreev, 1991; Guo et al., 1993; Wang et al., 2004; Huang et al., 2012). This loading induces tensile stresses on the plane containing the applied load and relatively high compressive stresses in the area close to the contact zone. Tensile failure occurs rather than compressive failure (Rodríguez et al., 1994). This test has been normalized in the standard ASTM D3967-95a and nowadays used by many industrial laboratories.

This test is easy to handle, and is used currently by many communities such as refractory one (for instance Tatasteel R&D). Sample preparation requires a specific attention to obtain repeatable results. According to ASTM D3967-95a, test specimen shall be a circular

disk with a thickness-to-diameter ratio ( $e/D$ ) between 0.2 and 0.75 in order to be in a plane stress configuration (Darvell, 1990). The diameter of specimen shall be at least 10 times greater than the largest mineral grain constituent.

Different typical loading configurations exist and are represented in Figure II-4.

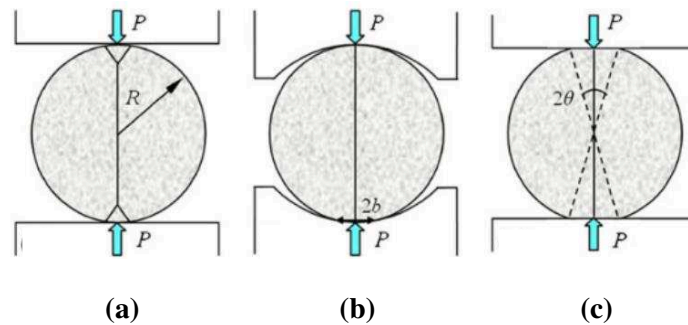


**Figure II-4: Examples of Brazilian test configuration. (a) flat loading bearings, (b) curved bearings and (c) flattened Brazilian disc (Chen et al., 2013)**

In the Brazilian test, the contact point between the loading bearings and the circular boundary of the specimen will lead to stress concentration at the loading contact. This stress concentration may lead to undesired damage in this area. Two attempts have been made to avoid this undesired failure in disc specimen (Chen et al., 2013). One was changing the flat loading bearings (Figure II-4a) into curved bearings to fit the specimen (Figure II-4b). The other attempt was to modify the sample shape by machining two opposing flat ends on sample to fit the regular loading bearings (Figure II-4c). In the present work, curved bearings will be used (Figure II-5).



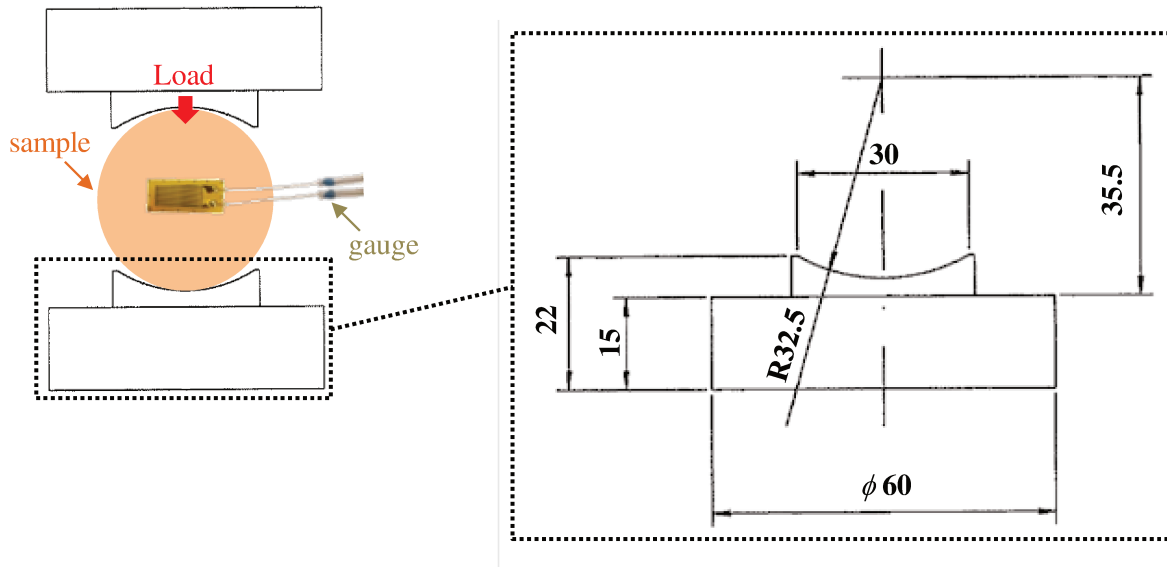


**Figure II-5: Details of Brazilian test device with curved load bearing**

Tensile stress  $\sigma_t$  is determined thanks to the following equation:

$$\sigma_t = \frac{2.P}{\pi.e.D} \quad \text{Eq. II-8}$$

where  $P(N)$ ,  $e(m)$  and  $D(m)$  are respectively, the applied load, thickness and diameter of cylindrical sample. Samples with  $e=0.01$  m and  $D=0.05$  m will be used.

The main objective of this test is to determine material tensile strength  $\sigma_t$ . Nevertheless, some authors investigated the possibility to characterize elastic properties and fracture parameters.

Young's modulus calculation using Brazilian test is not easy to perform due to two major difficulties. Firstly, the sample is not submitted to uniaxial sollicitation and the secondly the load-displacement curve is non-linear due to the device itself. Nevertheless, some authors (Jianhong et al., 2009) have proposed an approach to analyse the results.

Young's modulus characterized in tension  $E_t$  can be evaluated using this equation:

$$E_t = E_s \cdot A \quad \text{Eq. II-9}$$

where  $E_s$  is defined as splitting elastic modulus which can be determined from the following equation:

$$E_s = \frac{\sigma_{0.5}}{\varepsilon_{0.5}} \quad \text{Eq. II-10}$$

where  $\sigma_{0.5}$  and  $\varepsilon_{0.5}$  correspond respectively to half test values of stress and strain (Figure II-6). This choice is proposed to overcome non-linearity of the curve.

$A$  is a correction coefficient, related to the presence of biaxial stresses, which depends on sample geometry and Poisson ratio  $\nu$ :

$$A = \left(1 - \frac{D}{L} \arctan \frac{2L}{D}\right)(1 - \nu) + \frac{2D^2(1 + \nu)}{4L^2 + D^2} \quad \text{Eq. II-11}$$

where  $2L(m)$  is strain gauge length.

In the present study, strain measurement by gauges will be replaced by DIC.

Figure II-6 represents a typical load-displacement curve obtained using Brazilian test. This curve can be divided in four stages:

- **Stage 1:** Load-strain curve exhibits an upward curvature related to the elastic linear behaviour of the tested material.
- **Stage 2:** Load-strain curve shows a downward curvature linked to stable crack propagation until the load reaches the maximum value.
- **Stage 3:** The load decreases rapidly as the crack widens in the unstable crack extension stage.
- **Stage 4:** An increase of load occurs again and is related to the two separate disc halves.

An attempt to estimate the surface fracture energy is proposed using the ratio:

$$G_f = \frac{W}{A_f} \quad \text{Eq. II-12}$$

The total dissipated energy  $W$  (Jonsén et al., 2007) can be obtained using a straight line between two points that determine the limit of elastic energy (Figure II-6). Point 1 is chosen as the beginning of linear elastic stage and point 2 corresponds to the minimum value of the load after unstable cracking. The fracture energy is the difference between the area under the curve and the area related to the elastic energy.  $A_f$  is the surface of fracture.

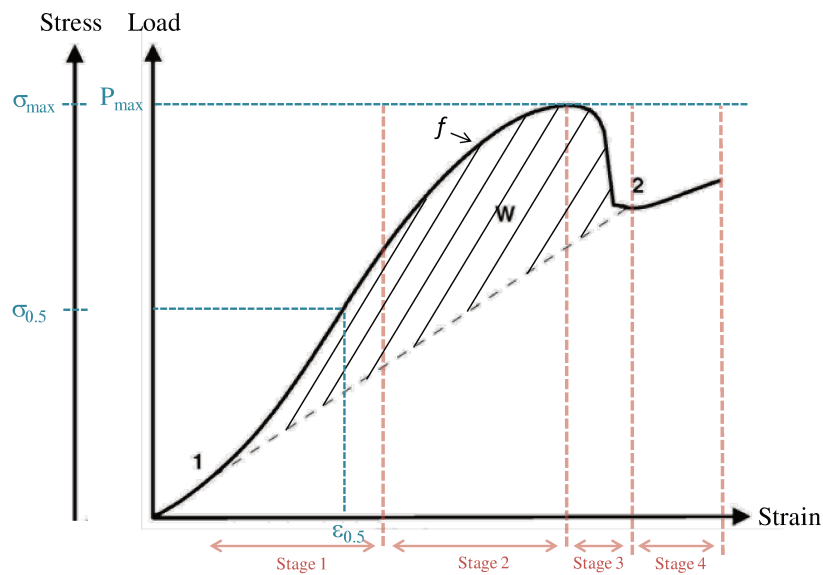


**Figure II-6: Representation of the total dissipated energy  $W$  during Brazilian test. It is represented by the area enclosed by the dashed line and the solid line between points 1 and 2 (from Jonsén et al., 2007)**

The approach should be considered as a very first tentative to estimate surface fracture energy. Another kind of experimental test has been specifically developed much later (Tschegg, 1986): “wedge splitting test”. It is much more adapted to characterize surface fracture energy despite its complexity.

### III.3. Wedge splitting test

In order to characterize the stable crack propagation and to evaluate the surface fracture energy of refractories with coarse aggregates, specimen with large fracture surface

size should be used. To do so, “wedge splitting test” (WST) has been developed by Tschegg (Tschegg, 1986) and has been used by a numerous research centres and universities (Harmuth et al., 1996; Guinea et al., 2002; Ribeiro et al., 2010).

As other testing methods like notched beam test and compact tension method, WST consists of opening a crack using a wedge in mode I. The principle of this test is to apply a vertical force  $F_V$  which is transformed to a horizontal one  $F_H$  causing a symmetrical opening mode of the crack by an angular wedge. The set-up of the WST is presented schematically in Figure II-7a. The specimen is placed on a linear support, which is fixed on the lower plate of the testing machine. The use of rolls improves significantly the accuracy and reproducibility of results (Brühwiler et al., 1990) and allows reducing the intensity of friction. Dimensions of parts assembly are detailed in Figure II-7b. It was elaborated from hardened steel Z160CDV12 of 60 HRC.

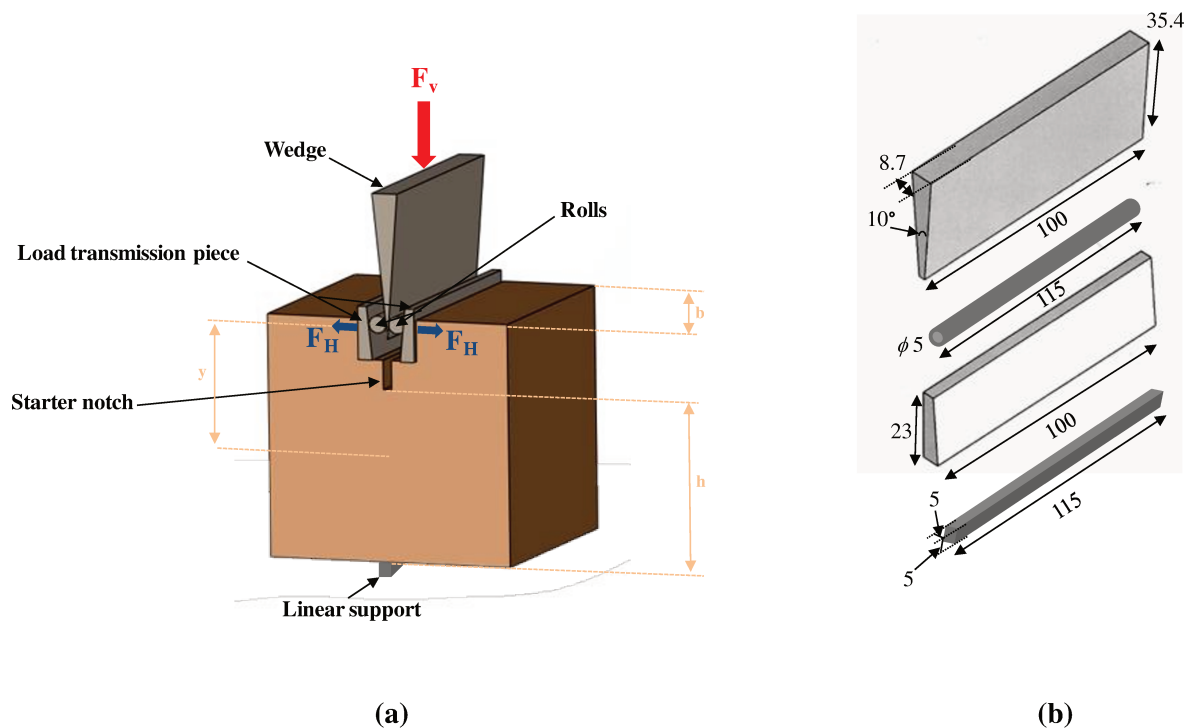


**Figure II-7: Wedge splitting test device (a) with dimension of parts assembly (b)**

Figure II-8a represents a cracked WST sample and the stress distribution during the test. The crack onsets and propagates thanks to tensile stresses induced by  $F_H$  (Figure II-8b), besides, the lower part is submitted to compressive stresses.

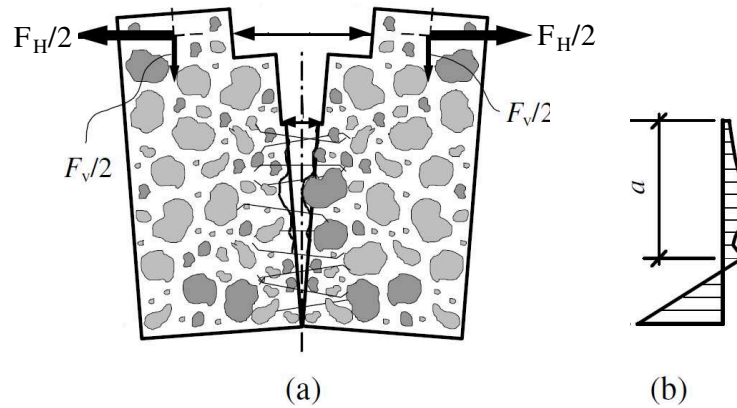


**Figure II-8: Schematic representation of wedge splitting test: (a) cracked specimen, (b) stress distribution in specimen (a is crack length) (from Löfgren et al., 2007)**

$F_H$  is calculated from  $F_V$  taking the wedge angle  $\alpha$  into account and neglecting any friction effects due to rolls:

$$F_H = \frac{F_V}{2 \cdot \tan(\alpha/2)} \quad \text{Eq. II-13}$$

The horizontal force  $F_H$  is much higher than vertical one to reduce the machine applied load and thus allows storing less elastic energy in the frame.

First, experimental results can be used to characterize material strength. This strength is called the nominal notch tensile strength ( $\sigma_{NT}$ ):

$$\sigma_{NT} = \frac{6 \cdot y \cdot F_{H,\max}}{b \cdot h^2} + \frac{F_{H,\max}}{b \cdot h} \quad \text{Eq. II-14}$$

where  $b$  (m) and  $h$  (m) are sample dimensions.  $F_{H,\max}$  (N) is the maximum horizontal force and  $y$  (m) is the distance between the fulcrum of  $F_{H,\max}$  and the middle of  $h$  shown in Figure II-7. The surface fracture energy  $G_f$  ( $\text{N}\cdot\text{m}^{-1}$ ) is defined as the mean work per unit of projected fracture area required to propagate a crack.  $G_f$  is calculated using the following equation:

$$G_f = \frac{1}{A_f} \int_0^{\delta_{1.5\% F_{H,\max}}} F_H d\delta_H \quad \text{Eq. II-15}$$

where  $A_f$  is fracture surface,  $F_H$  is the horizontal force and  $\delta_H$  is the horizontal displacement. This surface fracture energy is calculated for  $\delta_H$  values from zero up to the displacement corresponding to 10%~15% of the maximum load which suppose a full crack opening (Figure II-9).

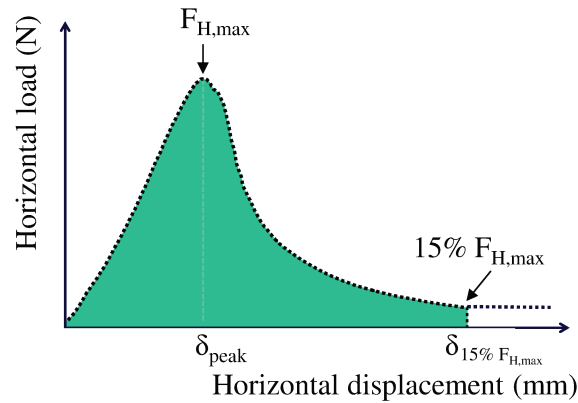


**Figure II-9: Calculation of the surface fracture energy using WST from a typical obtained load-displacement curve**

All the mechanical tests (bending, Brazilian and wedge splitting) were done using an Instron 5969 electromechanical press with a loading cell of 500 N or 50 kN.

## IV. Application of optical methods

### IV.1. Digital image correlation

As highlighted in chapter 1, DIC is one of the most common techniques used for kinematic fields measurements. Using reasonable experimental means, it allows measuring displacement fields from the degree of similarity between two images corresponding to different states of mechanical solicitation. One related to a reference state and the other to a deformed state. Both of them are recorded in the same conditions, the sample surface texture is supposed to be passive and doesn't change during mechanical load. From the difference between these images, the measurement of global and local material displacement is obtained.

DIC computation is based on the definition of many parameters such as the ZOI, correlation windows size and scale factor. The ZOI, in which the calculation is done, is

divided into many correlation windows whose size and number determine measurements density. These windows contain a number of grey levels. Each window is supposed unique. The windows can be square or rectangular, located next to each other or overlapped. The shape and size of these windows should be carefully chosen in accordance with calculation aim.

Displacements are defined by a plane material transformation  $\phi$  linking the coordinates of the reference state ( $\underline{X}$ ) to the deformed state ones ( $\underline{x}$ ) by the following equation:

$$\underline{x} = \phi(\underline{X}) \quad \text{Eq. II-16}$$

The degree of similarity between  $f$  and  $g$ , which correspond respectively to the grey levels of the reference and the deformed states, is given by the minimization of the correlation coefficient  $C$  (Doumalin, 2000; Bornert et al., 2008; Barranger et al., 2012):

$$C = 1 - \frac{\sum_{\underline{X} \in D} (f(\underline{X}) - \overline{f_D}) \cdot (g(\phi(\underline{x})) - \overline{g_D})}{\sqrt{\sum_{\underline{X} \in D} (f(\underline{X}) - \overline{f_D})^2} \cdot \sqrt{\sum_{\underline{X} \in D} (g(\phi(\underline{x})) - \overline{g_D})^2}} \quad \text{Eq. II-17}$$

where  $\overline{f_D}$  and  $\overline{g_D}$  are the averages of grey levels on correlation window in its reference ( $D$ ) and deformed  $\phi(D)$  state. The  $C$  value decreases with the optimization of the degree of similarity.

Four-points bending, Brazilian and wedge splitting tests have been coupled to digital image correlation to obtain kinematic fields on sample surface during material mechanical characterization.

The following paragraphs describe different steps and critical points which require a great attention.

#### IV.1.1. Sample preparation

A great attention must be paid to sample surface preparation in order to avoid artefacts of correlation results between deformed and reference states. To do so, the dynamic signal of the image has to be between 0 and 255 avoiding saturation in white or in black.

In some cases, the contrast is obtained directly using the natural texture of specimen surface, but its existence is not always guaranteed. To overcome this problem, an artificial preparation of the specimen surface called “speckles” is to be used on the material surface to highlight the contrast. This can be obtained using an aerosol spray, an airbrush or other means (Figure II-10). The airbrush is useful as it can control droplets size and the aerosol spray allows obtaining optimized results according to the user experience.



**Figure II-10: Different ways to obtain speckles: aerosol spray (a), airbrush (b)**

A black (or white) paint layer is spread on specimen surface, and after drying, fine white (or black) droplets are projected in order to ensure a good contrast (Figure II-11).

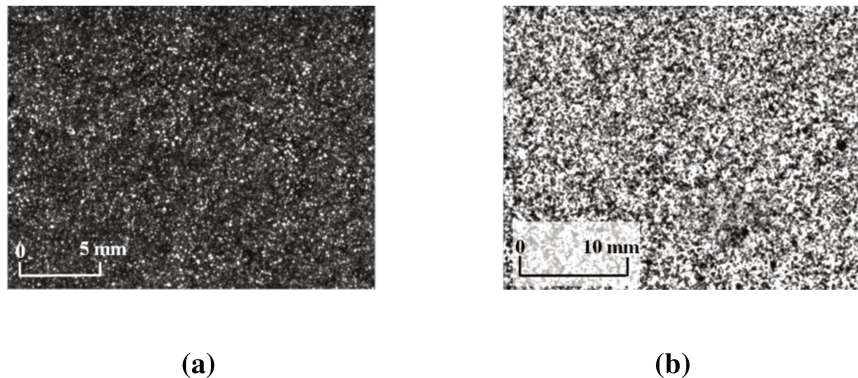


**Figure II-11: Examples of speckled surfaces: (a) white droplets on a black layer; (b) black droplets on a white layer applied on the surface of magnesia spinel materials**

Droplets has to be randomly spread and their size is variable (contain around 3~15 pixels). Speckles should also cover the overall range of greyscale distribution. It is preferable to use the full greyscale distribution. The quality of speckles has a great influence on the accuracy of results as will be explained in the paragraph “experimental key points”.



### IV.1.2. Image acquisition

A digital 8-bit IDS UI-1480SE-M-GL CMOS (Complementary Metal Oxide Semiconductor) USB2.0 camera (2560x1920 pixels<sup>2</sup>) is used to record speckled specimen surface during loading in order to perform optical measurements. CMOS is constituted by a matrix of photosensitive cells that retain their charge and convert it by themselves in tension. These cells in the case of CCD (Charge Couple Device) captor transfer the charge line by line to a manifold which transfers the entire charge to the converter. CMOS are much more compact than the CCD. For this reason, CMOS based cameras are smaller than the CCD ones. These latter are known with their high efficiency but allow slow acquisition speeds in comparison with CMOS.

As DIC is based on the comparison of grey level images, monochrome (black and white) images satisfy the DIC purpose and at the same time avoid the complexity (and inaccurate) of full colour image treatment. An optical lens Fujinon 1:1.8/50 mm has been used to guarantee a sufficient light source and to minimize optical distortion.

The camera (Figure II-12) is related to the acquisition software “Defpac” which was developed by Pprime Institute of Poitiers University (Bretagne et al., 2005b). It is preferable to link the camera to the computer around 30 minutes before starting the acquisition to ensure a thermal stability of the device. Image number is synchronized with mechanical load values (from load cell) using a National Instrument USB-6210 DAQ which receives an analogical signal from the electromechanical machine (0-10 V) and converts it to a numerical one. Image acquisition frequency adopted is 1 image per second.

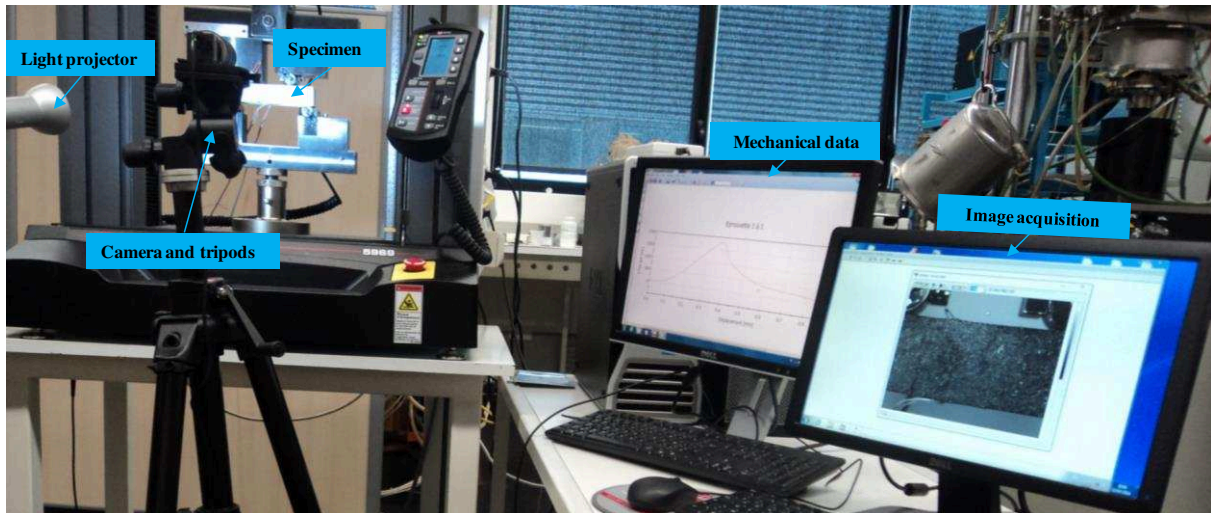


**Figure II-12: Digital image acquisition of a speckled instrumented sample during four-points bending test**

#### **IV.1.3. Images analysis by DIC**

After recording digital images of the speckled material surface, the correlation algorithm implemented in the software “Correla” measures the degree of similarity between selected images (reference and deformed ones, Eq II-17). “Correla” is developed by Pprime Institute of the University of Poitiers.

From the computation results, displacement fields (Figure II-13) can be represented using softwares of visualisation such as “Voxler” or “Surfer”. These softwares can easily combine data and display it using a variety of formats and colours. The accuracy and the quality of the represented displacement fields depend on the following parameters to be determined before running the computation:

- **ZOI size (horizontal  $h_{zoi}$  and vertical  $v_{zoi}$  size in pixels):** defines the area of sample in which the calculation will be done (Figure II-13).
- **Correlation windows size (horizontal  $h_{cor}$  and vertical  $v_{cor}$  size in pixels):** defines the number of correlation windows and so measurement point density. These correlation windows discretize the ZOI. They can be square or rectangular.
- **Correlation windows gap (horizontal  $h_{gap}$  and vertical  $v_{gap}$  gap in pixels):** determines if the windows are overlapped or not and the number of windows.

- **Scale factor (mm/pixel):** allows converting pixels to millimetres.

Using these parameters, correlation process allows the construction of displacement fields taking into account material rigid body motion that occurs between the reference images and deformed ones.

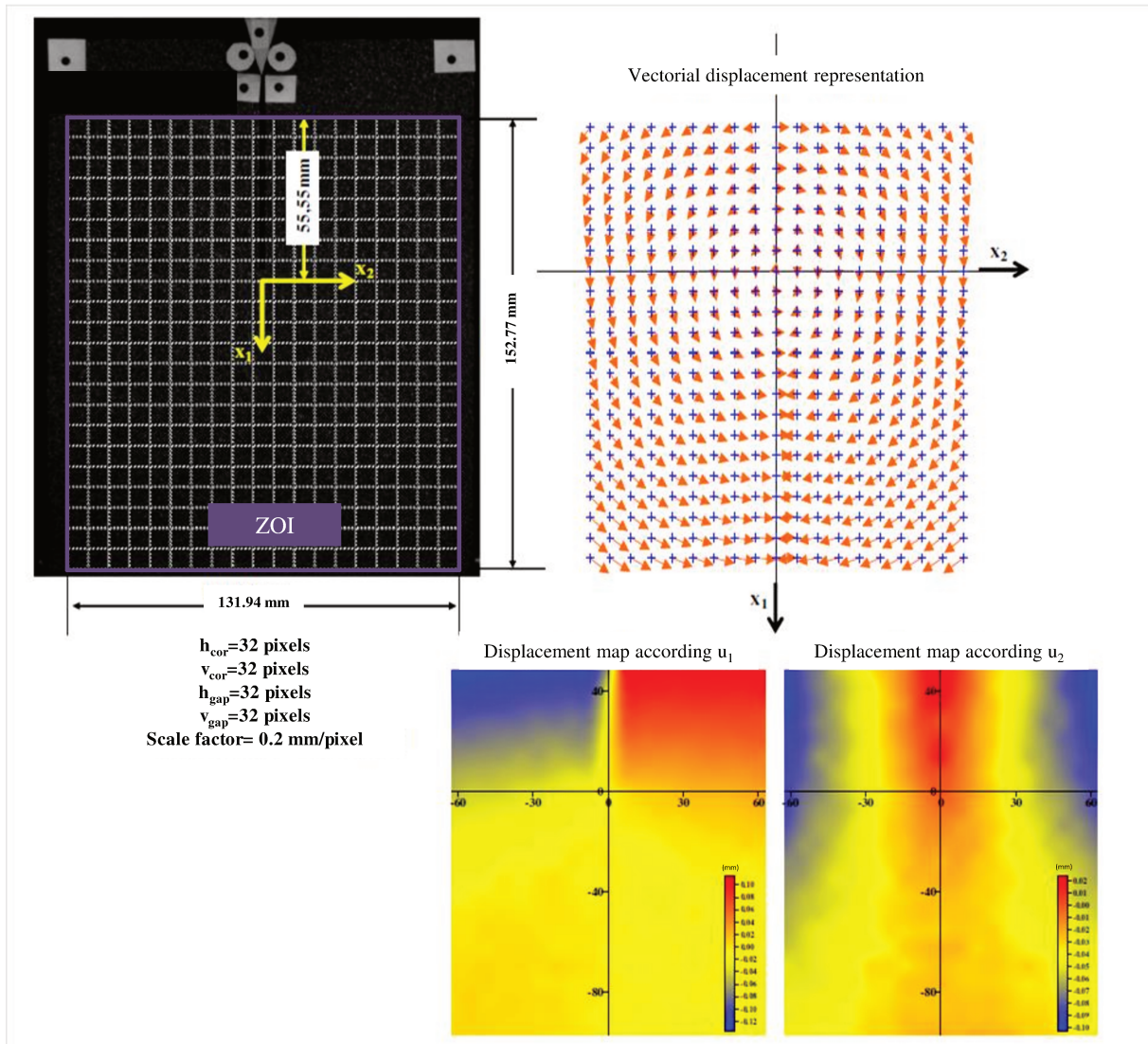


Figure II-13: Example of displacements representation obtained by DIC (from Pop, 2013)

#### IV.1.4. Experimental key points

As the majority of mechanical tests, a great attention has to be paid to the experimental conditions in order to avoid external sources of measurement errors. This point is more

critical as strain-to-rupture of studied refractory material is low and requires high measurement accuracy.

#### IV.1.4.1. Influence of sample preparation and processing parameters

An accurate DIC calculation requires appropriate digital images of a well prepared sample. Indeed, the quality of DIC measurements depends on sample surface and processing parameters. For instance, correlation windows size is chosen taking into account speckles quality and the ZOI. Each window should contain enough droplets and each droplet must have around 3~15 pixels (Barranger et al., 2012). Otherwise, correlation problems may occur. Figure II-14 illustrates a DIC stress-strain curve containing experimental disturbance. Stresses and strain values were obtained, respectively, from the electromechanical machine and DIC computation. It can be due to a lack of information in terms of pixels in the analysed droplets and so in correlation windows. This makes it difficult to evaluate the correspondence between the reference and deformed states. To overcome this problem, larger windows of correlation and an optimized speckled surface can be preferred (Figure II-15).

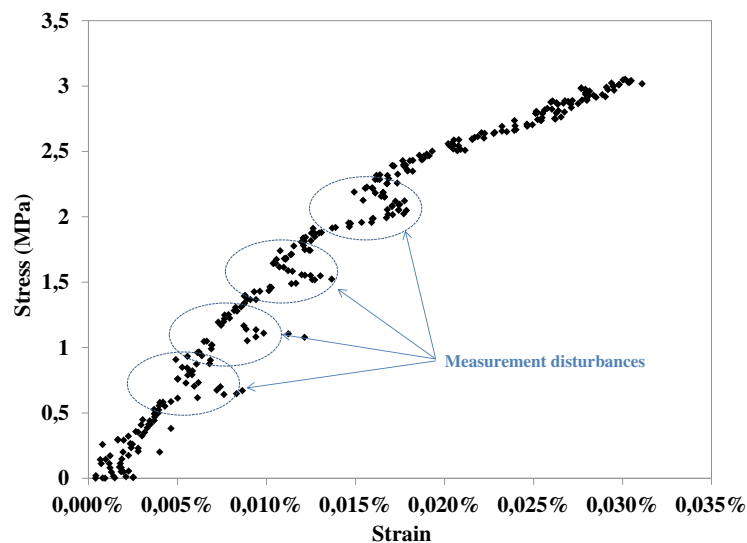


**Figure II-14: DIC tensile stress-strain curve obtained containing experimental disturbance**

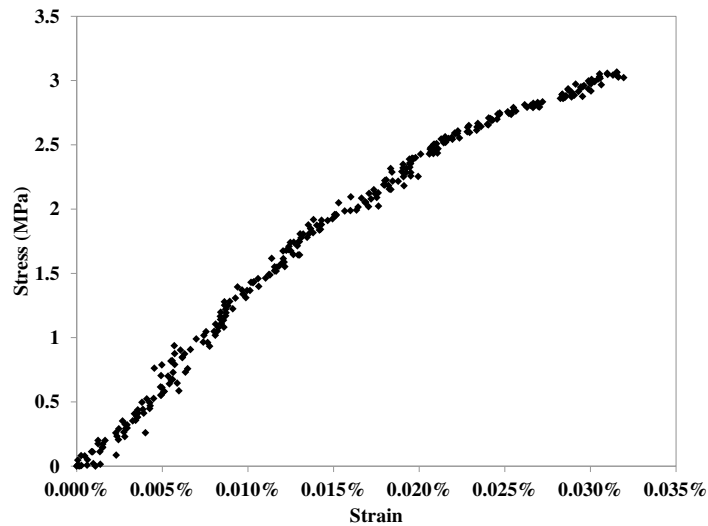


**Figure II-15: An improved DIC tensile stress-strain curve**

#### IV.1.4.2. Temperature variation effect

A study has been carried out to understand the influence of temperature variation of specimen during the mechanical test on strain measurement obtained by DIC. Light projector was one of temperature variation sources. Figure II-16 represent strains calculated on the surface of an unloaded refractory sample using respectively normal light projectors and cold light projectors. The frequency of acquisition is 1 image per 5 seconds. Temperature acquisition was done using K-type thermocouple placed near sample.

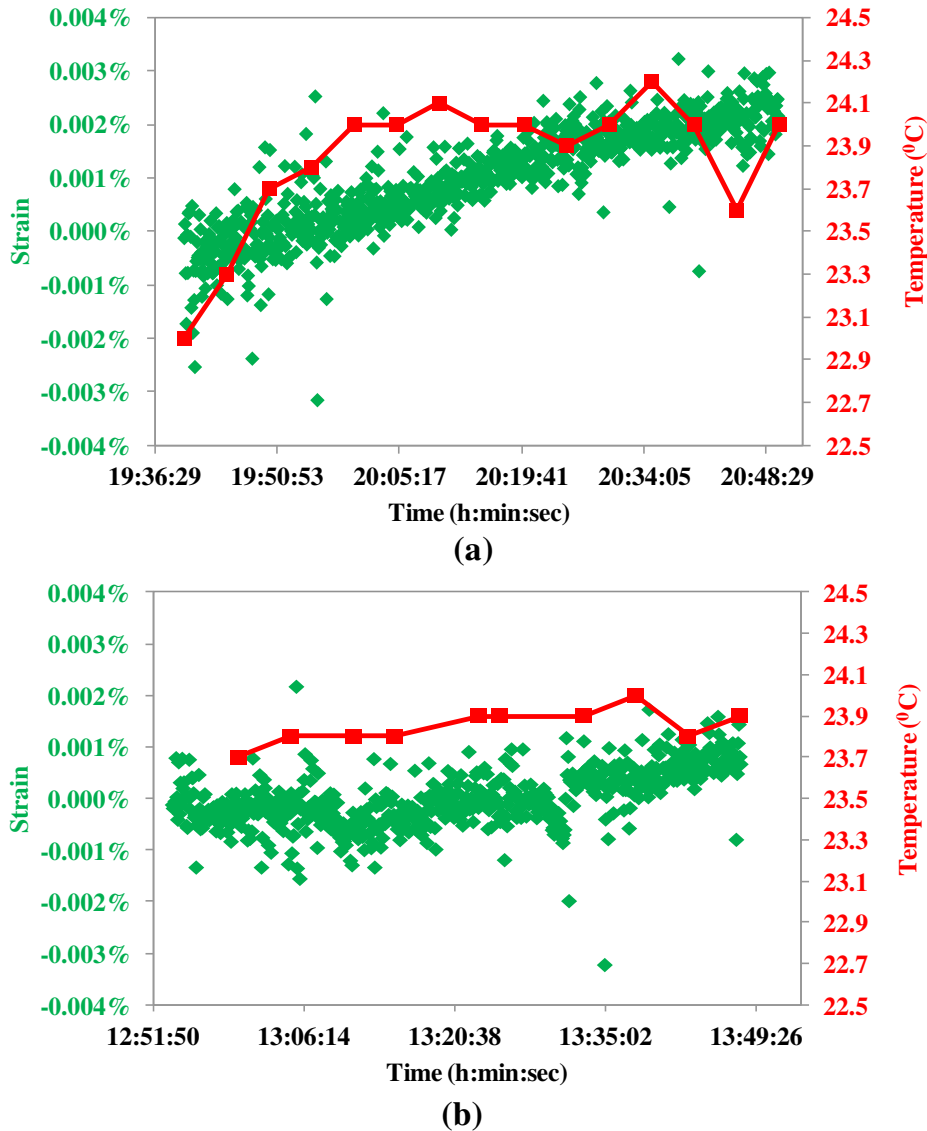


**Figure II-16: The influence of temperature variation on strain values evolution: (a) normal light projector, (b) led projector**

Actually, the use of suitable projectors enhance the contrast and the brightness of images grey level, however, some of them can be considered as the origin of temperature variation during acquisition. Halogen projector induces significant temperature variation during the test which leads to an increase of strain value due to thermal expansion (Figure II-16a). To overcome this problem, we preferred to use cold light projector (LED) for this work (Figure II-16b).



#### IV.1.4.3. Additional error sources

During image acquisition, all external sources of errors that can affect DIC strain values have to be eliminated. Figure II-17 compares DIC strain values measured on an unloaded sample surface in two configurations. One corresponding to a state in which additional parameters have been imposed such as walking around the camera and closing/opening laboratory door at different times, the other one is considered as a reference. In this latter, those parameters were not taken into account. A great attention should be paid to these parameters as they can have an influence on results quality.

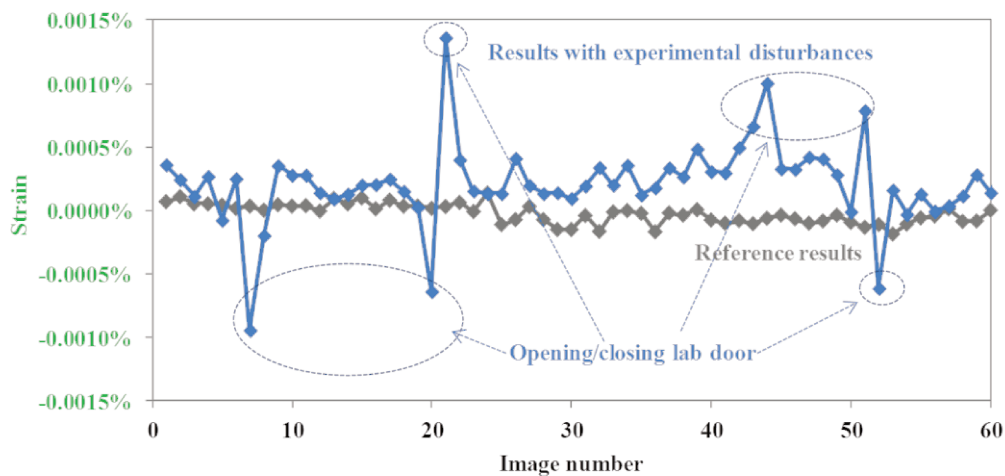


**Figure II-17: The impact of external disturbance sources on DIC strain values**

From the points detailed in the paragraph “experimental key points”, several parameters require a great attention during experimental testing. Taking into account this, and by optimizing the DIC analysis depending of calculation aim, DIC can lead to an accuracy of strain measurement around  $10^{-5}$  which is quite near from strain gage measurements.

## IV.2. Mark tracking method

To quantify the behaviour of four-points bending device in order to evaluate boundary conditions and their influence on the estimation of material properties, markers were deposited on inner and outer rolls. Markers colour has to be clearly distinct from support colour.

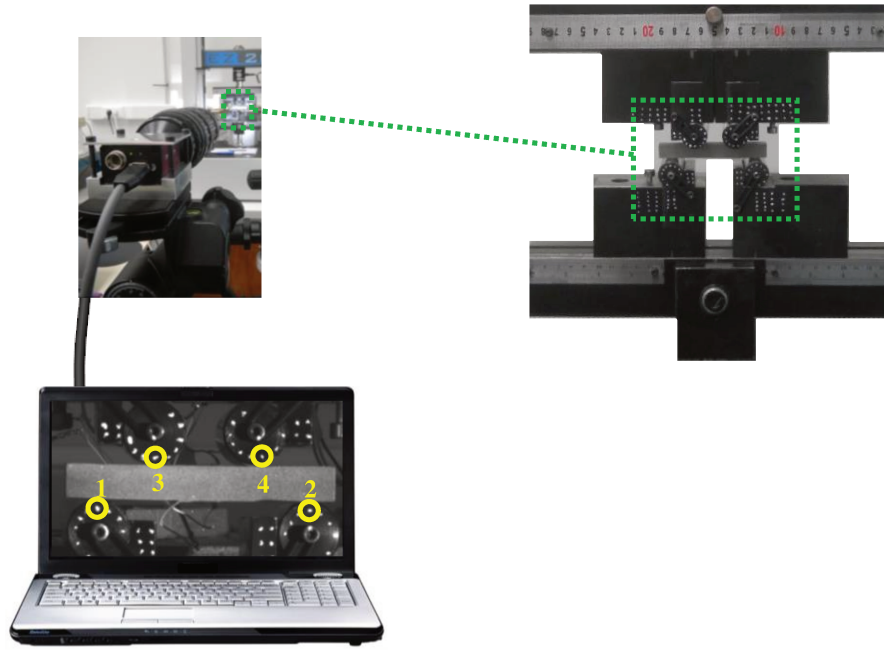


**Figure II-18: Mark tracking method application on four-points bending device**

After determining a threshold to distinguish markers from support, mark tracking method consists in following markers displacement during the test by calculating their geometric centres  $(x_g, y_g)$  pondered by the grey levels (PEM, 2015).

$$\left\{ \begin{array}{l} x_g = \frac{\sum_i \sum_j x(i, j)(I(i, j) - I_s)}{\sum_i \sum_j (I(i, j) - I_s)} \\ y_g = \frac{\sum_i \sum_j y(i, j)(I(i, j) - I_s)}{\sum_i \sum_j (I(i, j) - I_s)} \end{array} \right. \quad \text{Eq. II-18}$$



where  $I_s$  is the lower limit of the light intensity to distinguish if a pixel is a part of the marker or is a part of the background and  $I(i,j)$  the light intensity of the pixel whose coordinates are  $(x(i,j), y(i,j))$ .

As geometric centres of markers can be determined, it is possible to evaluate material rigid body motion from their displacements and rotations.

## V. Materials selection

Different materials with a non-linear mechanical behaviour have been chosen to develop and to valid the DIC approach of refractory mechanical characterization. Among the studied materials, a “flexible” model refractory material based on aluminium titanate developed for academic purpose has been considered. It develops a non-linear mechanical behaviour thanks to its thermal expansion mismatch according to the different crystallographic axis.

Besides, industrial partners of the project FIRE D suggested industrial magnesia refractories. These materials have been also studied as they exhibit a non-linear mechanical behaviour thanks to the thermal expansion mismatch between the different present phases.

### V.1. Why flexible ceramics?

As explained in chapter 1, the non-linearity of refractories or “flexibility” permits to admit large strain-to-rupture when they are submitted to thermo-mechanical solicitations. It is directly related to their microstructure design.

Itacolumite, which is frequently called “flexible sandstone”, illustrates a natural flexible material. Sandstone is a generic name of rocks constituted of sand grains (mainly quartz) integrated into natural cement. Itacolumite (Dusseault, 1980) is a particular case where quartz grains are angular and characterised by inter-granular spaces arranged like a puzzle. The cohesion of this material is not achieved by inter-granular mineral cement but by the morphology which allows some free motion from grain to grain into the void spaces as illustrated in Figure II-19 (Doncieux et al., 2008).

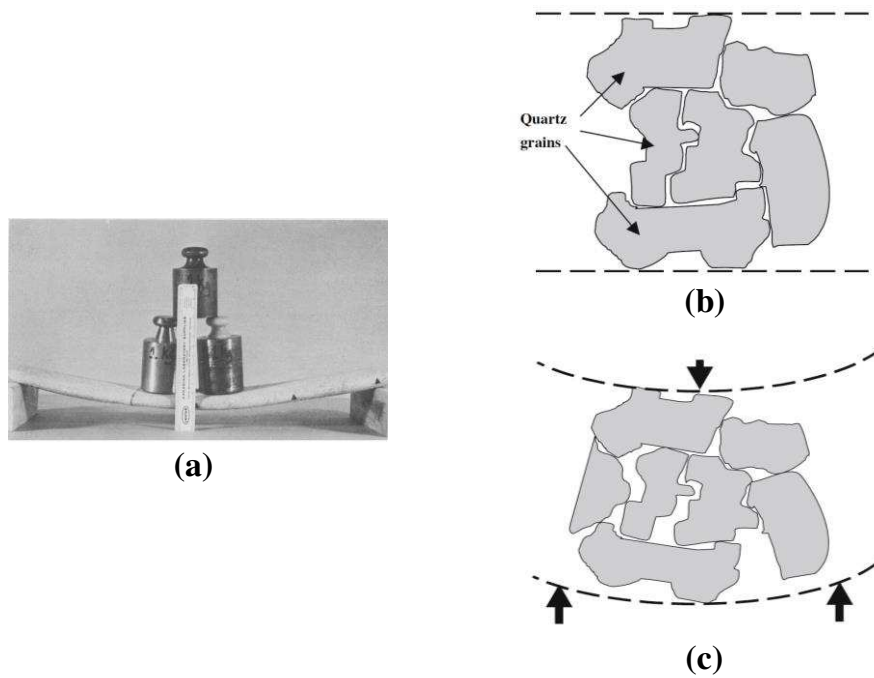


**Figure II-19: An Itacolomite deflecting under load (a) and a representation of its cross section in an unstressed state (b) and in a state under bending stresses (c) (from Dusseault, 1980 and Doncieux et al., 2008)**

For these reasons, Itacolomite, which is a natural material, has been used as a model for designing new refractory materials with large decohesions between constituents. This work did not study the Itacolomite, but focuses on refractories developed and inspired by mimicking this natural material. This is expected to improve thermal shock resistance of refractories.

## V.2. Aluminum titanate as a model flexible refractory

Due to its properties, aluminum titanate has been chosen as a model material to develop the flexibility of refractories by mimicking Itacolomite. This choice was done according to numerous reasons.

$\text{Al}_2\text{TiO}_5$  (AT) is a synthetic material of potential interest. It is obtained by synthesis of an equimolar mixture of  $\text{Al}_2\text{O}_3$  and  $\text{TiO}_2$  at temperatures above  $1280^\circ\text{C}$ . It is an excellent thermal shock resistant material thanks to its low thermal expansion coefficient and low Young's modulus (Babelot et al., 2009). Besides, it has a high melting point ( $1860^\circ\text{C}$ ).

However, AT materials have a relatively low mechanical strength due to micro-cracks induced by the high anisotropic thermal expansion of its grains after sintering. Along the a axis:  $\alpha_a = -2.9 \times 10^{-6} \text{ K}^{-1}$ , along the b axis:  $\alpha_b = 10.3 \times 10^{-6} \text{ K}^{-1}$  and along the c axis:  $\alpha_c = 20.1 \times 10^{-6} \text{ K}^{-1}$  (Babelot et al., 2009). Furthermore, pure  $\text{Al}_2\text{TiO}_5$  tends to decompose into  $\text{Al}_2\text{O}_3$  and  $\text{TiO}_2$  at temperature ranging from  $800^\circ\text{C}$  to  $1300^\circ\text{C}$ . The thermal stability can be improved by decreasing decomposition temperature and limiting its grain growth using some additives (Kim, 2010).

These properties make AT suitable for high temperature applications where thermal shock resistance are required. For instance, it is used in diesel particulate filters (DPF) (Figure II-20).

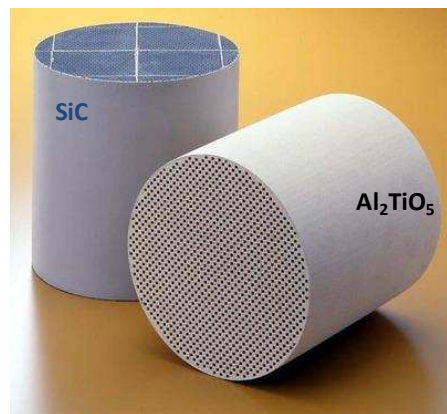


**Figure II-20: Examples of diesel particle filters**

The development of flexible AT was done in the framework of a previous study in which different thermal cycles were used to investigate the relationship between sintering cycles, microstructure and flexibility (Babelot et al., 2010). Indeed, three types of AT were elaborated; non flexible AT (AT NF), flexible AT (AT F) and very flexible AT (AT VF). AT NF has a quasi-brittle behaviour characterised by rather linear elastic stress-strain law as major ceramics. AT F and AT VF exhibit a non-linear “ductile” behaviour which leads to much larger strain to rupture. AT VF is more flexible than AT F and this flexibility is associated to a decrease in Young’s modulus (Babelot et al., 2009) as represented in Figure II-21.

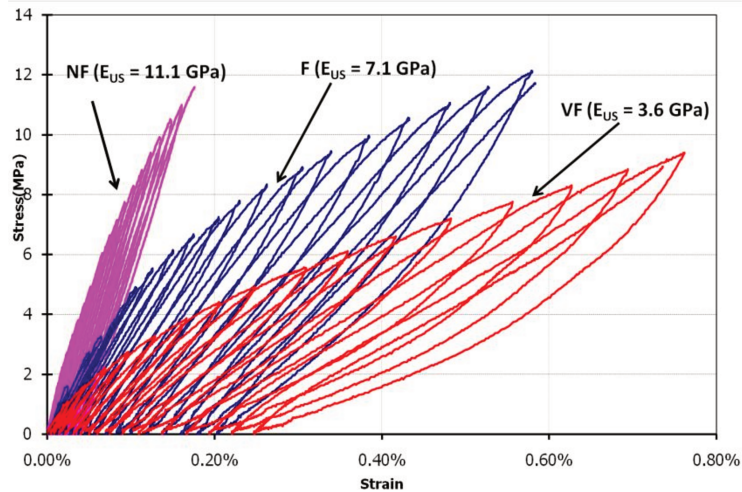


**Figure II-21: Stress-strain curves obtained by four-points bending tests for the AT samples (Babelot et al., 2009)**

This flexibility has been obtained by improving the grain growth. It generates a network of micro-cracks inside sample during cooling stage of sintering. The higher micro-cracks volume fraction is, the more flexible the material is. In this study, VF sample will be considered.

### V.3. Industrial flexible magnesia refractories

#### V.3.1. Materials containing spinel

Magnesia chromite refractories have been used over many years in a wide range of furnaces. They have important applications where a very high degree of refractoriness or resistance to basic environments is required, such as steel making vessels and rotary cement kilns. However, because of the toxicity of  $\text{Cr}^{6+}$ , the replacement of the chrome in these refractories is considered to be very desirable (Aksel et al., 2002).

For this reason, attention has been given to the use of spinel as an alternative to chrome ore. The mineral in the group of “spinel” are double oxides that crystallize in the cubic crystallographic system. They are generally indicated by the formula  $\text{AB}_2\text{O}_4$ , where “A” is a divalent element such as Mg, Fe, Zn, Ni, Co and Cu, and “B” a trivalent element such as

Al, Fe and Cr (Zhang et al., 2004). Among spinels associated with refractory systems  $MgAl_2O_4$  (Magnesium aluminate spinel called in general “spinel”) and  $FeAl_2O_4$  (Hercynite) can be quoted. Some of their properties are listed in the following table (Zhang et al., 2004).

**Table II-1: Properties of spinel and hercynite (from Zhang et al., 2004)**

	<b>MgAl<sub>2</sub>O<sub>4</sub> Spinel</b>	<b>FeAl<sub>2</sub>O<sub>4</sub> Hercynite</b>
Composition (wt %)	MgO 28.3	FeO 41.3
	Al <sub>2</sub> O <sub>3</sub> 71.7	Al <sub>2</sub> O <sub>3</sub> 58.7
True density (g.cm <sup>-3</sup> )	3.58	4.40
Melting point (°C)	2135	1450

### V.3.2. Magnesia spinel refractories

A further major advantage of magnesia spinel refractories is that they exhibit an improved thermal shock resistance unlike pure magnesia refractories, and it has been confirmed that (Ghosh et al., 2004) two to three times longer service life can be obtained, compared to a conventional magnesia-chrome brick. The reason for the improved thermal shock resistance has been linked to the large difference in thermal expansion coefficient between magnesia ( $\sim 13.5 \times 10^{-6} \text{ }^\circ\text{C}^{-1}$ ) and  $MgAl_2O_4$  ( $\sim 7.6 \times 10^{-6} \text{ }^\circ\text{C}^{-1}$ ). On cooling from sintering temperature (about 1700 C), the thermal expansion mismatch leads to micro-cracks development around the spinel grains (Aksel et al., 2002). Magnesia spinel refractory materials are used mainly in the cement kilns in particular in the cooling zone and the upper part of kilns (Figure II-22).

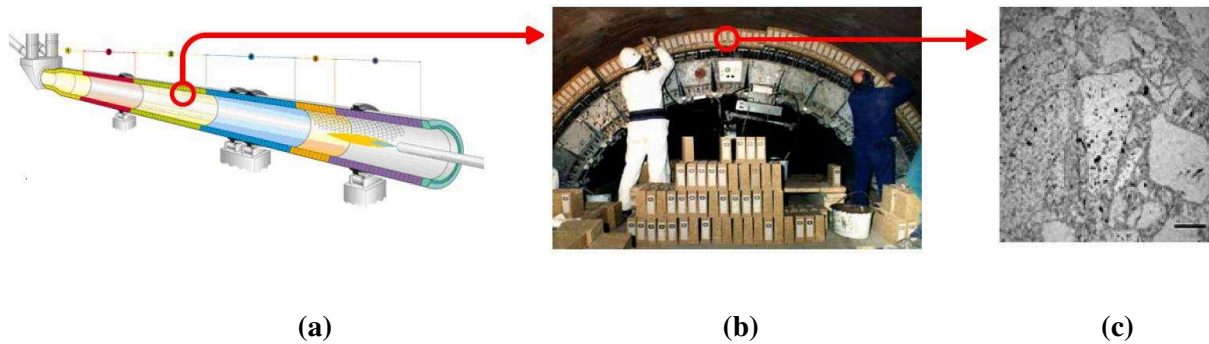


**Figure II-22: Industrial magnesia spinel refractories: Cement rotary kiln (a), installation of these materials (b) and microstructure (c) (Grasset-Bourdel, 2011)**

In order to apply DIC approach and to understand the mechanical behaviour of these refractories, different materials were elaborated (by RHI Company) and compared to a reference pure magnesia brick to understand the influence of spinel addition on crack process mechanisms and on their mechanical properties.

### V.3.3. Magnesia hercynite refractories

Magnesia hercynite refractory is also an important chrome-free refractory. It was found to increase the flexibility of based refractories (Liu et al., 2012). This is due to the thermal expansion mismatch between hercynite ( $10.3 \times 10^{-6} \text{ }^\circ\text{C}^{-1}$ ) compared to surrounding matrix (Lee et al., 1999). In addition to that, during firing, possible mechanisms related to the reaction between MgO and hercynite are possible. Among these phenomena, the diffusion of  $\text{Fe}^{2+}$  into MgO matrix and the partial diffusion of  $\text{Mg}^{2+}$  into the hercynite grains and thereby  $\text{Mg}^{2+}$  ions form a local  $\text{MgO-Al}_2\text{O}_3$  spinel with a surplus of MgO and the  $\text{Al}_2\text{O}_3$  from hercynite (Liu et al., 2012). Magnesia hercynite materials are used in cement kilns.

### V.3.4. Magnesia carbon refractories

Magnesia carbon refractories (MgO-C) are widely used in basic oxygen furnaces, electric arc furnaces and steel ladles. These refractories have an excellent slag resistance and thermal shock resistance due to the good properties of carbon. The slag cannot wet MgO-C structure because of the low wettability of carbon, so the service life of the MgO-C bricks increases.

In contact with molten iron and slag, the magnesia is modified by reaction with oxides present in the slag. To reduce the rate of chemical aggression, particularly slag corrosion and wear, the grains are embedded in a carbon material, which forms the so-called binder phase. For MgO-C materials, two kinds of binder are used; pitch binder and phenolic-resin binder.

Pitch is produced by distillation of high petroleum (Robin et al., 1998). It has a complex composition with a large number of polycyclic aromatic molecules mostly hydrocarbon in nature.

The second class of binder is generally composed of phenol-formaldehyde resins which polymerise at low temperature.

However, carbon tends to oxidize at high temperatures. After the oxidation of carbon, the structure of MgO-C brick is destroyed and the slag can penetrate into the structure. Therefore, metals, compounds or alloys so-called antioxidants are added during fabrication to prevent oxidation of carbon.

Several researchers have studied the oxidation behaviour of antioxidants. Aluminium is one of the most used antioxidant due to its low cost and effective protection. However, it has hydration problems when  $Al_4C_3$  forms, since this phase is easily hydrated, even at room temperature (Wang et al., 2001). The hydration of  $Al_4C_3$  causes volume expansion and cracks and is illustrated in Figure II-23.



**Figure II-23: MgO-C sample with an antioxidant Al before (a) and after (b) hydration**



This catastrophic phenomenon should be avoided with an accurate control of storage conditions in metallurgical applications.

An investigation of the mechanical behaviour of pitch and resin bonded MgO-C refractory materials has been carried out in order to understand the effect of thermal evolution and micro-cracking on mechanical properties of lining refractories. In this work, we would focus on variables that could mainly affect materials' flexibility due to the evolution of micro-cracking network. The idea is to fix aggregate's mix quality, mix size distribution, and impregnation conditions and to evaluate the effect of some variables such as microstructural evolution during operation, graphite content, binder type and presence of additives. The study will be completed by the use of DIC.

## VI. Conclusion

This chapter aimed to present the experimental characterization techniques and materials that exhibit a non-linear mechanical behaviour considered in the study. These materials, used for their high thermal shock resistance, exhibit such behaviour thanks to the network of micro-cracks present in their microstructure. In the present study, they were chosen in order to develop and to valid DIC for mechanical refractories characterization.

Among these materials, a model aluminium titanate samples, developed for academic purposes, have been studied (Chapter 3). Besides, industrial magnesia materials which exhibit a non-linear mechanical behaviour which have been proposed by FIRE project D partners (Chapter 4).

Elastic properties of each material will be determined using ultrasonic measurement at room temperature, than mechanical properties will be determined using four-points bending, Brazilian and wedge splitting tests. The main objective of this work was to complete the mechanical characterisation of refractories by coupling DIC to mechanical tests and to implement a FEMU-U numerical approach (Chapter 5).



# Chapter III

First application of DIC for the non-linear mechanical  
characterization of a model material: “very flexible  
aluminium titanate”

## I. Introduction

Aluminum titanate (AT) is a good candidate to develop flexibility of refractories due to its properties presented in chapter II. In the framework of a previous study, different types of AT with various degrees of flexibility were obtained by controlling sintering parameters: VF (very flexible), F (flexible) and NF (non-flexible). After a general presentation of these refractories and their preparation conditions, AT VF will be considered in this chapter.

During thermal shock solicitation, refractories are subjected to compressive and tensile loadings. Considering that, four-points bending test appeared as one of the appropriate experimental methods to investigate compressive and tensile behaviour at the same test. It has been coupled to DIC in order to better characterize the mechanical behaviour of AT.

This chapter aims to validate the DIC that allows obtaining kinematic fields. It permits completing the mechanical characterization and has been used for materials whose behaviour is non-linear with high strain levels such as alloys and plastics; however, its application on ceramics is still remaining not widespread.

Here, DIC will be applied on an AT VF sample that exhibits a high strain-to-rupture in comparison with common ceramics. Contrary to materials already characterized with DIC, it shows low strain levels (lower than 1%). In parallel, the boundary conditions of the loading system and their influence on material properties are experimentally evaluated thanks to mark tracking technique.

## II. AT as model material of flexible refractories

### II.1. Flexible AT preparation

AT VF, AT NF and AT F were elaborated from a granulated industrial powder (TM-20P, Marusu, Japan) in the framework of a previous collaboration with NITECH (Japan) by mimicking Itacolumite (Doncieux et al., 2008; Babelot et al., 2010). They have been shaped by uniaxial pressing with a pressure of 25 MPa. Each type has its own degree of flexibility thanks to its microstructure characterized with a specific grains size and different micro-cracking level. Table III-1 represents details about their preparation conditions and properties.

**Table III-1: Sintering cycle, microstructure characteristics, and mechanical properties of the three references of AT samples (from Babelot et al., 2010)**

		AT NF	AT F	AT VF
Sintering conditions	Sintering temperature (°C)	1500	1600	1600
	Dwell time (h)	1	8	16
	Cooling rate (h)	4	4	12
Microstructure	Grain boundary micro-cracking level	Partly	Totally	Totally
	Grain size (µm)	<20	<150	<200
	Micro-crack width (nm)	<100	<150	<500
Mechanical behaviour	Young's modulus (GPa)	11.7	7.1	3.6
	Strength (MPa)	18	16	13
	Deflection at rupture (mm)	0.27	0.7	1

According to (Babelot et al., 2010), for a  $T_s = 1500^\circ\text{C}$ , whatever the dwell time is, the samples have a low flexibility characterized with a poorly non-linear behaviour and a brittle rupture. At  $T_s = 1600^\circ\text{C}$ , the samples have a marked non-linear behaviour. Their flexibility increases and strength decreases between 1 and 8h of dwell time. From 8 to 16h of dwell time, the strength decreases but the flexibility still remains the same.

In addition to that, a slower cooling rate induces a higher flexibility as the micro-cracks width increases. In the same time, the strength of the samples remains relatively equal.

As a consequence, AT NF is partly micro-cracked as its grain size is low. The AT F grain growth is more important and thus grain boundaries are totally micro-cracked. AT VF, has a higher grain size than AT F due to a longer sintering dwell time and cooling rate. AT VF micro-cracks are wider, and so induce the possibility to support larger strain-to-rupture.

Young's moduli were measured by ultrasonic technique at room temperature. Strength and deflection at rupture were estimated by three-point bending tests made on parallelepiped samples ( $100 \times 12.6 \times 11 \text{ mm}^3$ ) with a constant crosshead displacement velocity of 1 mm/min. The mechanical behaviour is shown in Figure III-1. The AT NF sample has brittle behaviour without a post-peak occurrence, as typical ceramics. AT F and AT VF samples have non-

linear evolution that leads to a higher flexibility associated to a post-peak region which is more marked for the AT VF sample. This is why, this last reference was chosen.

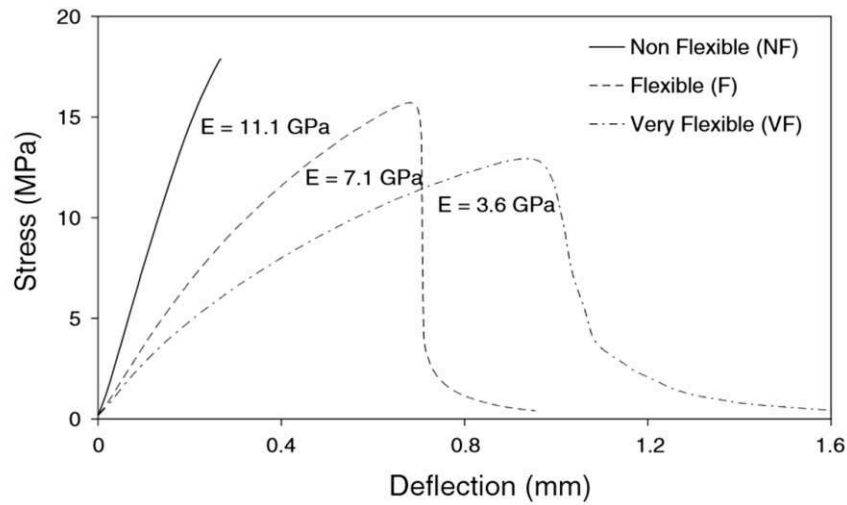


**Figure III-1: Three-points bending test results of the three types of AT samples. Young's moduli were measured by ultrasonic measurements (Babelot et al., 2010)**

## II.2. AT VF microstructure characterization

Figure III-2a represents the microstructure of AT VF obtained using scanning electron microscopy (SEM). AT grains (light gray) are surrounded by a silicate glass phase (dark gray) and porosity (black). After sintering, the microstructure becomes micro-cracked as represented in Figure III-2b, and this induces a flexible behaviour of such materials.

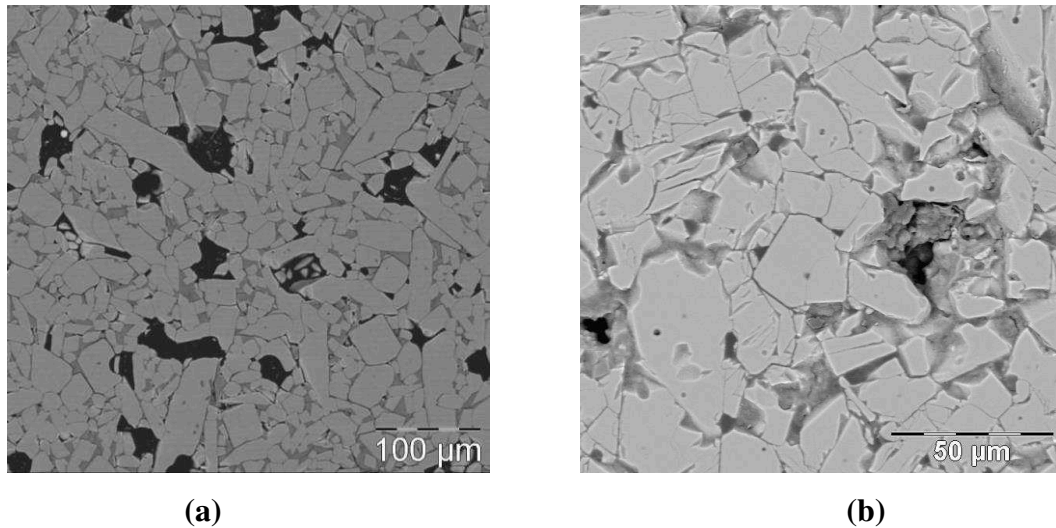


**Figure III-2: Details of AT VF microstructure with different magnification  
(Gallet-Doncieux et al., 2011)**

The micro-cracked microstructure of AT VF can be explained, as detailed in chapter I, by the occurrence of thermal stresses due to the high anisotropic thermal expansion coefficients ( $\alpha$ ) of AT VF grains according to the different crystallographic axis ( $\vec{a}$ ,  $\vec{b}$  and  $\vec{c}$  axis). As presented in chapter II, in the case of AT, the thermal expansion coefficient are :  $\alpha_a = -2.9 \times 10^{-6} \text{ K}^{-1}$ ,  $\alpha_b = 10.3 \times 10^{-6} \text{ K}^{-1}$  and  $\alpha_c = 20.1 \times 10^{-6} \text{ K}^{-1}$  (Babelot et al., 2009).

From chapter I: § II.1, different mechanisms occur according to the crystallographic axis and  $\alpha$ . Figure III-3 is a schematic representation of an equivalent homogeneous AT material whose average thermal expansion is  $9.6 \times 10^{-6} \text{ K}^{-1}$ . It allows explaining what is happening in the microstructure and especially between grains during cooling step after sintering.

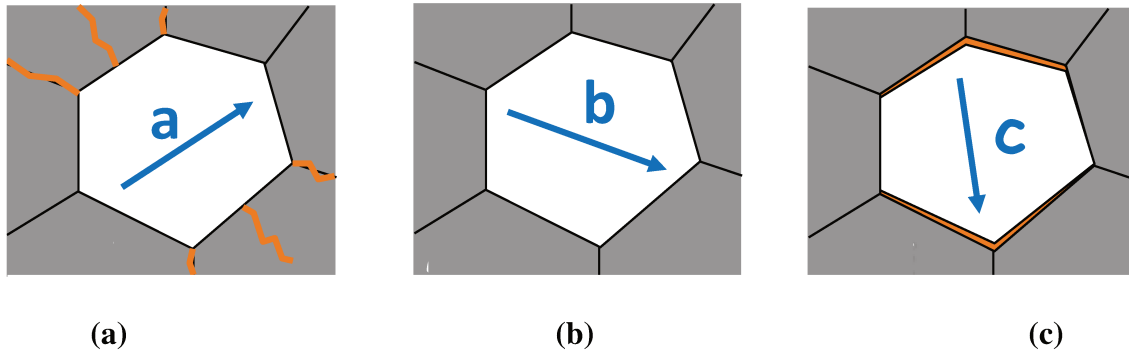


**Figure III-3: Microstructural mechanisms of AT occurring during cooling step depending of the central grain configuration: (a) micro-cracking, (b) absence of damage and (c) grain debonding**

- Along  $\vec{a}$  axis,  $\Delta\alpha = 9.6 \times 10^{-6} - (-2.9 \times 10^{-6}) = 12.5 \times 10^{-6} \text{ K}^{-1} > 0$

The grain have tendency to expand, and so there is a presence of radial compressive and circumferential (orthoradial) tensile stresses.

- Along  $\vec{b}$  axis,  $\Delta\alpha = 9.6 \times 10^{-6} - 10.3 \times 10^{-6} = 0.7 \times 10^{-6} \text{ K}^{-1} \sim 0$

There is quite thermal expansion coefficient equality, and so no internal stress appears during cooling, and thus, no damage is observed.

- Along  $\vec{c}$  axis,  $\Delta\alpha = 9.6 \times 10^{-6} - 20.1 \times 10^{-6} = -10.5 \times 10^{-6} \text{ K}^{-1} < 0$

A debonding of the interface can occur as the grain is subjected to radial tensile stresses and so a large ability of grain to shrink.

Thermal expansion mismatch between the material and grains along  $\vec{a}$  axis is positive (Figure III-3a). In this case, micro-cracks will be generated inside the microstructure as the grain will have tendency to expand. Along  $\vec{b}$  axis, thermal expansion mismatch is quite equal to zero, for this reason, there is an absence of damage (Figure III-3b). However, along  $\vec{c}$  axis, thermal expansion coefficient mismatch will induce a grain debonding (Figure III-3c).

Young's modulus evolution of AT VF versus temperature has been obtained using ultrasonic echography and represented in Figure III-4. The initial Young's modulus at room

temperature is around 4 GPa and its evolution at high temperature is a hysteresis cycle. During the increase of temperature, the micro-cracks initially present in sample are closing, then, the material tends to reduce its damage and so, Young's modulus values become higher progressively until 900°C. After that, they increase significantly until 1250°C. At higher temperatures, Young's modulus decrease as the glassy phase becomes less viscous. It can be noticeable that during cooling, Young's modulus values still remain high since micro-cracks are closed until reaching 700°C. After this temperature, they decrease due to the damage caused by the sudden reopening of micro-cracks.

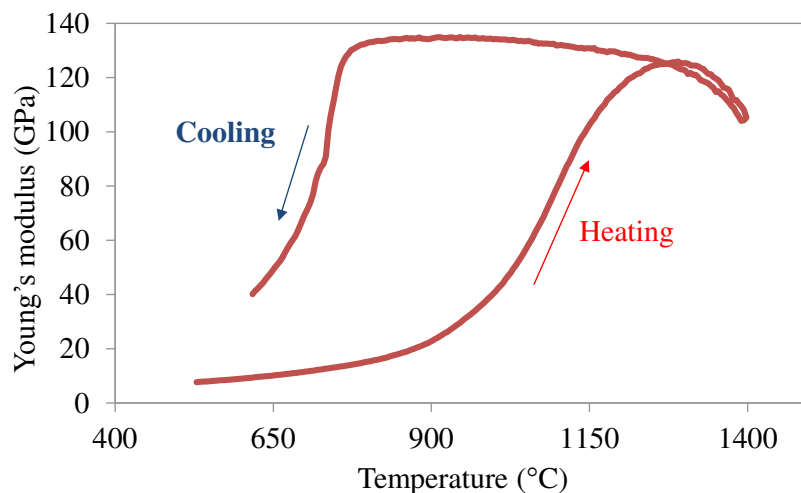


**Figure III-4: Evolution of AT VF Young's modulus versus temperature**

### **III. The application of DIC to investigate the non-linear mechanical behaviour of AT VF**

#### **III.1. Introduction**

The mechanical characterization of AT VF is done using four-points bending test. As mentioned before (chapter II: § III.1), this test suits well with the mechanical solicitations type and can be easily adopted in association to DIC as it permits to have plane surfaces submitted to stresses. The experimental configuration is coupled with DIC as detailed in chapter II: § III.1.

Tested AT VF specimens ( $85 \times 12.5 \times 10.5 \text{ mm}^3$ ) are obtained directly from sintering with a rectangular cross-section. To practice image acquisition, a sample preparation has been done using black and white speckles to enhance contrast of investigated surface. Firstly, a black opaque paint layer was deposited on material surface, then, white droplets were projected on (chapter II: § IV.1.1). Strain gages were glued on material upper and lower surface for strain measurements.

The frequency of image acquisition was 1 image per second. The applied loading rate is 0.5 mm/min.

In order to calculate rolls displacements and rotations (chapter II: § IV.2), different markers were drawn on rolls surface. Using mark tracking method, the measurement of markers displacement allows evaluating boundary conditions of the experimental configuration during the test.

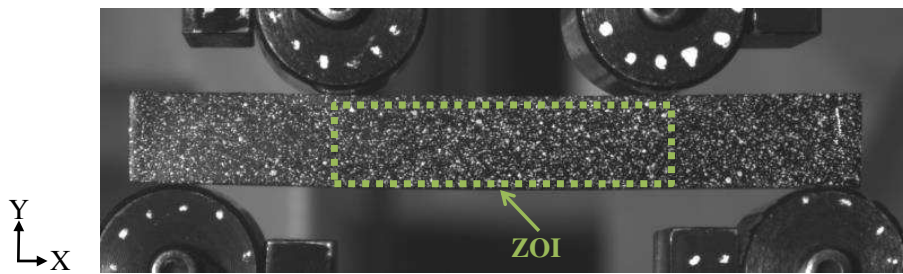


**Figure III-5: Speckles and markers are respectively visible on sample surface and on the rolls. Besides, ZOI is defined**

## III.2. Mechanical behaviour

According to Figure III-6, at room temperature, AT VF sample exhibits a large non-linear evolution which demonstrates a high flexibility.



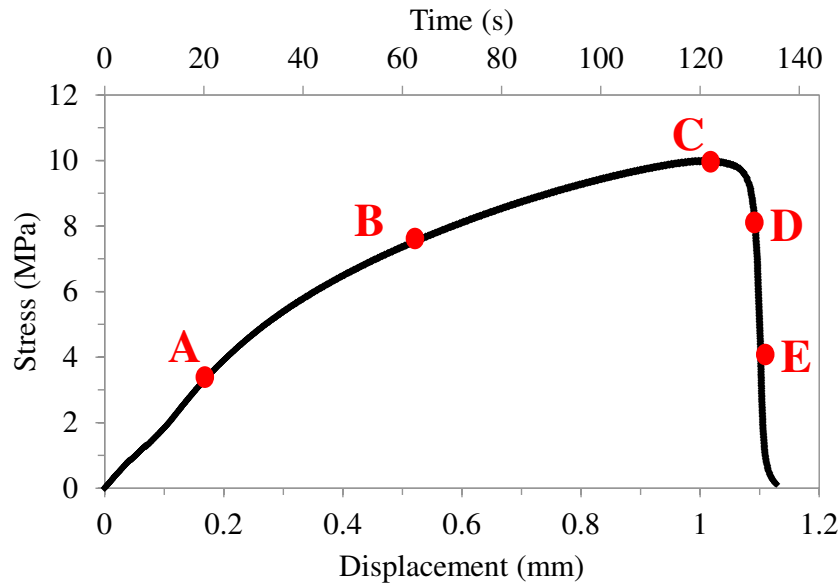


**Figure III-6: Stress-displacement curve of AT VF. The points A, B, C, D and E represent the five times chosen for full-fields strain measurements**

At the beginning of the curve, the mechanical behaviour is quite linear. This part is characterized with a symmetrical behaviour between tension and compression. For this reason, Young's moduli values presented in Table III-2 were calculated using strain gages (Hooke law) in this part of the curve.

**Table III-2: Stress-to-rupture and Young's modulus values obtained thanks to four-points bending test**

AT VF	
$\sigma_{\max}$ (MPa)	10.16
$E_{\text{tension}}$ (GPa)	5.21
$E_{\text{compression}}$ (GPa)	5.02

Since the applied stress reaches 4 MPa, the mechanical behaviour becomes non-linear that leads to a higher flexibility until its value is equal to stress-to-rupture given in Table III-2. The rupture is not brittle and the post-peak region is more marked.

### III.3. Asymmetric behaviour

In order to characterize strain distribution on AT VF sample surface during the four-points bending test, DIC has been used. Five longitudinal strain maps were presented at the different times indicated in Figure III-6. (A) corresponds to the end of the rather linear step, (B) is related to the non-linear zone, (C) is close to the peak, (D) and (E) represent crack propagation and material rupture. The ZOI chosen for DIC calculation is the area limited by the upper rolls centres and is enclosed in the dashed green rectangle shown in Figure III-5. The used correlation windows are  $32 \times 32 \text{ pixels}^2$  with a gap of  $8 \times 8 \text{ pixels}^2$  and factor scale equal to  $37.28 \mu\text{m}/\text{pixel}$  as schematically represented in Figure III-7.

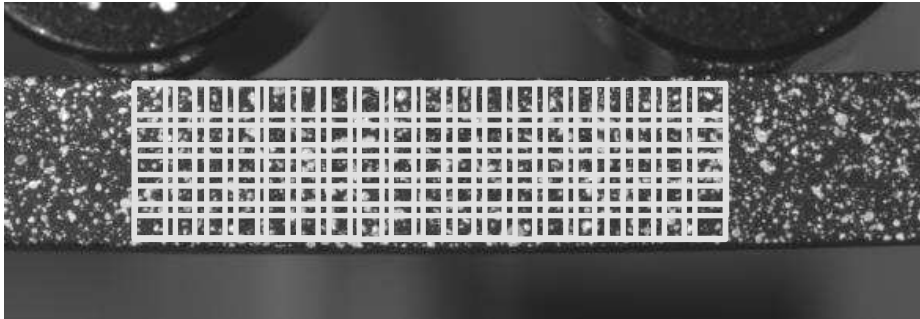


**Figure III-7: Schematic representation of correlation windows for strain map calculation**

DIC calculation has been done for the whole test, however, Figure III-8 shows the different maps of strain along X-axis obtained at the specific mentioned times in Figure III-6.

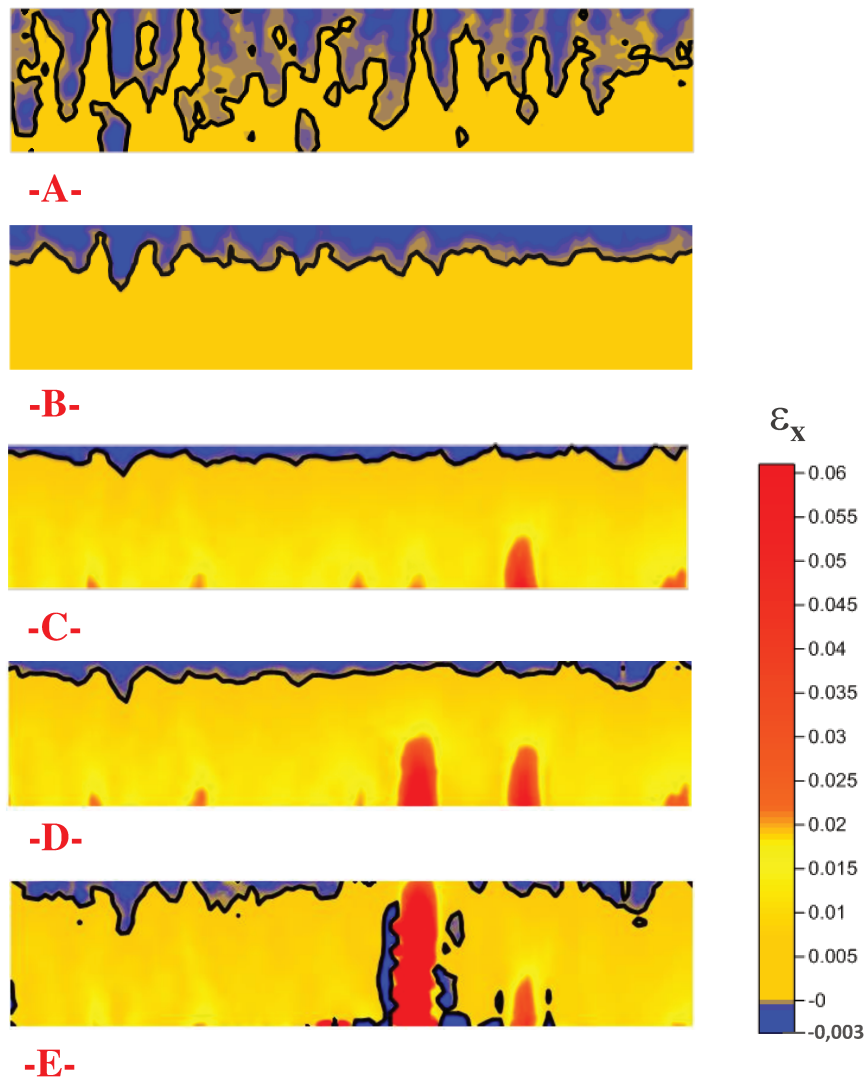


**Figure III-8: Maps of strains along X-axis for the five times defined in Figure III-5**

During the test, the upper part is submitted to horizontal compressive stresses, while the bottom is subjected to a tensile one.

At the beginning of the test (stage A) which corresponds to the linear part of the mechanical curve, compression and tension are balanced and are symmetrically distributed with respect to the zero stress line well known as “neutral fibre” represented with the black line in Figure III-8 and will be described after. It is worth to mention that measurement disturbance due to the low strain level induces a perturbation of neutral fibre localisation which should be a horizontal line in the middle of sample.

In stage B, which corresponds to the beginning of the non-linear behaviour, strains in the bottom of sample are becoming higher in comparison with the compressive strains inducing the asymmetric distribution of tensile and compressive stresses.

In stage C, the asymmetric behaviour is stronger and there is localisation of zones with high strain level which are concentrated where the crack may appear on the surface. Red color is not related to a real deformation, but corresponds to crack opening.

Stages D and E have been chosen in order to describe the post-peak behaviour of the material which appears as representative of not brittle material rupture.

In stage D, strain level around crack opening which will induce material rupture becomes higher in comparison with zones characterized with high strain level.

In stage E, this crack will propagate until material rupture. High strain values localised in the zones become low as the applied load is decreasing.

The evolution of these strain maps during the whole test has been represented in Figure III-9 and compared with a similar rectangular cross-section sample of aluminium alloy (2017A). These evolutions have been drawn using Voxler software from Goldensoftware.

From Figure III-9, distribution of compressive and tensile strains versus time is not the same and depends on material behaviour. Aluminium alloy exhibits a symmetric distribution of strains (Figure III-9a) unlike AT VF sample in which tensile strains become higher than compressive ones as the applied load is increasing (Figure III-9b).

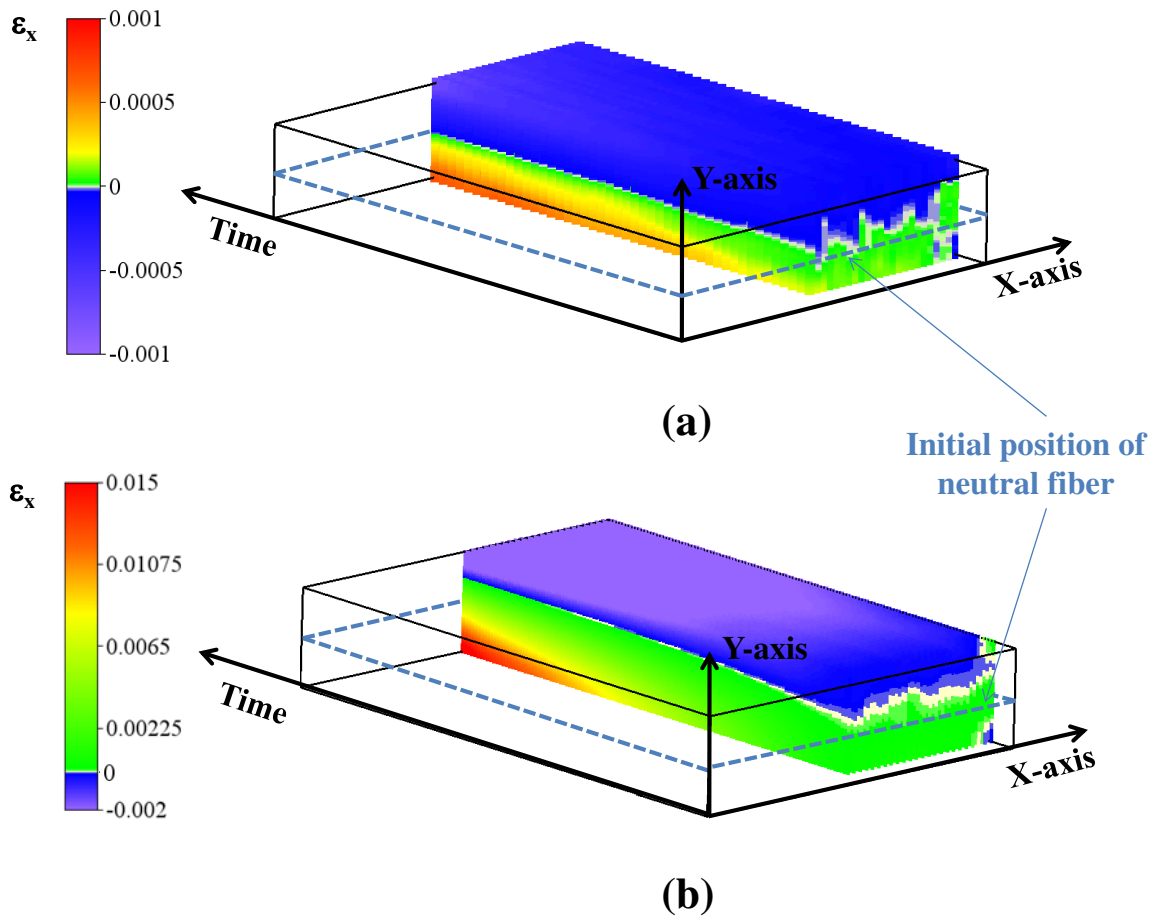


**Figure III-9: Evolution of strain fields during bending test:  
Reference aluminium alloy sample (a) and AT VF sample (b)**

### III.4. Neutral fibre evolution

The asymmetric behaviour of AT VF as shown in previous results has a great influence on localisation of the neutral fibre.

For the evaluation of neutral fibre evolution using DIC, strain fields evolution needs to be more accurate in deformation as explained before. To do so, the calculation has been done on two columns of correlation windows symmetric to the middle of sample as represented schematically in Figure III-10.

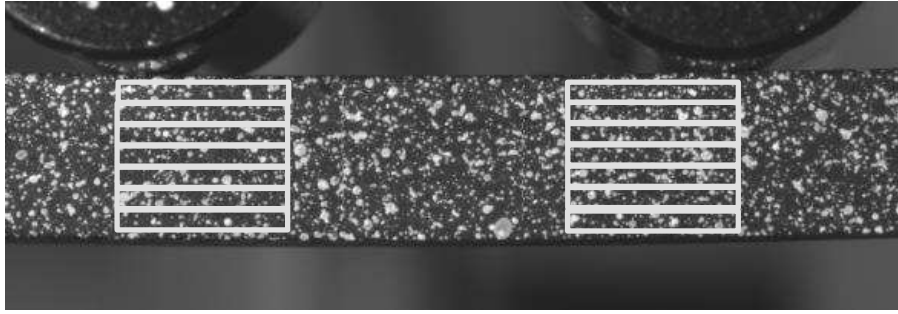


**Figure III-10: Schematic representation of correlation windows for neutral fibre evolution**

The correlation windows used are of  $256 \times 32$  pixels<sup>2</sup> with a gap of  $512 \times 32$  pixels<sup>2</sup>. The choice of these specific correlation windows has been done according to many reasons. As stress distribution is homogeneous along the horizontal direction on material surface, large windows were chosen. Besides, the high gap value was privileged so as to improve strain accuracy.

Figure III-11 represents strain field evolution for AT VF compared to aluminium alloy using the same ZOI. These maps were obtained thanks to Surfer software.

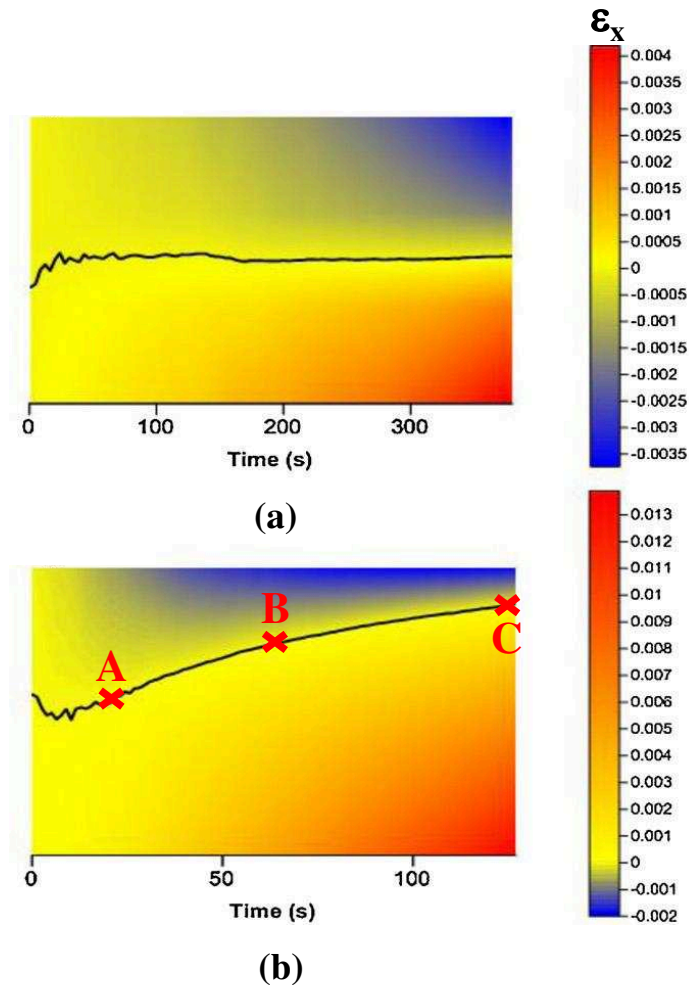


**Figure III-11: Evolution of strain fields during bending test for aluminium sample (a) and AT VF sample (b)**

At the beginning of the test, for both samples, neutral fibre is localized around the middle due to the symmetric tensile-compressive stress distribution. This part corresponds to an elastic behavior.

In the case of aluminium sample, this stress distribution still remains for the whole test and induces a constant neutral fibre position (Figure III-11a).

However, neutral fibre position for AT VF tend to move up from a specific stress value (Stage A in Figure III-11b) due to the asymmetric distribution of compression-tension stresses. This can be justified by the equality between the areas under compressive and tensile stresses which has to be satisfied. This explains the reason why the classical equation for

stress estimation and elastic properties determination are not valid in the case of such behaviour, and using FEMU-U introduced in chapter I may allow overcoming this experimental limitation.

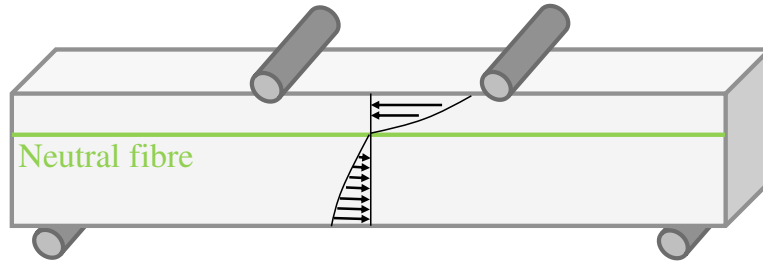


**Figure III-12: Asymmetric stress distribution during four-points bending test which induces neutral fibre shifting**

### III.5. Stress-strain behaviour

Strains on the upper and lower surfaces which are in contact with rolls have been measured using strain gages on another sample of AT VF. The values are here compared to DIC calculated on the upper and lower correlation windows as shown in Figure III-13. For this reason, it was necessary to improve the DIC accuracy of measurements by choosing specific correlation windows.

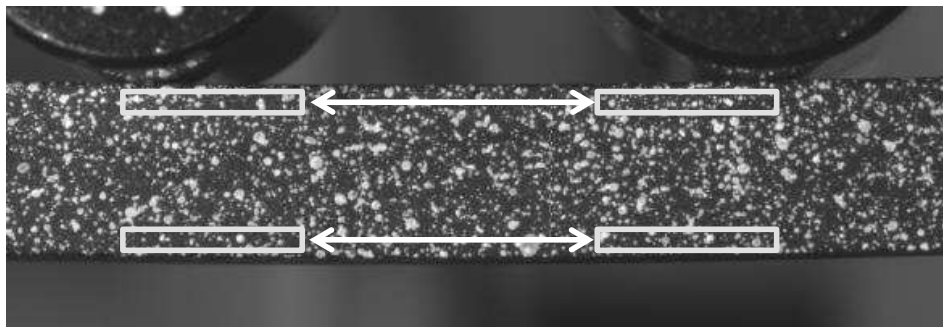


**Figure III-13: Schematic representation of correlation windows on AT VF sample**

The comparison between stress-strain curves is plotted in Figure III-14. Stress values are obtained using the Eq. II-6 which assumes symmetry between tension and compressive efforts.



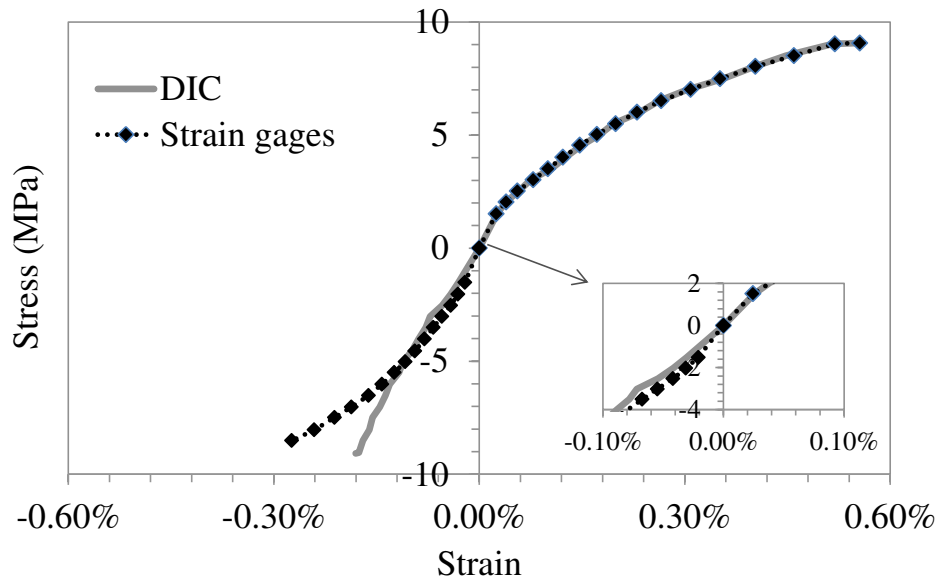


**Figure III-14: Comparison between experimental results of AT VF obtained using DIC and conventional gages**

From the very beginning of the test, Young's modulus values in compression and in tension have been evaluated and are presented in Table III-3. As shown in Figure III-14, tensile Young's modulus has been calculated up to 2 MPa and compressive one is estimated up to 4 MPa.

**Table III-3: Young's moduli values**

	Compression (GPa)	Tension (GPa)
DIC	4.52	5.28
Gages	5.02	5.21

Considering the overall measurement during the test, in one hand, strains obtained using DIC and gages (Figure III-14) show a good agreement. In the other hand, AT VF exhibits an asymmetric behaviour between tension and compression; this induces the neutral fibre shift as schematically represented in Figure III-12.

Unlike other ceramics, AT VF exhibits high level of strains, for this reason, it was possible to underline the efficiency of DIC technique. However, for other refractories, an improvement of the accuracy of DIC measurement is required.

### III.6. Energetic approach

After underlining the ability of AT VF high strain before rupture, and for a better understanding of the influence of damage on mechanical behaviour, an energetic approach has been applied so as to perform an investigation on dissipated energy. Four-points bending test is not devoted for such purpose in the case of brittle materials which have high and rapid release of energy. It has been applied here on AT VF sample as their behaviour can be considered as a specific case of the evolution of brittleness.

Figure III-15 represents the evolution of energy in terms of elastic, dissipated and total. The calculation is done using the energy evaluation principle explained in the case of WST in chapter II: § III.3.

Elastic energy is estimated by assuming that an elastic linear unloading of the material reaches the initial state before mechanical sollicitation. It corresponds to the area enclosed in a triangle whose vertexes are the origin of the curve, the displacement and the applied load. The total energy is calculated by integrating the load-displacement curve. Then, dissipated one is evaluated from the difference between total and elastic energies.

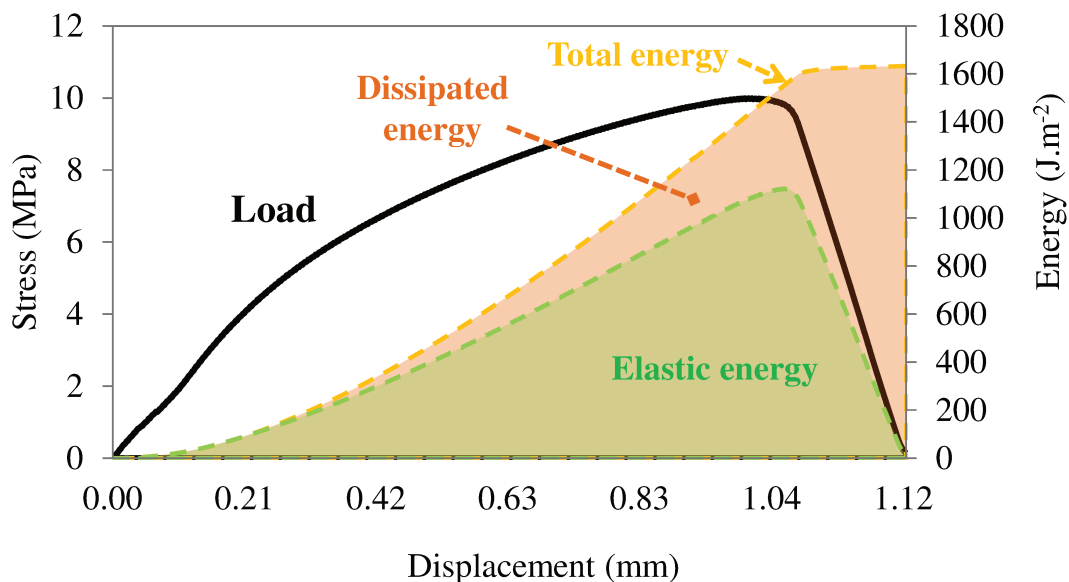


**Figure III-15: Estimation of elastic, dissipated and total energies for AT VF during four-points bending test**

At the beginning of the curve, the material is submitted to elastic solicitations, so the total energy is equal to elastic one. Since the curve started to become non-linear, the dissipated one appears due to the specific micro-cracked microstructure of AT VF. This energy is dissipated through different damage mechanisms occurring mainly in the following wake region as explained in chapter I.

The total energy becomes higher as the applied load increases until the crack initiation and propagation. After the peak, the total energy rises slightly when at the same time the elastic energy decreases.

### III.7. Bending device behaviour

During each experimental bending testing, different factors may have an influence on the evaluated results such as the presence of friction. To avoid this phenomenon, rolls of some bending devices are designed free to rotate along their axes (Figure III-16).

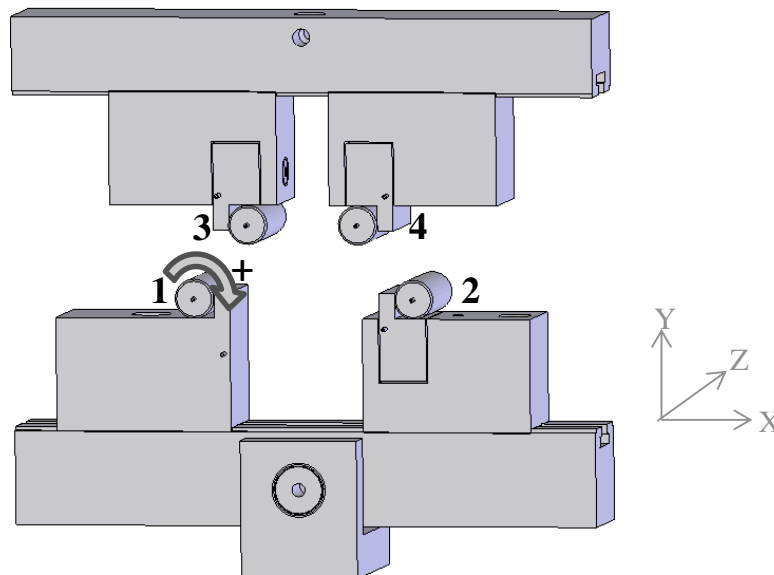


**Figure III-16: Designed four-points bending test with different degrees of freedom**

Taking into account stress distribution during this mechanical test, which means, the upper and lower parts of sample are submitted respectively to compressive and tensile stresses. Then, the upper (the lower) surface has tendency to be compressed (stretched).

As a consequence, it is predictable that rolls displacements and rotations will behave according to mechanisms occurring on these surfaces. For this reason, mark tracking method is used to quantify the behaviour of rolls and their influence on material properties.

Rolls rotation is obtained by measuring the displacement of two points diametrically opposite marked on each roll surface (Figure III-5). From this, rotation angles are determined using trigonometric relations and are presented in Figure III-17.

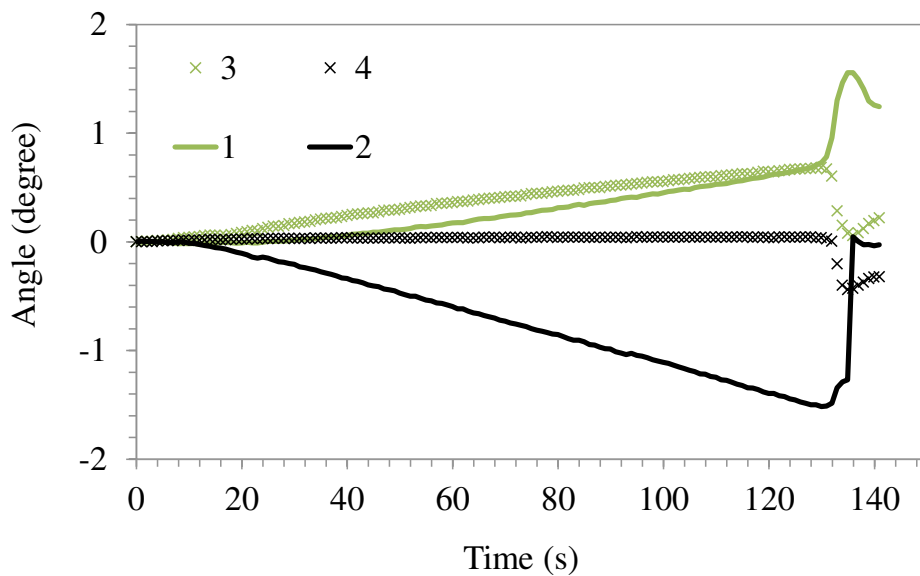


**Figure III-17: Rotation of rolls during the test**

Relative distance between rolls is estimated by measuring lateral displacement of one point on the surface of each roll numerated in Figure III-16. Figure III-18 represents the relative variation of the distance between lower and upper rolls observed during the test.

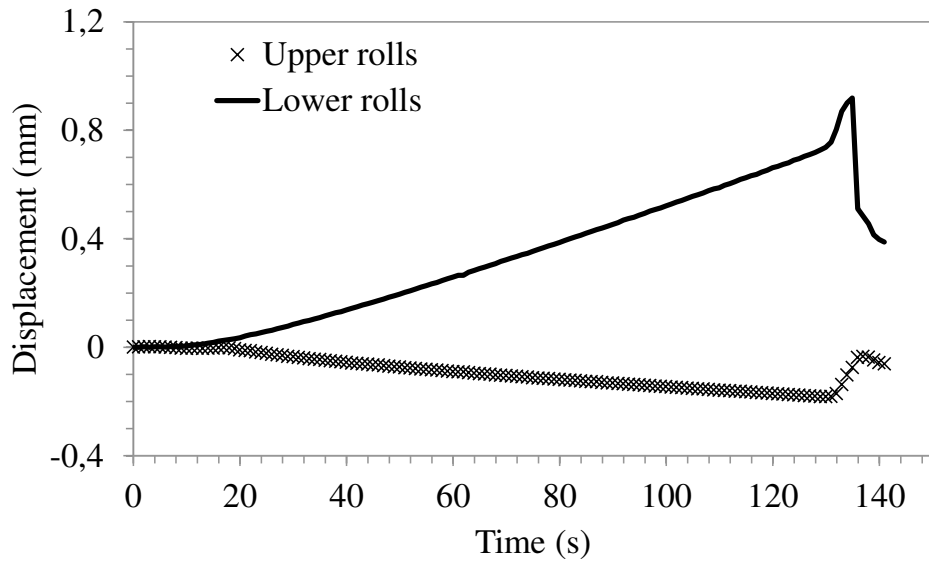


**Figure III-18: Evolution of relative distance between rolls**

Upper rolls become closer to each other due to compressive stresses presence unlike lower ones which tend to move away in the opposite direction owing to tensile stresses occurrence. This makes sense according to the stress distribution during a four-points bending test.

The equation Eq. II-6 used for stress calculation depends on the distance between rolls. Taking into account the results obtained by mark tracking method, its influence on material properties can be evaluated. It is quantified by comparing stress values measured between a configuration with and another one without taking into account rolls displacements. According to this, rolls movement yields to a stress variation of 2%.

## IV. Conclusion

The main objective here was to demonstrate the efficiency of this technique as an effective tool to complete the mechanical characterization of refractory materials.

Due to the lack of DIC skills in the laboratory, the first step was to acquire enough knowledge in this field and to master the technique. To do so, in this chapter we have

performed a preliminary study done on a single phase flexible material (AT VF) whose microstructure could be considered as a model for refractories to improve their thermal shock resistance.

This study highlights the asymmetric and non-linear behaviour of AT VF during four-points bending test at room temperature which is characterized by the shift of the neutral fibre. Besides, the relative variations of the distance between rolls and their rotations which permit avoiding friction are quantified using mark tracking method.

In the next chapter, DIC will be used to complete the characterization of multi-phased industrial refractories. These latter develop the flexibility, which is less accentuated than AT VF, thanks to the mismatch between thermal expansion coefficients of the different phases.

# Chapter IV

Application of DIC to characterize the non-linear  
mechanical behaviour of industrial refractories:  
case of magnesia based materials

## **I. Introduction**

In the previous chapter, as a first investigation, DIC has been applied to study the non-linear mechanical behaviour of a model aluminium titanate material. This step allows to master the DIC technique and to valid the efficiency of the technique in order to enrich the mechanical characterization of refractories.

In this chapter, the expertise developed previously over the DIC technique will be applied on different kinds of industrial refractories and especially on magnesia based materials. These materials, introduced in chapter II, are magnesia spinel and magnesia hercynite.

Magnesia spinel materials have been already investigated during the Ph.D. of Renaud Grasset-Bourdel (Grasset-Bourdel, 2011) which focused on the relationship existing between the microstructure and the associated thermo-mechanical properties. Here, thanks to DIC and WST, the influence of spinel addition on fracture mechanisms will be underlined.

However, the other types of materials processed by RHI have not been investigated in SPCTS laboratory yet. For this reason, a first characterization round has been conducted. Then, their mechanical behaviour investigation will be coupled to DIC.

## **II. Analysis of spinel addition influence on fracture mechanisms in magnesia spinel refractories using DIC**

### **II.1. Magnesia spinel materials description**

These industrial materials, already studied (Grasset-Bourdel, 2011), were simplified (MSp) and elaborated especially without any other constituent in order to understand the influence of spinel addition on the non-linear mechanical behaviour of magnesia refractories. Their processing was obtained using a maximum pressure of 140 MPa and a maximum sintering temperature of 1600°C.



As explained before (chapter II: § V.3.2), these materials exhibit a non-linear mechanical behaviour thanks to their microstructure represented in Figure IV-1. This matter of fact is due to the micro-cracking network developed by the thermal expansion mismatch existing between magnesia matrix ( $13.3 \times 10^{-6} \text{ K}^{-1}$ ) and spinel inclusions ( $8.9 \times 10^{-6} \text{ K}^{-1}$ ) in the range of 400-200 °C.

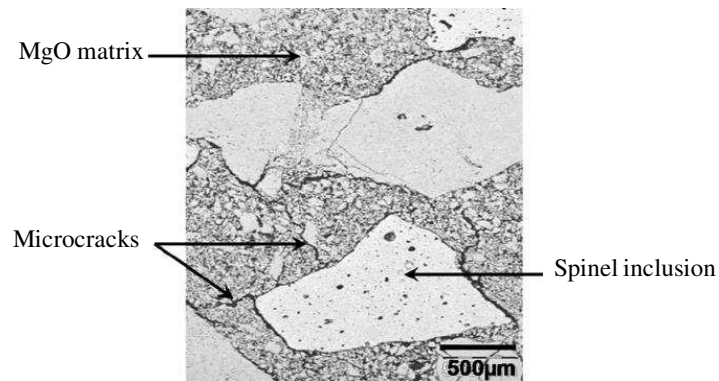


**Figure IV-1: Microstructure of a simplified MSp materials (Grasset-Bourdel, 2011)**

In the previous work, many MSp materials with different spinel rates were studied. Elastic properties were determined using ultrasonic measurements at room temperature and compared to the values calculated using Hashin and Shtrikman's model (Figure IV-2). This latter is dedicated to isotropic materials composed of a matrix and inclusion with perfect matrix/inclusion bondings.

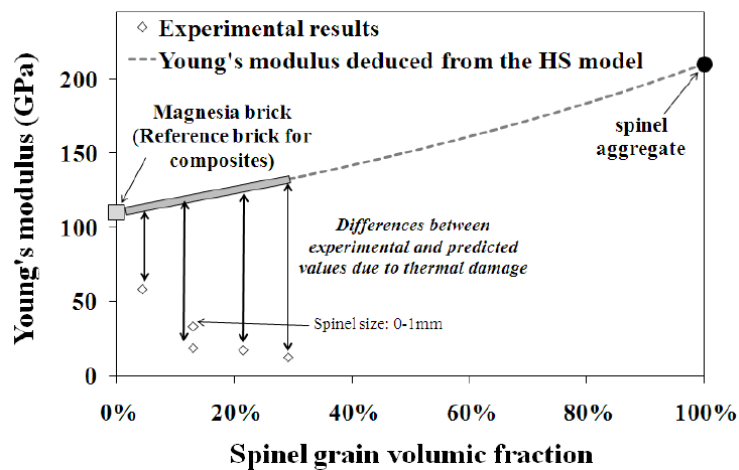


**Figure IV-2: Evolution of experimental Young's modulus of the MSp composites vs. spinel inclusion content and comparison with the lower bound of the Hashin & Shtrikman's model (Grasset-Bourdel, 2011)**

According to this model, a higher value of spinel inclusion content is supposed to increase Young's modulus of the composite. This is not in agreement with the obtained experimental data. Indeed, spinel addition induces a decrease of Young's modulus value. This difference is explained by the presence of a micro-cracking network in these thermally damaged materials.

In addition, Young's modulus evolution at high temperature was investigated using ultrasonic measurements. The studied materials exhibit an hysteretic cycle (Figure IV-3) which is characteristic of thermally damaged materials (Huger et al., 2007) with a micro-cracked microstructure: a high increase and decrease of Young's modulus during thermal cycle are mainly due to micro-cracks closure (heating) and opening (cooling) respectively. Besides, the maximum value of Young's modulus, reached during the beginning of cooling, is found around 950°C for all studied samples and the major decrease in Young's modulus occurs in the 950°C-600°C range. We can notice that the maximum value is not similar to the Hashin & Shtrikman's model, this means that there is not a complete closing of micro-cracks.

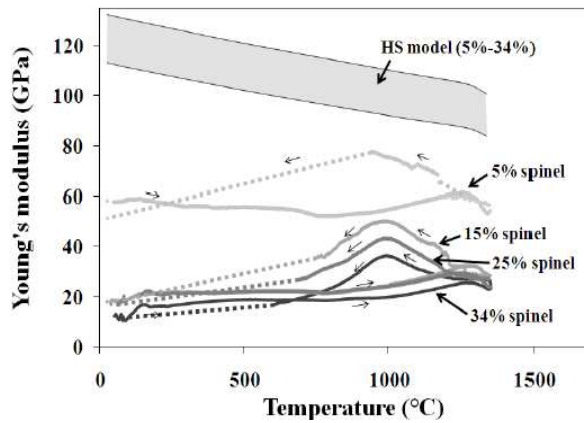


**Figure IV-3: Evolution of the Young's modulus vs. temperature of the MSp composites with a spinel grain size of 1-3 mm and different spinel inclusion contents (Grasset-Bourdel, 2011)**

Besides, the evolution of the thermal expansion coefficient vs. of the spinel inclusion content either at the beginning (1200-1000°C) and the end of cooling (400-200°C) was determined and represented in Figure IV-4. Thanks to these results, a huge part of micro-cracks present in the microstructure seems to be closed at the beginning of cooling. At lower temperature, stress relaxation, involved by micro-cracks opening during cooling leads to lower thermal expansion values than expected.

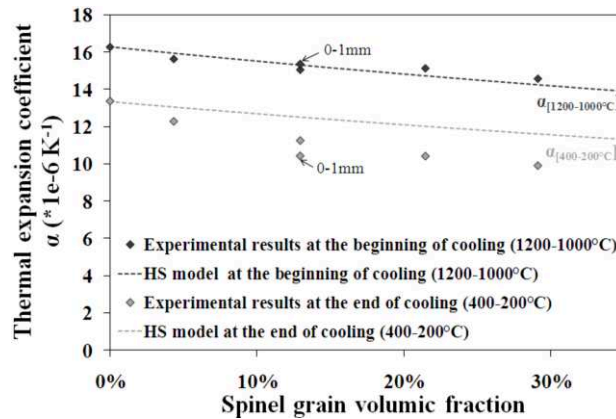


**Figure IV-4: Influence of spinel inclusion content on the thermal expansion coefficient of composites either at the beginning (1200-1000°C) and the end (400-200°C) of cooling (Grasset-Bourdel, 2011)**

The work initiated by Grasset-Bourdel has been continued in the present work, in order to study the influence of damage induced by spinel inclusions on the non-linear

mechanical behaviour and fracture mechanisms, two types of MSp materials with different spinel content (5 wt.% and 15 wt.%) has been tested by WST using DIC and compared to pure magnesia (MgO) material.

## II.2. Non-linear mechanical behaviour of magnesia spinel refractories

The WST test was conducted on two samples ( $100 \times 100 \times 100 \text{ mm}^3$ ) of each material type; the aim was here to analyse crack propagation in the different studied materials.

### II.2.1. Load-displacement curves obtained by WST

Figure IV-5 represents the typical horizontal load-displacement curves of pure MgO and MSp materials obtained by WST.

The mechanical behaviour of all these materials is characterized by three stages:

- The first stage corresponds to materials linear elastic behaviour.
- The beginning of non-linearity is related to the occurrence of micro-cracking network (stage 2).
- The maximum of the curve is linked to the macro-crack onset. The following part of the curve represents the crack propagation (stage 3).

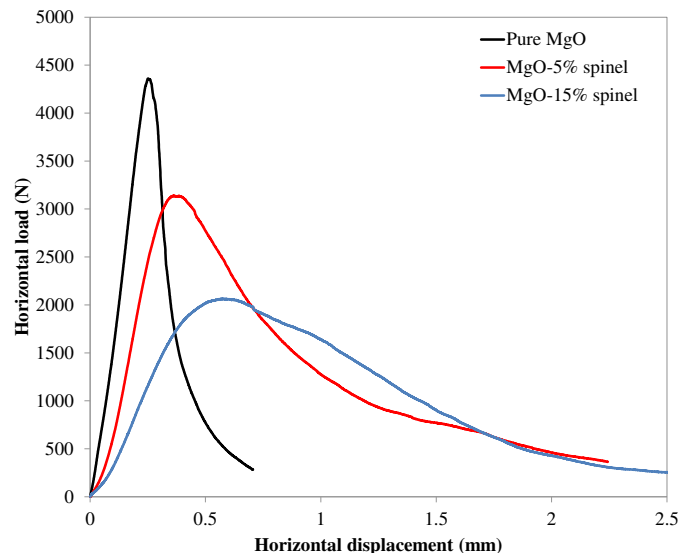


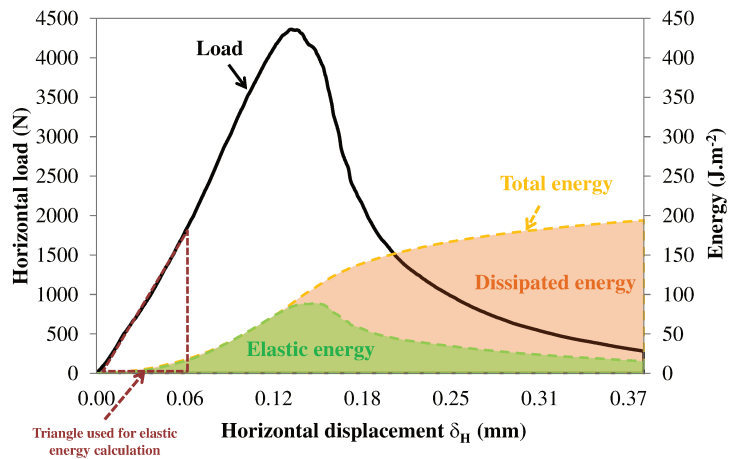
**Figure IV-5: Horizontal load-displacement curves of pure MgO and MSp materials obtained thanks to WST**

Horizontal load-displacement curves of pure MgO exhibits a much higher maximum load, a lower strain at the peak, and a reduced post-peak region.

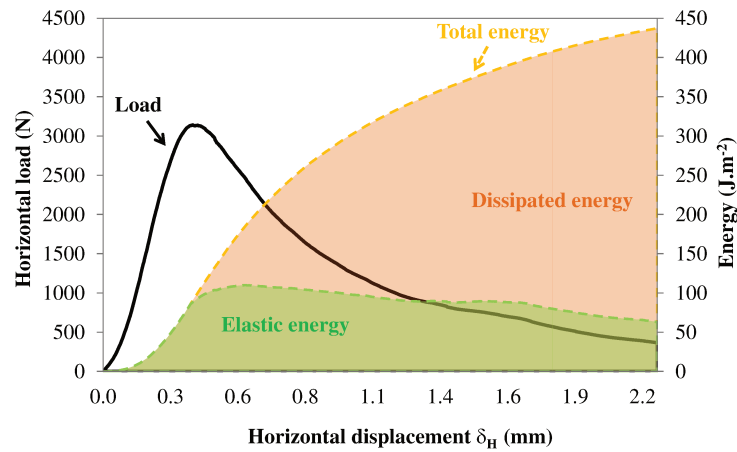
Curves of MSp present a much accentuated non-linear mechanical behaviour up to the peak with a significant post-peak region. The increase of spinel content seems mainly to lower the maximum load, to enhance the pre-peak non-linear stage and to intensify the post-peak region. As introduced previously, this is explained by the high level of micro-cracking in the case of MSp developed during cooling and toughening mechanisms occurring around the crack, especially in the following wake region, which increase the resistance to crack propagation (Chapter I).

### **II.2.2. Energy and fracture analysis**

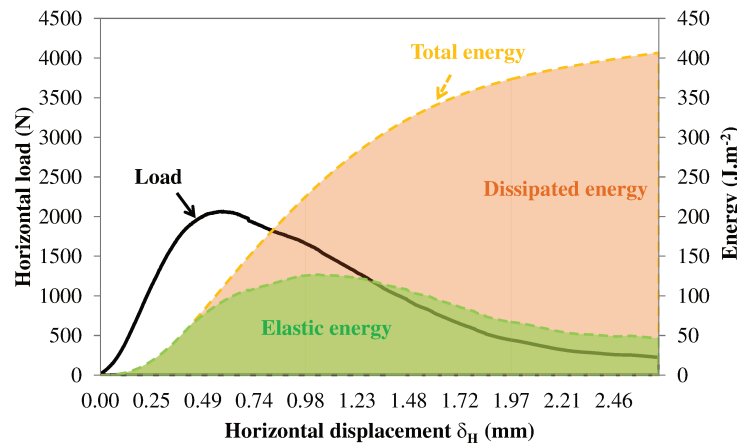
Elastic energy, dissipated energy and total energy are evaluated and their evolution is given in Figure IV-6. Total energy is deduced from the overall area under horizontal-displacement load curves obtained by WST divided by final crack surface. Elastic energy is estimated by considering a linear elastic behaviour which is related to the area of the triangle between the current point and the beginning of the curve. The dissipated energy corresponds to the difference between the two previous areas.



(a)



(b)



(c)

**Figure IV-6: Horizontal load-displacement and energetic curves for: (a) Pure MgO, (b) MSp-5% of spinel, (c) MSp-15% of spinel**

For the three materials, at the beginning, the total energy corresponds to the elastic one. In stage 2, a consumption of energy is effective thanks to the occurrence of the different mechanisms which happen in the following wake region. In the case of MSp, the dissipated energy required for material rupture is much higher than for the case of pure MgO.

Nominal notch tensile strength  $\sigma_{NT}$  and the surface fracture energy  $G_f$  were calculated respectively using Eq. II-14 and Eq. II-15.  $G_f$  values have been calculated from the area under the horizontal load-displacement curves for  $\delta_H$  values from zero up to the displacement corresponding to 15% of the maximum load which suppose a full crack opening.

These fracture parameters are reported in Table IV-1.

**Table IV-1: Fracture parameters of pure MgO and MSp obtained using WST**

		$\sigma_{NT}$ (MPa)	$G_f$ (N.m <sup>-1</sup> )	$G_f/\sigma_{NT}$ (mm)x10 <sup>-3</sup>
Pure MgO	Sample 1	14.35	231.00	16.13
	Sample 2	14.38	182.00	12.66
	<b>Average</b>	<b>14.36</b>	<b>206.50</b>	<b>14.39</b>
MSp (5% of spinel)	Sample 1	9.73	359.00	36.94
	Sample 2	10.19	423.00	41.51
	<b>Average</b>	<b>9.96</b>	<b>391.00</b>	<b>39.22</b>
MSp (15% of spinel)	Sample 1	6.55	326.00	49.86
	Sample 2	6.75	396.00	58.63
	<b>Average</b>	<b>6.65</b>	<b>361.00</b>	<b>54.25</b>

This table confirms that the nominal notch tensile strength decreases and the fracture resistance increases with the spinel rate.

The higher values of energy in the case of MSp are due to the dense network of micro-cracks created during the crack initiation and propagation.

The ratio  $G_f/\sigma_{NT}$  is a parameter that evaluates the brittleness of the studied material: the more brittle material is, the lower value of the ratio is.

### II.2.3. DIC as an efficient tool to bring out fracture mechanisms during WST

Crack growth in heterogeneous materials is often a very complex process, featuring many different physical mechanisms. To underline the presence of damage process of studied materials during fracture, DIC has been used in order to measure displacements and strains on sample surface during WST. To do so, sample surface has been prepared using black and white speckles; the acquired area and the ZOI are represented in Figure IV-7. The frequency of acquisition was 1 image/sec.

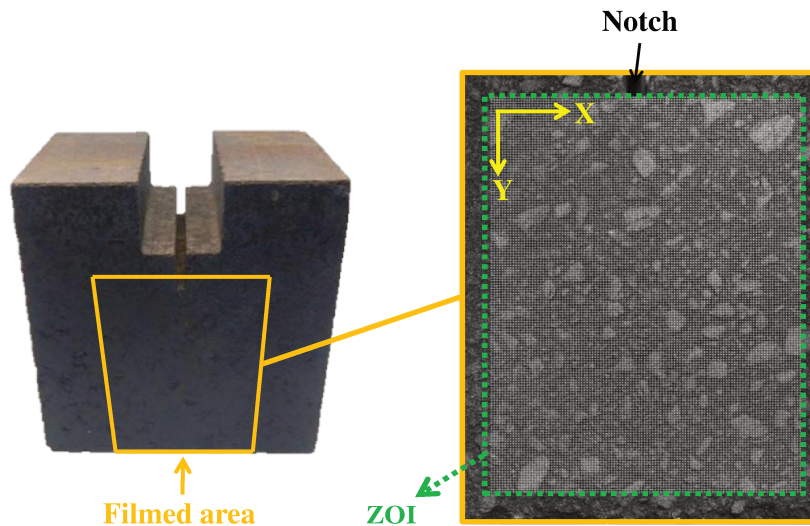


Figure IV-7: A recorded example image of a MSp material during WST

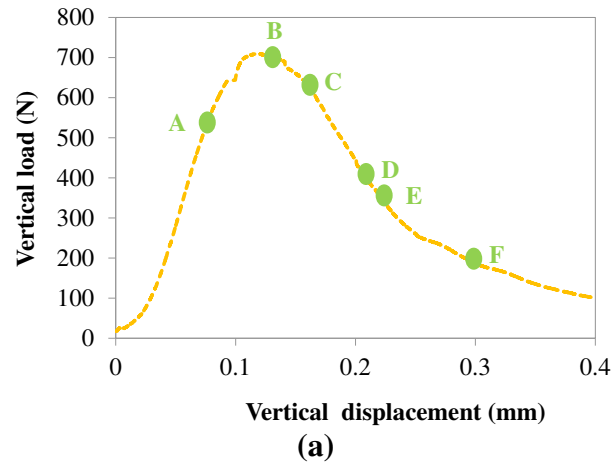
#### II.2.3.1. Displacement mapping

MSp-15% of spinel sample has been chosen here to illustrate displacement mapping during WST. DIC is performed with the assumption of a continuous material. Several maps of displacements along X and Y axis were obtained at the different steps (step A to F) shown on the curve (Figure IV-8a).

According to displacement fields, the macro-crack occurs at the maximum of the horizontal load in the area close to the notch due to local stress concentration (step B). As the



applied load is decreasing (step C), the crack propagates in a stable way until the total fracture of sample. It splits the sample in two parts as represented in displacement along X-axis in Figure IV-8b.



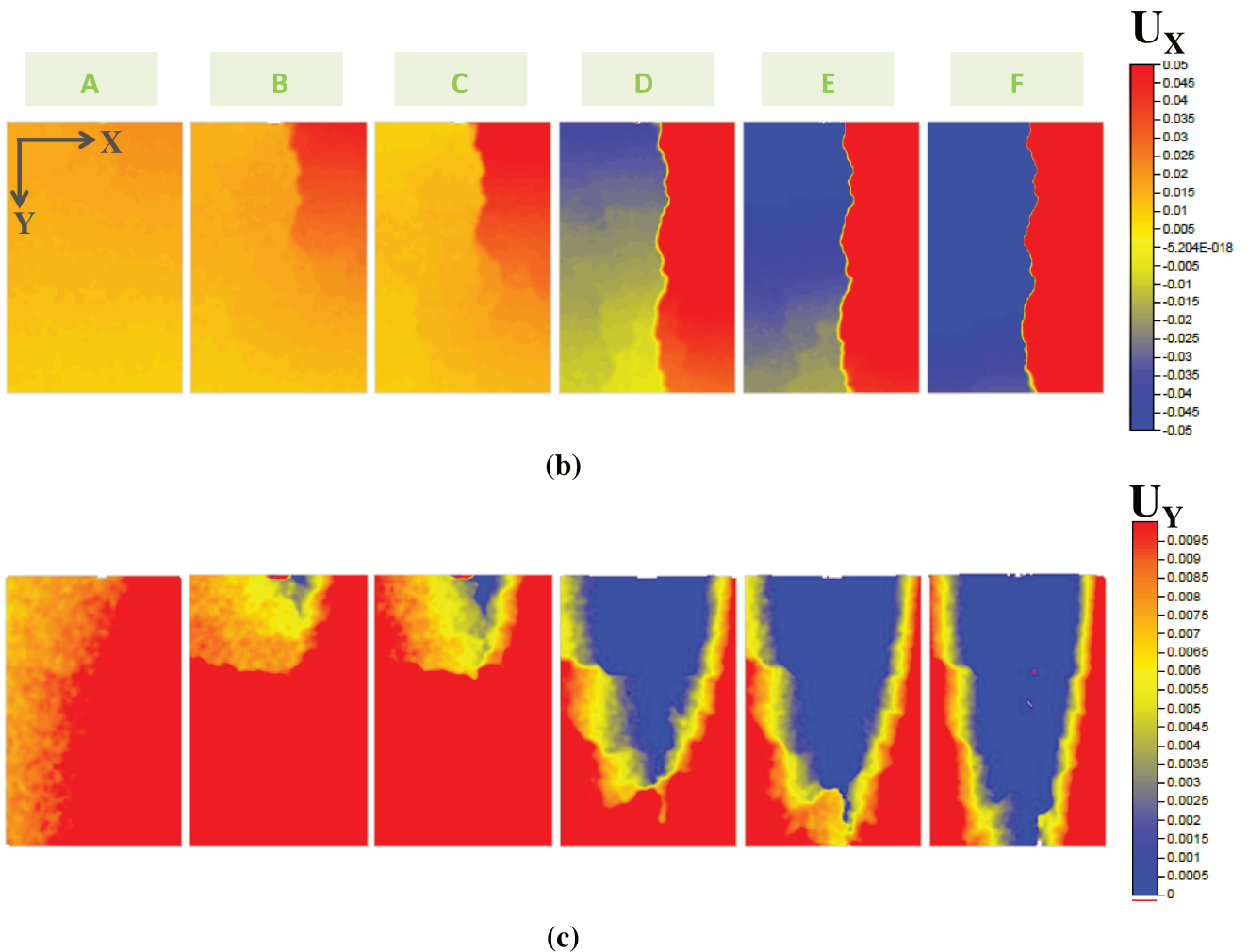


**Figure IV-8: An example of displacement maps along X-axis (b) and Y-axis (c) obtained during WST on a MgO-15% spinel sample at different times represented in the curve (a)**

From X-axis displacements, the right (or the left) part of sample has tendency to move to the right (or to the left) as the macro-crack is propagating (especially steps D-E-F). Besides, at the beginning of the test, according to displacement maps along Y-axis (Figure IV-8c), the whole sample moves slightly down (step A). However, after crack initiation and during its propagation, the area surrounding the notch is moving up (steps B to F). This behaviour is due to tensile damage in the vertical direction, with a lower magnitude than damage in the horizontal direction. This could be attributed to additional bending induced by WST. This zone becomes larger with the crack propagation and is symmetric relatively to the vertical central line of sample (steps D-E-F).

### II.2.3.2. Presence of crack branching phenomenon

Displacement field are useful for detecting cracks presence as it induces discontinuities (Grédiac et al., 2011). However, for the description of deformation behaviour, strain fields can be more relevant. From displacement maps, strain maps along X and Y axis ( $\epsilon_{XX}$  and  $\epsilon_{YY}$ ) have been thus calculated. Figure IV-9, Figure IV-10 and Figure IV-11 represent the evolution of strains along X and Y axis during WST respectively for pure MgO, MSp with 5% and 15% of spinel. The chosen steps are the same as the represented steps in Figure IV-8. The mechanical behaviour of the three samples chosen was given in Figure IV-6.

In the following results, crack presence and its opening correspond to the local highest strain values. Indeed, a specific strain colour scale has been chosen here. The choice of colours was done first in order to identify the evolution of the local highest strains (from grey to red) and to eliminate measurement disturbance (black colour). A presence of a crack corresponds to a strain threshold higher than 0.001 (grey colour) taking into account the accuracy of measurements.

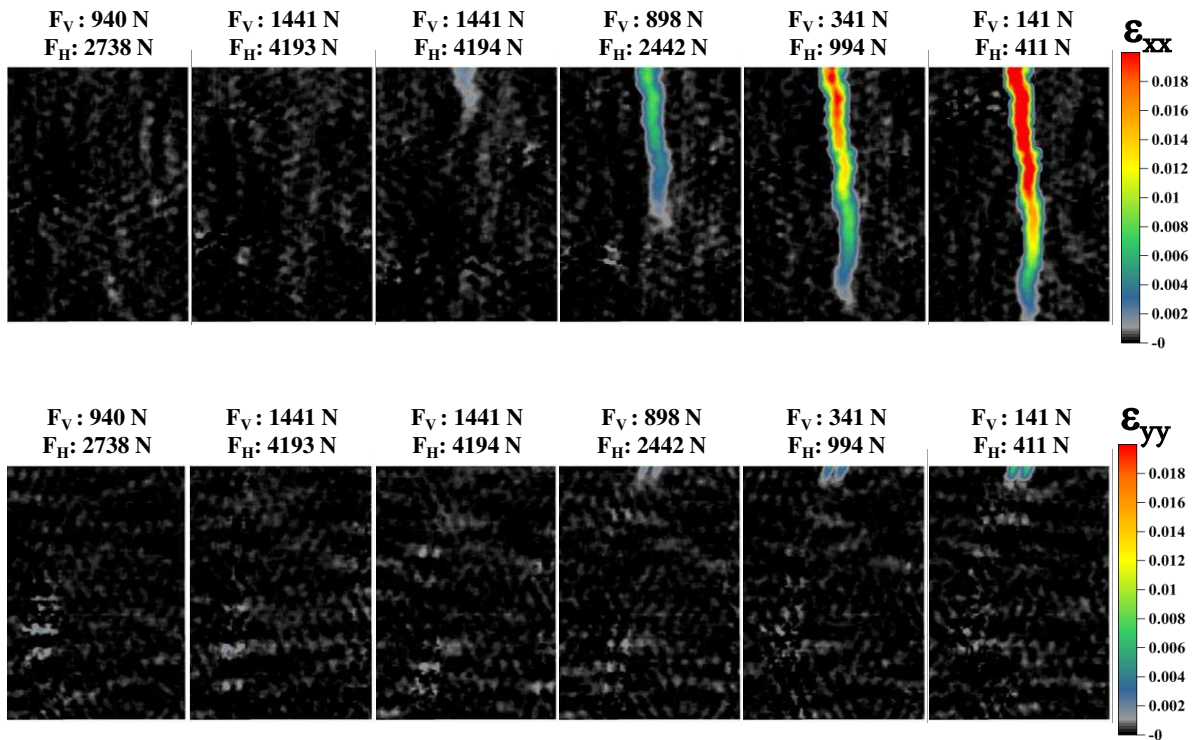


Figure IV-9: Maps of longitudinal strains along X and Y axis for pure MgO sample

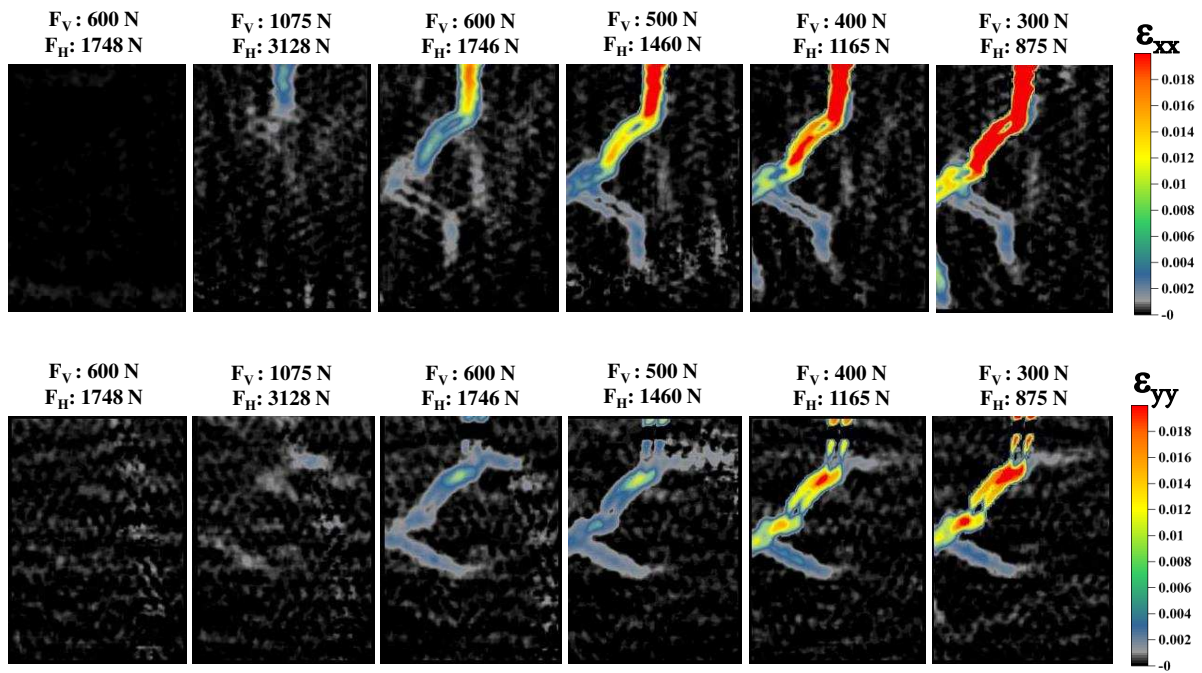


Figure IV-10: Maps of longitudinal strains along X and Y axis for MSp 5% of spinel

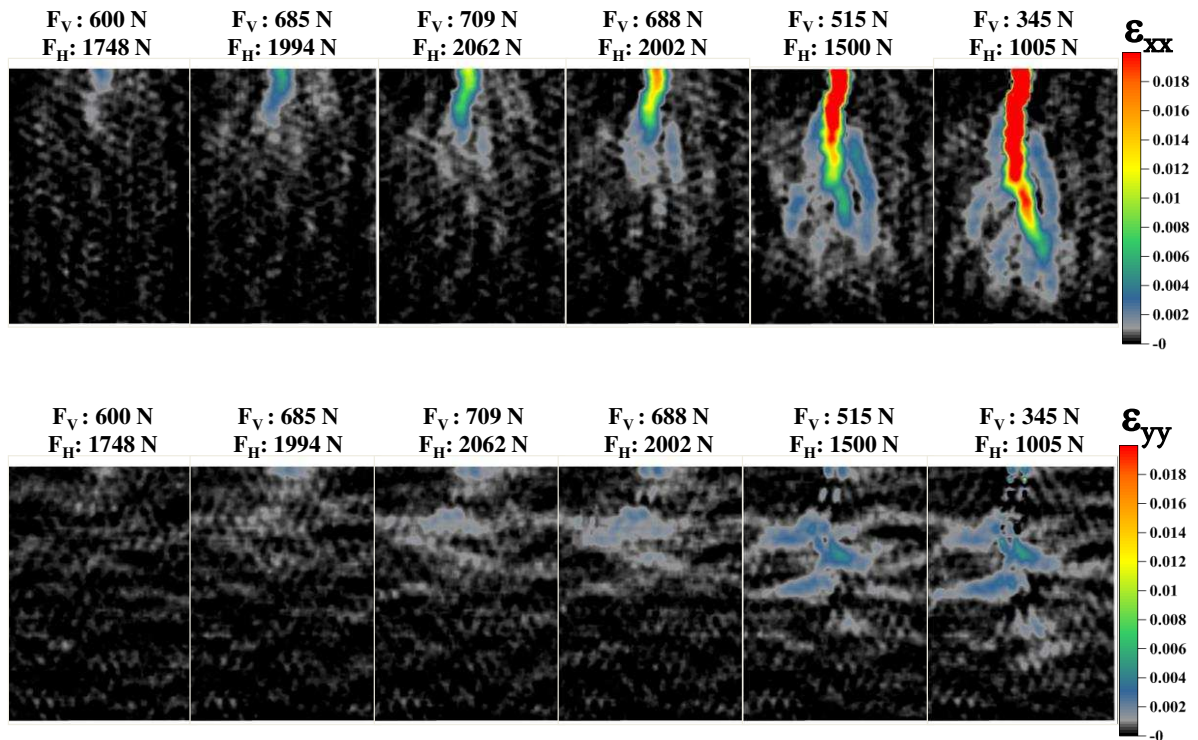


Figure IV-11: Maps of longitudinal strains along X and Y axis for MSp 15% of spinel

$\epsilon_{XX}$  strain maps describe crack opening and its propagation in mode I. In the case of pure MgO, there is only one crack that propagates in a vertical direction. However, the strain maps show that the crack in the case of MSp materials doesn't propagate only in a vertical direction and has a specific mode of propagation: bifurcation in the case of MSp with 5% of spinel and generation of crack branching phenomenon in the case of MSp with 15% of spinel.

In addition to  $\epsilon_{XX}$  strains,  $\epsilon_{YY}$  strains maps show a presence of tensile strains in the area near to the notch due to the vertical tensile stress from bending moment. Even if  $\epsilon_{YY}$  strains are in any case lower than  $\epsilon_{XX}$  strains, these strains are related to numerous mechanisms occurring in the crack propagation area (micro-cracks and crack bifurcation).

Then, using DIC, the presence of "crack branching" is clearly revealed in the case of MSp with 15% of spinel and results of many interacting micro-cracks or micro-branches (coalescence of micro-cracks). This confirms the complexity of crack growth process in heterogeneous materials due to the presence of several phases with different properties (thermal expansion coefficient and stiffness). Then, this can explain the high value of dissipated energy exhibited by MSp materials.

### **III. The non-linear behaviour of magnesia hercynite refractories**

Unlike to the simplified MSp materials presented previously and which were processed especially for the study, the following materials are industrial ones supplied also by RHI Company. These materials contain hercynite, which is, as mentioned in chapter II, another type of spinel.

#### **III.1. Microstructure characterization**

Three types of industrial materials were studied: magnesia spinel (MS), magnesia spinel type 1 (MST1) and magnesia spinel type 2 (MST2). As mentioned previously, these materials were not characterized before at SPCTS laboratory. For this reason, a classical package for characterization has been conducted. Table IV-2 presents density and porosity of these materials measured according to ASTM C830-00. Thanks to ultrasonic measurements



presented in chapter II, elastic properties have been determined at room temperature and are also given.

**Table IV-2: Properties of the studied MS materials (MS, MST1 and MST2)**

	MS	MST1	MST2
Density ( $\text{g.cm}^{-3}$ )	2.94 (+/-0.01)	2.98 (+/- 0.02)	3.01 (+/- 0.02)
Porosity (%)	16.07 (+/- 0.50)	15.75 (+/- 0.50)	15.11 (+/- 0.29)
Young's modulus E (GPa)	31.43 (+/- 3.43)	34.96 (+/- 3.59)	39.26 (+/- 3.56)
Shear modulus G (GPa)	13.48 (+/- 1.79)	15.00 (+/- 1.60)	16.89 (+/- 1.61)
Poisson ratio $\nu$	0.17 (+/- 0.03)	0.17 (+/- 0.04)	0.16 (+/- 0.02)

From these first experimental results, we can conclude that the MS, MST1 and MST2 contain probably around 10 – 15% of spinel ( $\text{MgAl}_2\text{O}_4$  or  $\text{FeAl}_2\text{O}_4$ ) taking into account the evolution of Young's modulus vs. spinel fraction presented in Table IV-2.

In order to identify the type of spinel which has been introduced in the three types of materials, some microstructure investigations have been conducted. Scanning electron microscope (SEM) with back-scattered electrons (BSE) has thus been applied to MS, MST1 and MST2 materials (Figure IV-12). It appears that MST1 and MST2 exhibit a much larger contrast from the aggregates. Thanks to Energy Dispersive Spectroscopy (EDS) technique, it was possible to identify the brightest aggregates as hercynite ( $\text{FeAl}_2\text{O}_4$ ). More details are given in Appendix A. In contrast to MST1 and MST2, the material MS with the less shiny aggregates correspond to  $\text{MgAl}_2\text{O}_4$  spinel without any  $\text{FeAl}_2\text{O}_4$ . Finally, MST2 contains only  $\text{FeAl}_2\text{O}_4$  inclusions, besides, MST1 reveals a mixture of  $\text{FeAl}_2\text{O}_4$  and  $\text{MgAl}_2\text{O}_4$ .

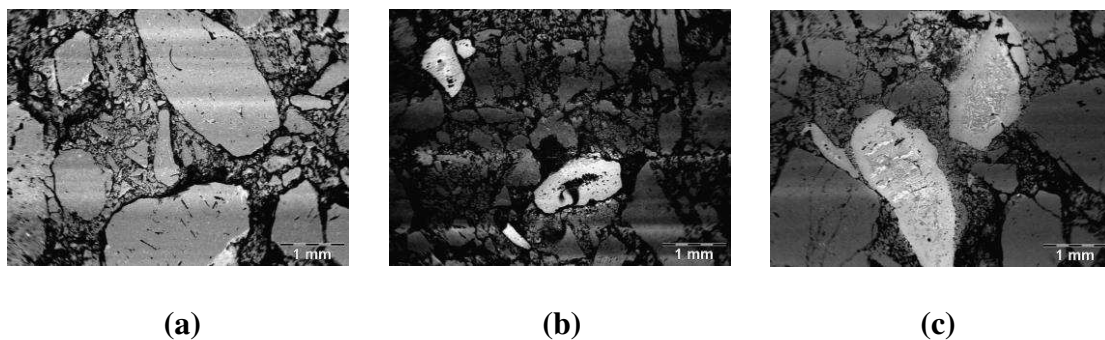


**Figure IV-12: Backscattered SEM analysis on (a) MS, (b) MST1 and (c) MST2**

Since the three materials MS, MST1 and MST2 don't contain the same kind of spinel exhibiting different expansion coefficient values, it is interesting to characterize the thermal expansion behaviour of these materials (Figure IV-13). The three curves are not linear, and the slopes at low and high temperature are quite different. As micro-cracking occurs during cooling, thermal expansion coefficients of these materials have been calculated during cooling between 1200°C and 1000°C and then between 400°C and 200°C. The values are represented in Table IV-3.

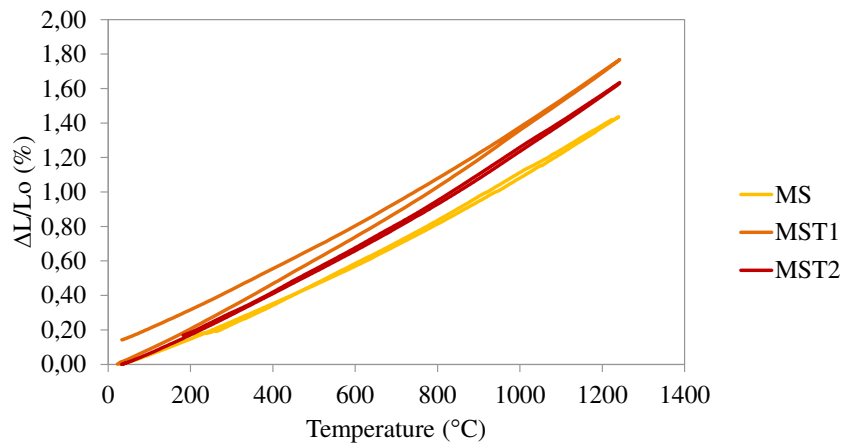


**Figure IV-13: Evolutions of thermal expansion of the: MS, MST1 and MST2 samples**

At high temperature (1200-1000 °C), it appears that in the case of MST1 and MST2, the thermal expansion is quite similar to magnesia sample whose expansion coefficient value is  $\alpha_{1200-1000^\circ\text{C}}=16.3 \times 10^{-6} \text{ }^\circ\text{C}^{-1}$  (Grasset-Bourdel, 2011). This demonstrates that for these two materials, there are probably rather no micro-cracks (micro-cracks are closed) in this temperature range. In comparison to MST1 and MST2, the thermal expansion of MS at high temperature is much lower. This can be explained by the difference between thermal expansion coefficient of  $\text{FeAl}_2\text{O}_4$  ( $\sim 10.3 \times 10^{-6} \text{ }^\circ\text{C}^{-1}$ ) and  $\text{MgAl}_2\text{O}_4$  ( $\sim 7.6 \times 10^{-6} \text{ }^\circ\text{C}^{-1}$ ). As a consequence, MS is the most micro-cracked since the thermal expansion mismatch  $\Delta\alpha$  between the present phases is higher than MST1 and MST2. This is confirmed by a much lower value of thermal expansion of MS in the low temperature range 400-200°C.

**Table IV-3: Thermal expansion coefficient values of MS, MST1 and MST2**

	MS	MST1	MST2
$\alpha_{1200-1000^{\circ}\text{C}} (^{\circ}\text{C})^{-1}$	$14.6 \times 10^{-6}$	$16.0 \times 10^{-6}$	$16.1 \times 10^{-6}$
$\alpha_{400-200^{\circ}\text{C}} (^{\circ}\text{C})^{-1}$	$10.3 \times 10^{-6}$	$11.9 \times 10^{-6}$	$11.9 \times 10^{-6}$

Taking into account these results and the ones presented in Table IV-2 in terms of micro-cracking density and Young's modulus, MST2 seems to be most probably the less flexible one, but however, hercynite can be preferred for its low cost in industrial applications.

### III.2. Mechanical behaviour using DIC at room temperature

It could be interesting now to understand the relationship between the stress-strain law and the microstructure, the main difference between materials being here the type of spinel inclusions inside magnesia matrix.

#### III.2.1. Four-points bending test

The stress-strain curves of MS, MST1 and MST2, obtained by four-points bending test on samples of 130 x 25 x 25 mm, are presented in Figure IV-14. Stress values were calculated using the Eq.II-6. The three materials exhibit a non-linear asymmetric mechanical behaviour. One can remind that Eq.II-6 gives valid results for symmetric behaviour. That is why, the stress values here obtained should be considered with caution.

Considering the three obtained curves of Figure IV-14, it confirms that MST2 is the less flexible material compared to MS and MST1. In fact, strain-to-rupture of MST2 is the lowest one. Strain-to-rupture of MS and MST1 are rather similar and larger. Considering stress analysis, MST2 exhibits a high stress-to-rupture which can be explained by its low porosity level.



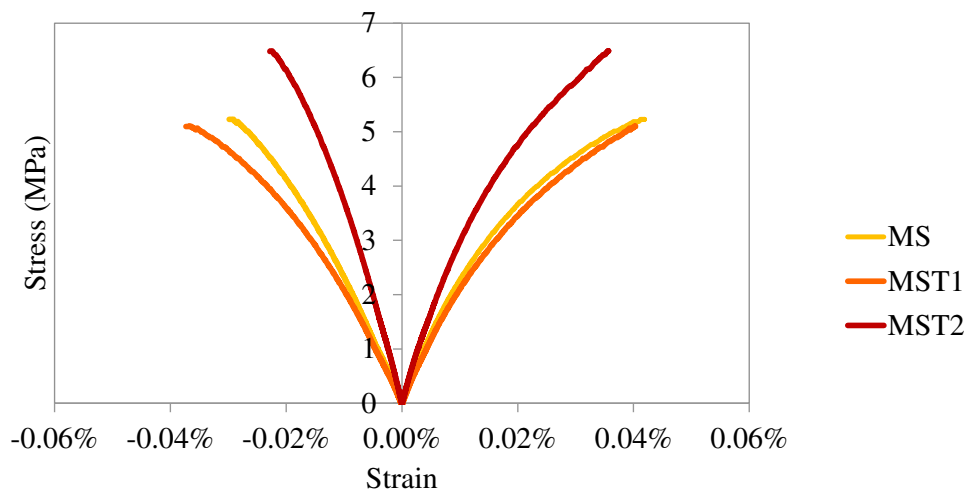


**Figure IV-14: Stress-strain curves of MS, MST1 and MST2 materials**

As MST2 materials exhibit the lowest strain-to-rupture compared to MS and MST1, and in the aim to improve the accuracy of DIC measurements, the following paragraphs will focus on MST2 in order to complete the development of this optical technique started using a very flexible material (AT VF presented in chapter III).

### **III.2.2. Brazilian test**

Brazilian test has been enforced for many years as an industrial easy test to obtain reliable values of tensile strength for refractories. The idea here is to combine this test with DIC to enrich the mechanical characterization. To do so, MST2 sample has been chosen.

#### **III.2.2.1. Load-displacement curves**

Figure IV-15 represents a typical load-displacement curve of MST2 characterized with a non-linear mechanical behaviour due to the microstructure as explained before. On this curve, different steps are defined in order to analyse the material behaviour during the test.

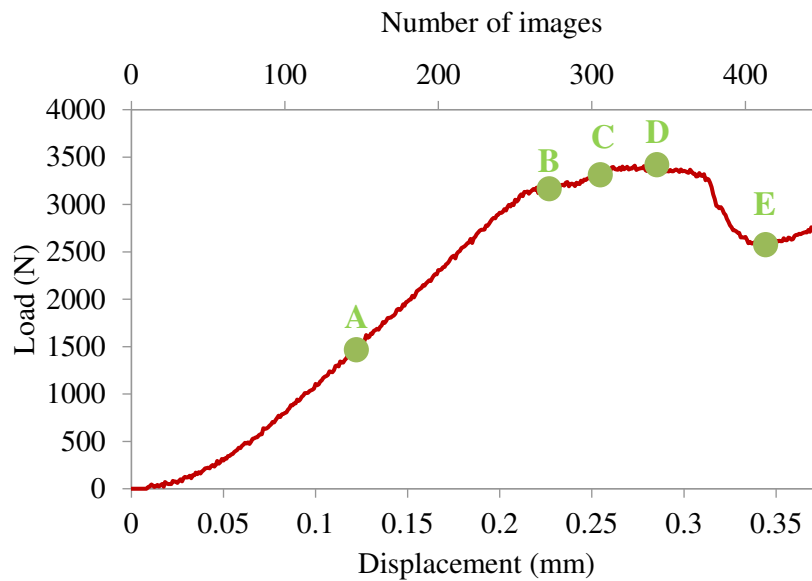


**Figure IV-15: Load-displacement curve of MST2. The points A, B, C, D, E correspond to the steps analyzed using DIC**

As detailed in chapter II, the tensile strength deduced from the Eq. II-8 used at the maximum load, has been estimated for MST2 and corresponds to  $\sigma_t = 3.98$  MPa.

### III.2.2.2. Stress-strain curve deduced from DIC

In order to obtain strain-stress curve using DIC, a choice of small size correlation windows has been done in purpose located in the central part of the sample since the stress state in this area can be assume rather homogeneous (see following paragraph III.2.2.4). These correlation windows have been localized symmetrically from the vertical axis of the sample. In such condition, we can assume that the strain is uniform in this overall central part. The X-axis strain obtained in such manner during the complete test allows then to obtain the stress-strain curve for MST2 illustrated in Figure IV-16.

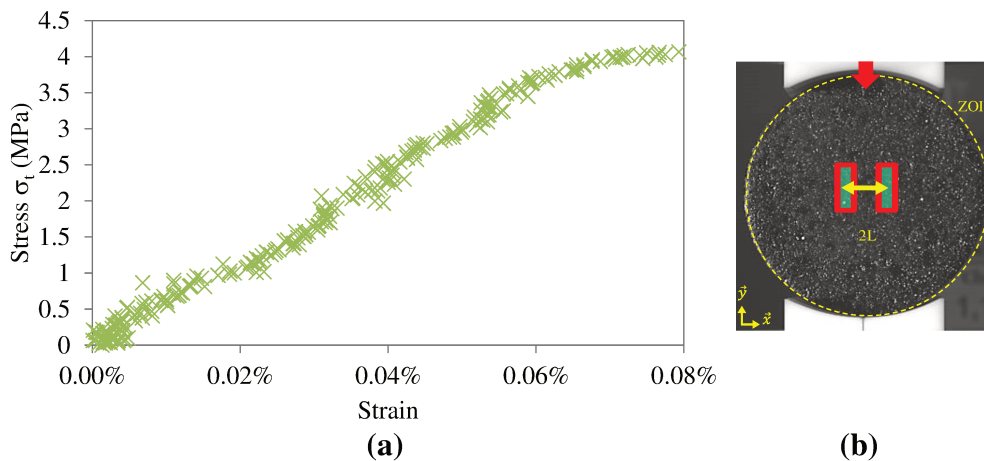


**Figure IV-16: (a) Stress-strain curve obtained from DIC results obtained using Brazilian test (b)**

The optimization of experimental conditions (§IV.1.4 in chapter II) leads to improve the accuracy of measurements ( $\Delta l/l \sim 10^{-5}$ ). The obtained results show a rather linear behaviour at the beginning of loading. Then, a non-linearity appears around an applied stress of 3 MPa, which leads to a tensile strength of 3.98 MPa. These results are in agreement with those obtained using four-point bending test and already presented before.

Considering the linear part, as seen in chapter II, elastic properties of a material can be calculated taking into account the biaxial loading in the central part of the sample. According to the Eq. II-10 and the Eq. II-11,  $E_s$  and A have been evaluated. The factor A was determined taking into account the distance between the two windows of correlation 2L in order to be coherent with gages length using the formula of the Eq. II-11. From these values and using the Eq. II-9, Young's modulus has been determined, and the measured value was  $E_t=39.6$  GPa which is quite similar to the value obtained by ultrasonic measurements (Table IV-2).

### III.2.2.3. Fracture analysis thanks to DIC

Aiming to analyze the fracture propagation within the sample, the correlation windows have been chosen here rather small ( $8 \times 8$  pixels<sup>2</sup> to promote high spatial resolution) even if the strain accuracy becomes lower. To do so, the computation was done using similar parameters as those used in chapter III: § III.3. Figure IV-17 and Figure IV-18 show the obtained result of fracture propagation according to the steps (A, B, C, D and E) already defined

in

Figure IV-15. The choice of colors was first elaborated in order to identify the evolution of the local highest strains and to eliminate measurement disturbance (black colour).

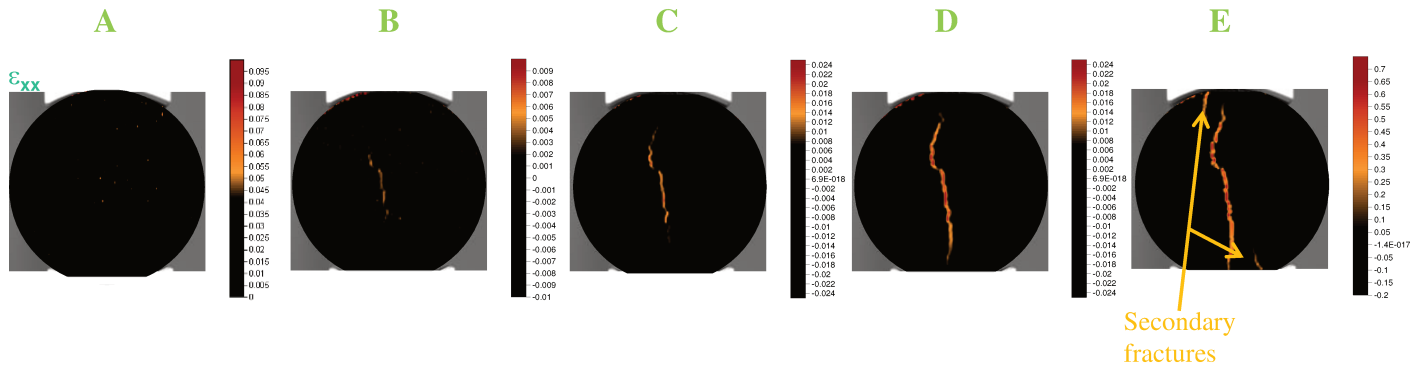


**Figure IV-17: Maps of strains along X-axis for the five steps defined in Figure IV-15**

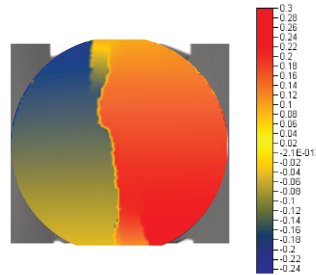


**Figure IV-18: Map of displacements along X-axis for the final step (E)**

Results obtained thanks to DIC confirm that the crack starts (Figure IV-17B) from the sample centre and fracture surface is parallel to the compressive vertical loading direction. This is due to the presence of maximum tensile stresses in this area which are normal to the loaded diameter. Then, this crack propagates symmetrically from the centre as the applied load increases (Figure IV-17C) until failure occurs at the maximum load (Figure IV-17D). At this point, sample becomes rather divided into two halves (Figure IV-17E). For this very last step, displacement map is represented in Figure IV-18.

In addition to the main crack, other damage (secondary fracture) appears at the end of the test (Figure IV-17E) due to the fact that each half sample is then individually being constrained by the testing curved bearing blocks. This corresponds to the beginning of the stage 4 (usually not exploited) already explained in chapter II and shown in Figure II-6.

This sequence of result proves that DIC can be a powerful method to analyse damage process: crack initiation and its propagation up to the final rupture.

### III.2.2.4. Numerical simulation

So as to clarify the distribution of stress during a Brazilian test and to explain the reason for which the crack appears in the central part of sample, a simulation using FEM by Code Aster software has been done (Figure IV-19) assuming an elastic behaviour of the material.

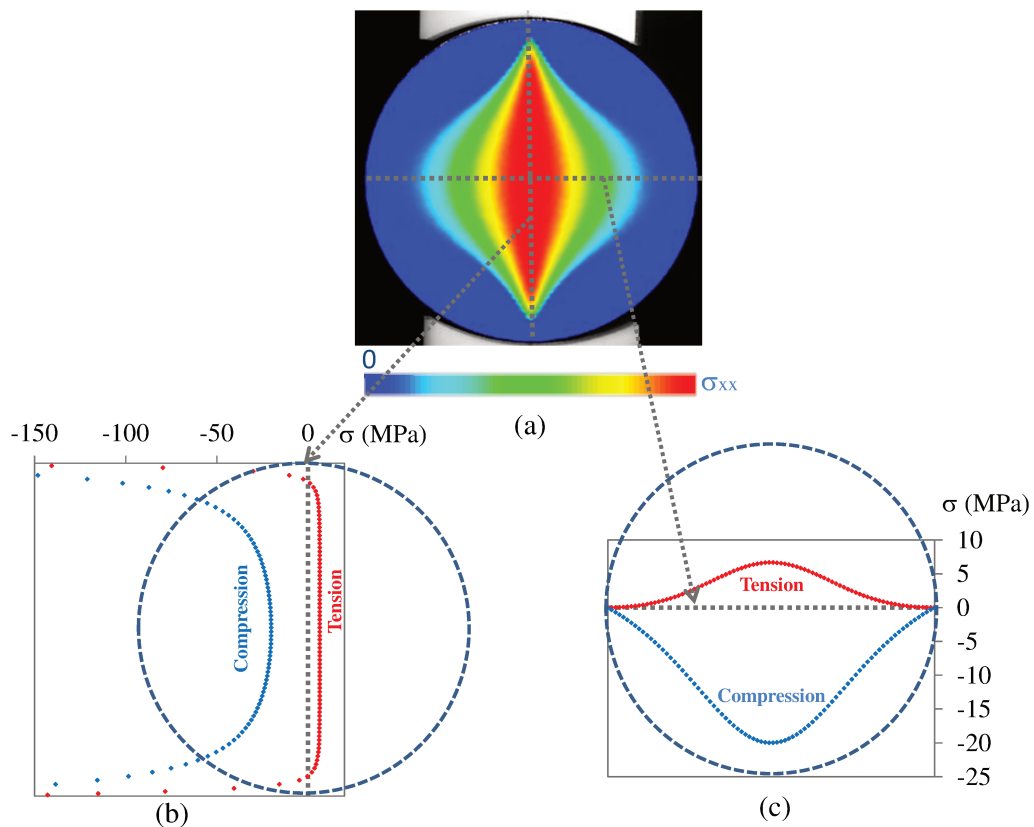


**Figure IV-19: Stress distribution in a sample during a Brazilian test: (a)  $\sigma_{xx}$  stress map, (b) Stress distribution along the diametrical vertical line, (c) Stress distribution along the diametrical horizontal line**

Even if the finite element calculation was performed here assuming a linear elastic behaviour, results clearly illustrate the combination of tensile  $\sigma_t$  and compressive  $\sigma_c$  stresses which strongly vary within the sample from the central part to the edge (especially along the

diametrical horizontal line). Along diametrical vertical line, tensile stress is quasi-uniform, this is a key point for a Brazilian test from which we can evaluate the tensile strength.

It can be noticed that tensile stresses are lower than compressive ones; however, tensile ones are those which induce the material ruin. Indeed, for brittle materials, tensile strength is around 10 times weaker than compressive one.

In one hand FEM analyses give us an idea about theoretical stress distribution on sample surface during Brazilian test, and in the other hand; DIC is useful to obtain strain fields in the central part during the test. To do so, strain calculations have been computed between many correlation windows localized in the zone represented in Figure IV-20a. This specific area was chosen taking into account stress distribution obtained by FEM analysis (Figure IV-19). Thus, a map of strain evolution in the vertical diametrical line vs. time is represented in Figure IV-20b.

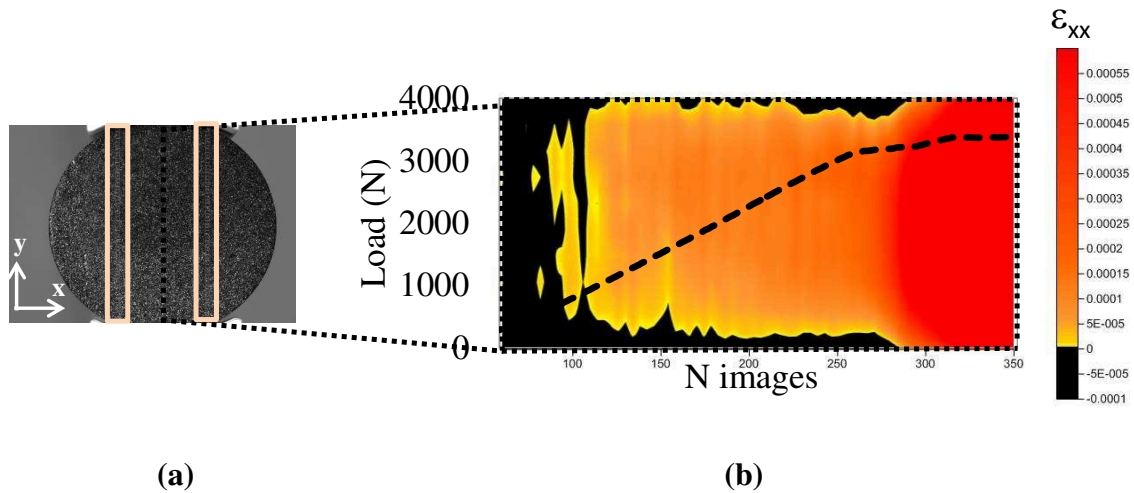


**Figure IV-20: Evolution of  $\epsilon_{xx}$  strains along vertical Y-axis: (a) localization of the correlation windows for computation, (b) orange colour indicates the  $\epsilon_{xx}$  horizontal tensile strain level (dashed point line correspond to vertical applied load)**

At the beginning of the test, the load level is quite low, and then the strain measurements are noisy. As the applied load is increasing, tensile strain becomes higher (orange colour) and its profile is quite in agreement with FEM calculation. Around image 250, initial crack occurs till the final rupture of the sample around image 280. In this stage,

tensile strain profile evolves since the central initial crack develops up to the boarder of the sample.

### III.2.2.5. Energetic approach

As DIC contributes to determine crack initiation and its propagation, the idea here is to combine crack extension which can be obtained by DIC with dissipated energy which can be calculated from the load-displacement curve at each stage (principle explained in Figure II-6). In order to increase the number of images acquired during the very short rupture sequence, a rate of 50 images per second was chosen for acquisition during the overall test. In order to eliminate DIC noise and to estimate accurately crack length at each stage, a specific scale colour threshold has been set.

This approach has been applied for the stages 2 and 3 defined in Figure II-6, that means starting at the end of linear part of the loading curve up to the minimum load observed just after the final rupture. At the beginning of stage 2, even if the loading curve is no longer linear, no significant cracks can be observed using DIC. As matter of fact, the first significant cracks can only be detected for the image 17700 (Figure IV-21a). Thus, using this approach, crack length has been evaluated from image 17700 to image 20800 (final rupture) represented in Figure IV-21a, and its evolution is plotted in Figure IV-21b. A numerical fitting has been applied in order to remove experimental measurement disturbance.

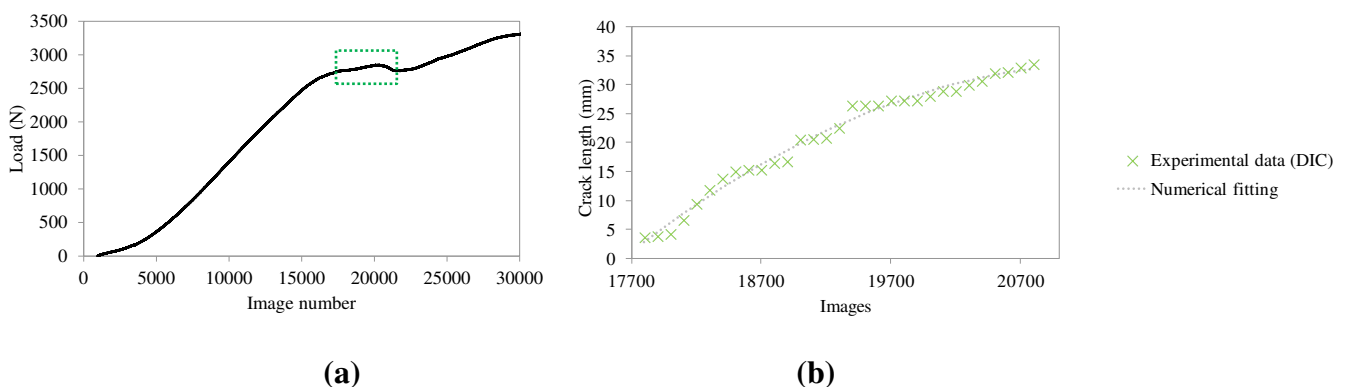


**Figure IV-21: Attempt of crack length measurement using DIC data: (a) selection of the images corresponding to the rupture sequence indicated by the green dashed window, (b) obtained crack length for these images.**

By associating crack length evolution and dissipated energy calculated for each single image using the load-displacement curve, an estimation of energy evolution vs. crack length has been determined and is represented in Figure IV-22.

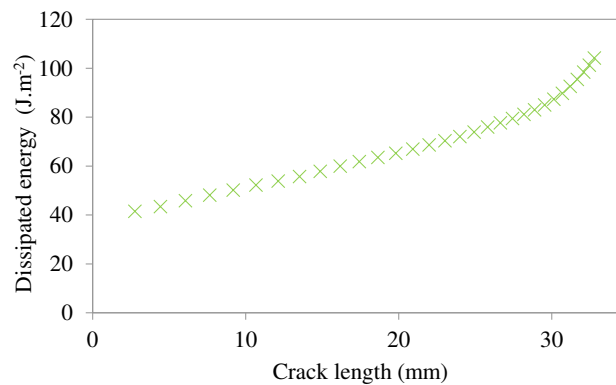


**Figure IV-22: Representation of dissipated energy vs. crack length for MST2 material during Brazilian test**

Even if Brazilian test is not devoted to such purpose due to the thickness of tested samples is not large enough, the obtained results are however interesting. Indeed, the increasing shape of this curve corresponds to R-curves already detailed in chapter I.

### **III.2.3. Wedge Splitting test**

As already managed for magnesia spinel materials (§ II.2.2), the aim is here to analyse crack propagation in MST2 material using classical WST combined with DIC.

#### **III.2.3.1. Load displacement curves**

The horizontal load-displacement curve for MST2 material obtained by WST is represented in Figure IV-23. The dimensions of sample are 100 x 100 x 70 mm since the thickness of delivered bricks was only 70 mm. As expected and like MSp materials, the mechanical behaviour of MST2 is non-linear before rupture and characterized with an interesting post-peak region. It confirms that the addition of hercynite enhances the non-linearity of magnesia materials, decreasing maximum load to rupture, increasing strain-to-rupture and improving the post peak region in comparison with pure MgO. This post peak



region is mainly induced by mechanisms of fracture occurring around the crack tip, especially in the following wake region, which contributes to increase the resistance to crack propagation.

As already discussed, since the thermal expansion mismatch between magnesia and hercynite is lower than the one between magnesia and spinel, it makes sense that fracture energy in the case of MST2 is lower than fracture energy of MSp.

Thanks to strain maps obtained by DIC, the crack onset occurs in the zone close to the notch. As the applied load is increasing, the crack is divided into two branches which demonstrate crack branching phenomenon already noticed in the case of MSp materials.

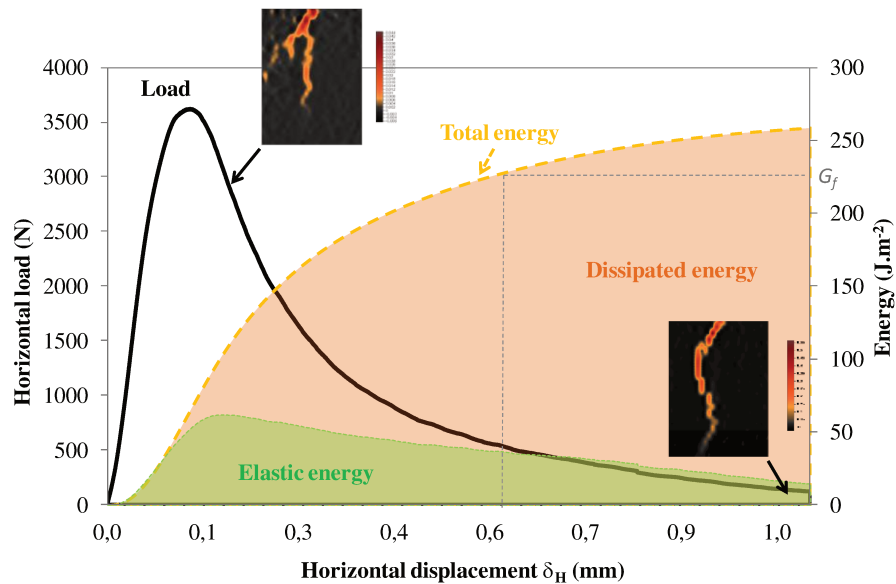
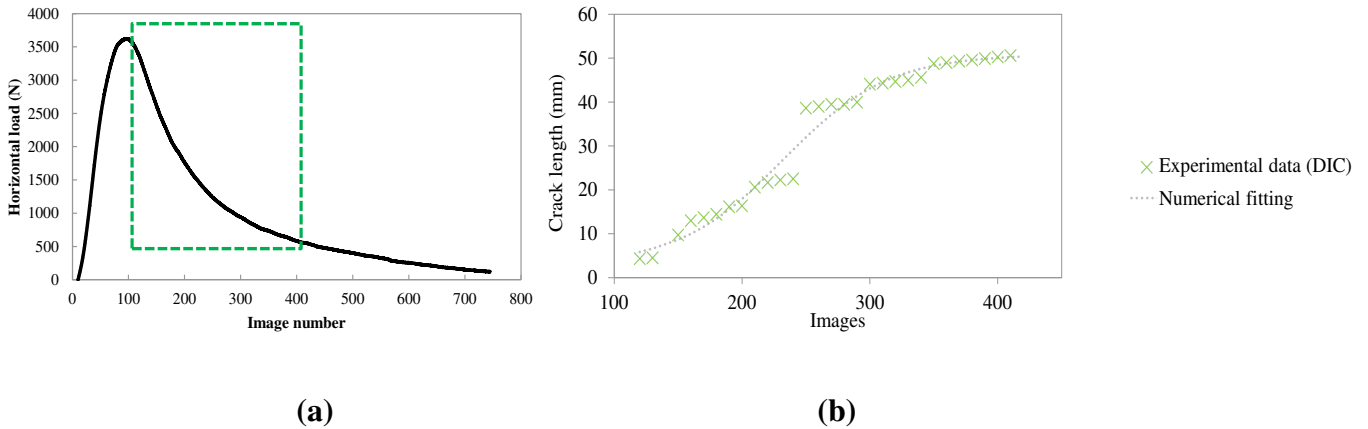


Figure IV-23: Horizontal load-displacement, energetic curves of MST2 and crack branching evidence observed by DIC

### III.2.3.2. Energetic approach

As already managed for Brazilian test, the idea here is also to combine crack extension which can be obtained by DIC with dissipated energy estimated from the load-displacement curve at each single stage.

The first significant cracks detected are those determined for the image 120 (Figure IV-24a). Thus, using this approach, crack length has been evaluated from image 120 to image 410 (corresponding to 15% of  $F_{H,max}$ ). These images are represented in Figure IV-24a, and crack length evolution is plotted in Figure IV-24b. A numerical fitting has been applied in order to remove experimental measurement disturbance.



**Figure IV-24: Attempt of crack length measurement using DIC data: (a) selection of the images corresponding to the crack propagation indicated by the green dashed window, (b) estimated crack length for the selected images.**

The dissipated energy, which corresponds to the difference between total and elastic energies, has been calculated at different steps until  $\delta_H$  corresponding to 15% of  $F_{H,max}$ . For each analyzed image, the dissipated energy has been coupled to the estimated values of crack length and represented in Figure IV-25.

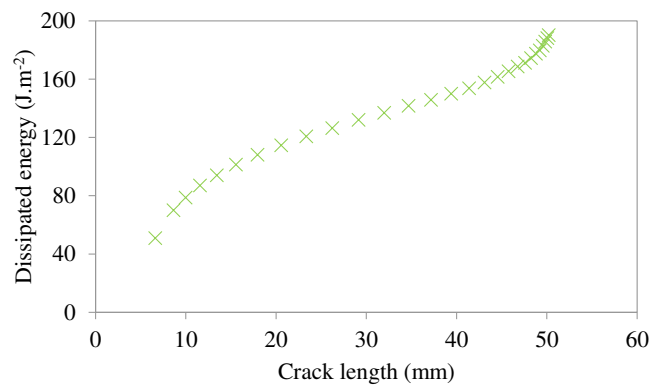


**Figure IV-25: Representation of dissipated energy vs. crack length of MST2 during Wedge Splitting test**

The rising behaviour of the curve confirms that, as the crack is propagating, the process requires more and more energy to pursue its progression. The increasing of dissipated energy value is related to the difficulty of the crack to extend. This is due to the occurrence of new mechanisms mainly located in the following wake region. Since these mechanisms were not activated at crack initiation, thus, the lower value of dissipated energy is observed at the beginning. These mechanisms make the refractory tougher before its failure and generate a non-linear mechanical behaviour associated to an increase of thermal shock resistance.

## IV. Conclusion

Thanks to the knowledge acquired during the first experiments on a model single phase flexible material (AT VF) which was the main aim of the previous chapter, the current chapter was dedicated to apply these DIC skills on industrial heterogeneous materials exhibiting a high heterogeneity and which are characterized with much lower strain-to-rupture level in comparison with AT VF.

As strain level for these industrial materials was expected to be much lower, it was necessary to improve the accuracy of DIC technique so as to enlarge its application on different classical mechanical tests often applied to characterize refractories. Indeed, in addition to four-point bending test, DIC has been coupled to Brazilian and Wedge Splitting tests.

During Brazilian test, tensile stresses are acting horizontally in the central part of the sample until failure happens and this has been clearly visualized thanks to strain map experimentally obtained by DIC. In fact using different strain maps, the vertical crack appears in the central part of the sample, and as the applied load is increasing, this crack propagates in either sides from the center of sample until the final failure. From the evolution of strain fields during the test, the crack's length has been determined at each single stage and coupled to energetic calculation. Thus, even if Brazilian test is not dedicated for such purpose, it has been possible to illustrate a R-curve behaviour.

Besides, Wedge Splitting test combined to DIC allows studying the mechanisms of micro-cracking and its influence on the non-linearity of mechanical behaviour of these

materials. Indeed, the thermal expansion mismatch between the different phases (magnesia, spinel and hercynite) in studied industrial materials induces a large network of micro-cracks which lead to crack branching occurrence during Wedge Splitting test. This phenomenon is clearly visualized thanks to DIC. Similarly to Brazilian test, DIC allows the possibility to investigate crack length evolution and to combine it to dissipated energy in the aim to represent the R-curves.

# Chapter V

Finite element method updating: an approach to  
identify material properties

## I. Introduction

From displacement maps obtained using DIC, it is possible to determine mechanical properties of materials. This can be reached by coupling these displacements with finite element method (FEM) in the framework of FEMU-U already introduced in chapter I.

To achieve this goal and due to the lack of knowledge and expertise on this specific numerical topic in the SPCTS laboratory, a specific numerical development has been carried out. Even if the aim is to apply this technique on refractories exhibiting non-linear mechanical behaviour, the first step of this chapter is to implement this approach using simple configuration with a material whose mechanical behaviour is well-known. The study is carried out thanks to four-points bending test which has been privileged as it permits obtaining higher values of displacements on material surface in comparison with Brazilian test.

Here, the first chosen material is aluminium which exhibits a linear elastic mechanical behaviour with Young's modulus in the same range than many refractory materials. Then, the developed approach was applied on AT VF flexible refractory sample, already introduced in chapters II and III.

## II. Global approach of FEMU-U

FEMU-U is one among the updating methods of identification. It consists in performing iteratively FEM calculation in order to minimize the difference between experimental and simulation data using an objective function. This latter determines the convergence satisfaction criterion. In our case, the compared results are experimental and simulation displacements respectively noted ( $U_{EXP}$ ) and ( $U_{FEM}$ ).  $U_{EXP}$  corresponds to those obtained by DIC. The very first FEM calculation is computed thanks to an initial parameter set  $P_i$  (to be chosen by the operator) and then, taking into account the value of the objective function, new parameter set  $P_{i+1}$  is determined for the following calculation up to the satisfaction of the convergence criterion. This overall process is resumed in Figure V-1.

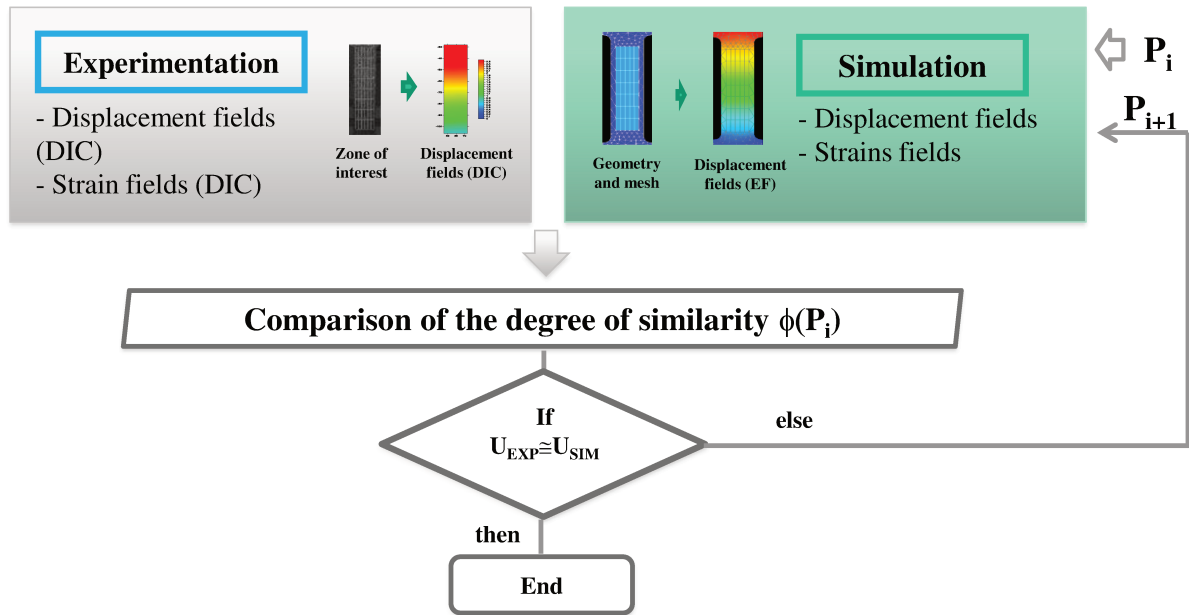


Figure V-1: Description of the global approach applied for implementation of FEMU-U

### III. Numerical implementation

#### III.1. Selection of numerical tools

The Code Aster software package has been used. It is developed by the EDF Company. It is an Open Source software package used by engineers, experts and researchers in civil and structural engineering. The main interest of using Code Aster is the huge number of available libraries, wide variety of models with many examples, the constant development and updating of new functionalities, and its compatibility with Python programming language.

Python programming language has been used to develop the global FEMU-U script so as to compute automatically the overall calculations. The different steps of this specific code will be detailed in the following paragraphs.

#### III.2. From experimental geometry to FEM simulation

From digital images obtained by DIC during the four-points bending test, a modelled sample in Code Aster has been created in order to be geometrically similar to the experimental one taking into account firstly, the pixel position of DIC pictures (ZOI),

secondly, the overall geometry of the sample and finally, the position of rolls contact used to apply the load (Figure V-2).

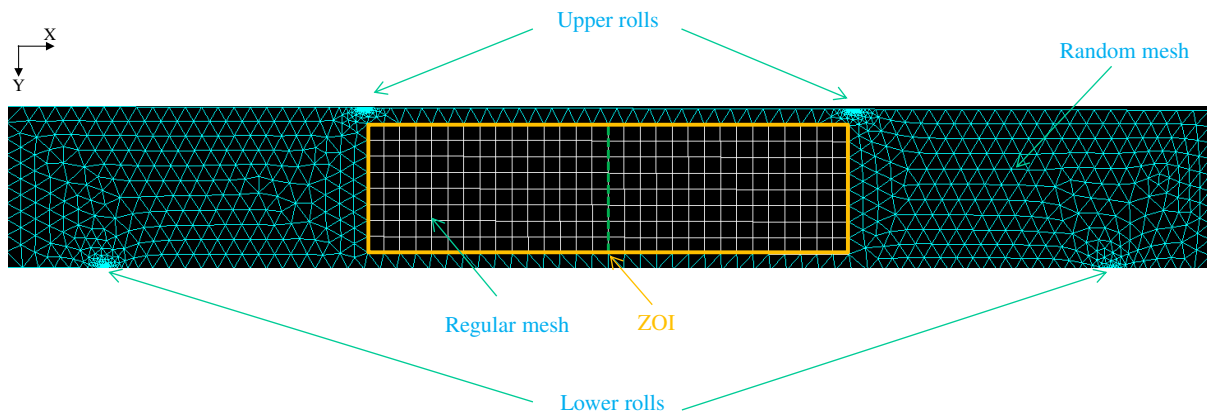


**Figure V-2: Geometry and meshing of the simulated sample under four-points bending test**

From DIC calculation, which generates displacements in the centre of each correlation window, an extraction of these data is conducted using Python script. At this stage, a particular attention has been paid in order to extract the coordinates of those experimental DIC calculation points to build the corresponding meshing grid which will be considered in Code Aster for simulation (ZOI in Figure V-2). Indeed, every single mesh nodes in ZOI should correspond accurately to the centre of each DIC correlation windows. This means that the distance between two nodes might correspond to the correlation windows size.

Out of the ZOI, the meshing becomes random and the area close to rolls contact is finely sub-meshed in order to avoid mesh abnormal distortions.

The imposed boundary conditions for simulation were chosen in order to be in accordance with the experimental ones for a four-points bending test: the nodes corresponding to the lower roll contacts are blocked along Y-axis (Figure V-2). Then, a vertical load, corresponding to the experimental one, is applied on nodes related to the upper roll contacts.

Using these boundary conditions and a given applied load, simulated strain maps can be obtained along X and Y axis (as represented in Figure V-3). The aim of this classical simulation configuration is to confront DIC and simulation as will be detailed in the following



paragraphs. As expected, between the upper rolls, the area will be under horizontal compressive stresses unlike the lower one which is submitted to tensile horizontal stresses.

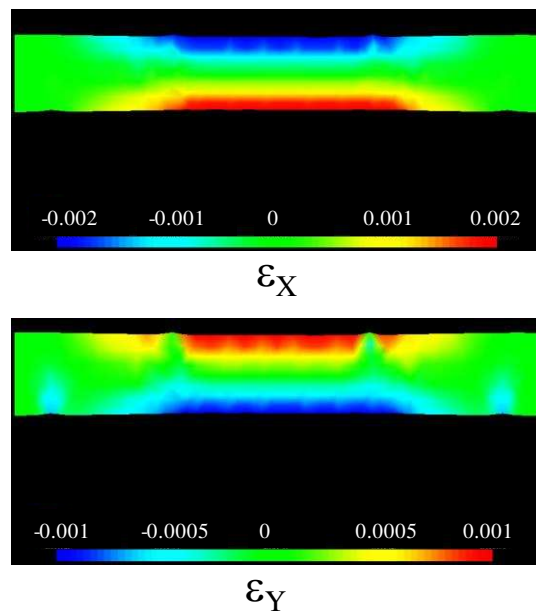


**Figure V-3: An example of strain fields which can be obtained by FEM simulation for a linear elastic material during four-points bending test**

### III.3. Pertinence of DIC results using control cards

From experimental data, during DIC calculation, some points may be outliers. In such case, these unreliable data may cause significant troubles for the comparison of displacements between FEM and DIC. For this reason, control cards have been used in order to eliminate these outliers points. To do so, three parameters have been defined to control DIC displacement values as represented in Figure V-4:

- **The target** corresponds to the arithmetic average of the points.
- **Controlling limits (horizontal red lines)** determine the interval where the measurements vary in a confidence level of 99,8% from the average. Then, an Inferior Controlling Limit (ICL) and a Superior Controlling Limit (SCL) are defined.

Using these limits, all points localized out of the ICL-SCL interval are automatically busted (red dots in Figure V-4) and then not taken into account for the FEMU-U calculation.

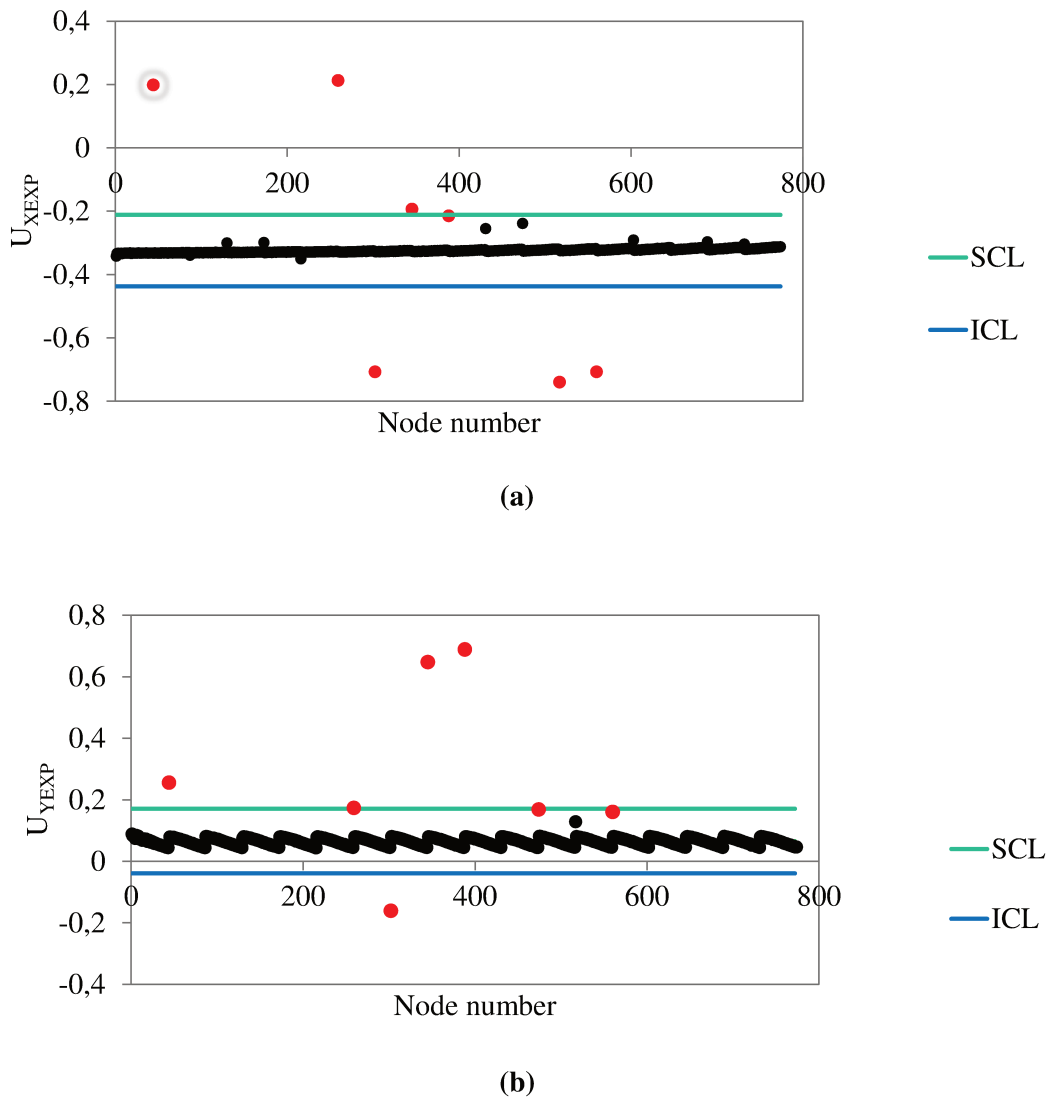


**Figure V-4: Example of controlling limits for displacement during four-point bending test: (a) along X axis, (b) along Y axis. The eliminated points are represented in red color**

### III.4. Objective function

Considering sample geometry, meshing and boundary conditions, the next step consist to compare simulated displacement of each point in the ZOI with the DIC experimental results and, then, to adjust the material properties (Young's modulus  $E$  and Poisson ratio  $\nu$ ) in order to obtain rather same values for all the calculated points in the central part of the sample. Displacement fields were preferred to strain fields in order to avoid additional scattering obtained by differentiating of the data.

It should be noticed here that experimental bending device induces parasite displacement of the sample (rotation around Z-axis:  $\theta_c$ , translation along X and Y axis:  $U_{x_c}$ ,  $U_{y_c}$ ). These displacement parameters must be taken into account in the comparison with FEM simulation results. In this purpose, this rigid body motion of sample must be subtracted to experimental DIC results by using the coordinate (X, Y) of each point and a set of correction displacement parameters ( $\theta_c$ ,  $U_{x_c}$  and  $U_{y_c}$ ). This set allows to determine the experimental coordinates free of rigid body motion ( $\overrightarrow{\text{POS}}_{\text{EXP}}$ ) taking into account the coordinates of each point of the ZOI, and the raw displacement results directly obtained from DIC ( $U_{\text{DIC}}$ ) with its two components  $U_{x_{\text{DIC}}}$  and  $U_{y_{\text{DIC}}}$ .

$$\overrightarrow{\text{POS}}_{\text{EXP}}(\theta_c, U_{x_c}, U_{y_c}) = \begin{pmatrix} (X + U_{x_{\text{DIC}}}) \times \cos \theta_c - (Y + U_{y_{\text{DIC}}}) \times \sin \theta_c - U_{x_c} \\ (X + U_{x_{\text{DIC}}}) \times \sin \theta_c + (Y + U_{y_{\text{DIC}}}) \times \cos \theta_c - U_{y_c} \end{pmatrix} \quad \text{Eq. V-1}$$

Finally, the global optimization must take into account five parameters: three coming from rigid body motion ( $\theta_c$ ,  $U_{x_c}$ ,  $U_{y_c}$ ) and two from material properties (E,  $\nu$ ). These five parameters are gathered in the vector  $\overrightarrow{\text{PARAM}}$  :

$$\overrightarrow{\text{PARAM}} = \begin{pmatrix} \theta_c \\ U_{x_c} \\ U_{y_c} \\ E \\ \nu \end{pmatrix} \quad \text{Eq. V-2}$$

For each point of the ZOI, the difference between experimental and simulated displacements ( $\overrightarrow{U}_{\text{EXP}}$  and  $\overrightarrow{U}_{\text{SIM}}$ ) can be then calculated from the values of their positions ( $\overrightarrow{\text{POS}}_{\text{EXP}}$  and  $\overrightarrow{\text{POS}}_{\text{SIM}}$ ). Searching to reduce the global difference for all the points of the ZOI consists thus in minimizing an objective function  $\phi(\overrightarrow{\text{PARAM}})$  defined as follow:

$$\begin{aligned} \phi(\overrightarrow{\text{PARAM}}) &= \sum_{\text{ZOI}} \left\| \overrightarrow{U}_{\text{EXP}}(\theta_c, U_{x_c}, U_{y_c}) - \overrightarrow{U}_{\text{SIM}}(E, \nu) \right\|^2 \\ \phi(\overrightarrow{\text{PARAM}}) &= \sum_{\text{ZOI}} \left\| \overrightarrow{\text{POS}}_{\text{EXP}}(\theta_c, U_{x_c}, U_{y_c}) - \overrightarrow{\text{POS}}_{\text{SIM}}(E, \nu) \right\|^2 \end{aligned} \quad \text{Eq. V-3}$$

where

$$\overrightarrow{\text{POS}}_{\text{SIM}}(E, \nu) = \begin{pmatrix} X + U_{X_{\text{SIM}}} \\ Y + U_{Y_{\text{SIM}}} \end{pmatrix} \quad \text{Eq. V-4}$$

This minimization of  $\phi(\overrightarrow{\text{PARAM}})$  allows to obtain, by iterative calculation, the sample rigid body motion and the material elastic properties.

### III.5. Newton Raphson optimization method

Prior to apply any inverse estimation procedure, a very simple systematic scanning procedure has been used for the determination of elastic properties in a given predefined range. This method (detailed in appendix C) allows to obtain a good estimation of elastic properties, however, it may require a great computation time depending on the investigated range for each parameter and on the scanned interval between each step of calculation (targeted accuracy).

For a better efficiency, iterative computation optimization methods are usually preferred. The aim of these types of algorithms, which can use different strategies, is to find, in the quickest way, the best set of parameters which leads to the global minima of the objective function. Among the available techniques, gradient based ones are commonly applied such as Newton-Raphson (NR) method, already implemented in DIC software Correla. This NR method has been considered here.

Newton-Raphson method is an iterative numerical technique that allows to find zeros of a mathematical function. Given an initial set of parameters  $\overrightarrow{\text{PARAM}}_0$ , this set can be iteratively refined in a sequence  $\overrightarrow{\text{PARAM}}_0, \overrightarrow{\text{PARAM}}_1, \dots, \overrightarrow{\text{PARAM}}_i, \overrightarrow{\text{PARAM}}_{i+1}$  until the satisfaction of a predefined convergence criterion. The initial set of parameters  $\overrightarrow{\text{PARAM}}_0$  should not be chosen too far from the final solution to avoid any divergence problems. NR technique uses the derivative of the objective function to update the set of parameters at each step of calculation.

To illustrate the algorithm in the simple case of a unique parameter P (example of a vector  $\overrightarrow{\text{PARAM}}$  containing only one coordinate P) and of a basic objective function  $\phi(P)$ ,

Figure V-5 shows that, using the tangent of the objective function  $\phi(P_i)$  for a given step  $P_i$ , the following parameter value  $P_{i+1}$  can be determined.

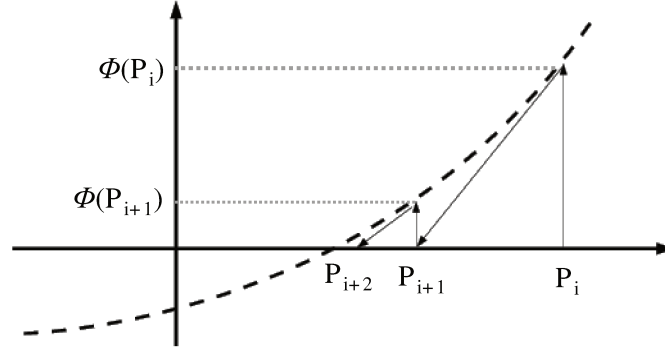


**Figure V-5: Schematic representation for iterative determining of following parameter value  $P_{i+1}$  from a given step  $P_i$**

For a given deviation  $\delta$  from  $P_i$ , an approximation of the objective function  $\phi(P_i + \delta)$  can be expressed by the following Taylor expression:

$$\phi(P_i + \delta) = \phi(P_i) + \delta \cdot \phi'(P_i) + \frac{\delta^2}{2} \phi''(P_i) + \dots \quad \text{Eq. V-5}$$

Neglecting the terms of order higher than 1, and targeting a zero value for  $\phi(P_i + \delta)$ , the expression becomes:

$$\phi(P_i + \delta) = \phi(P_i) + \delta \cdot \phi'(P_i) = 0 \quad \text{Eq. V-6}$$

Then, the following parameter value  $P_{i+1}$  can be determined

$$P_{i+1} = P_i + \delta = P_i - \frac{\phi(P_i)}{\phi'(P_i)} \quad \text{Eq. V-7}$$

In our case, with a vector parameter  $\overrightarrow{\text{PARAM}}$  (containing five unknowns) and with an objective function resulting from a vector norm calculation on the overall ZOI (containing  $n$  points and each point defined by its two coordinates), the NR principle remains the same but should be written in a vectorial form containing  $2.n$  coordinates and the deviation from

$\overrightarrow{\text{PARAM}}_i$  becomes a vector  $\vec{\delta}$  containing five components. Thus the Eq. V-6 becomes vectorial as follows:

$$\vec{\phi}(\overrightarrow{\text{PARAM}}_i + \vec{\delta}) = \vec{\phi}(\overrightarrow{\text{PARAM}}_i) + (J_i) \cdot \vec{\delta} = 0 \quad \text{Eq. V-8}$$

where:

- $\vec{\phi}$  represents the vector from which the numerical objective function  $\phi(\overrightarrow{\text{PARAM}}_i)$  is calculated using its norm. As mentioned previously, taking into account the n points in the ZOI, with the two coordinates of each point, the vector  $\vec{\phi}$  contains 2.n elements and is defined as follows:

$$\vec{\phi} : \mathbb{R}^5 \rightarrow \mathbb{R}^{2n}$$

$$\vec{\phi}(\overrightarrow{\text{PARAM}}_i) = \begin{pmatrix} \phi_{1,x}(\overrightarrow{\text{PARAM}}_i) \\ \phi_{1,y}(\overrightarrow{\text{PARAM}}_i) \\ \phi_{2,x}(\overrightarrow{\text{PARAM}}_i) \\ \phi_{2,y}(\overrightarrow{\text{PARAM}}_i) \\ \vdots \\ \phi_{n,x}(\overrightarrow{\text{PARAM}}_i) \\ \phi_{n,y}(\overrightarrow{\text{PARAM}}_i) \end{pmatrix} \quad \text{Eq. V-9}$$

with  $\phi_{k,x}$  and  $\phi_{k,y}$  are respectively the components of  $\phi$  along x and y axis at the node number k.

- $(J_i)$  is the Jacobian matrix (at the step i) that contains partial derivatives of the first order of  $\phi_{k,x}$  and  $\phi_{k,y}$ . This matrix can be written as following:

$$(J_i) = \begin{pmatrix} \frac{\partial \phi_{1,x}}{\partial \theta}(\overrightarrow{\text{PARAM}}_i) & \frac{\partial \phi_{1,x}}{\partial Ux_c}(\overrightarrow{\text{PARAM}}_i) & \frac{\partial \phi_{1,x}}{\partial Uy_c}(\overrightarrow{\text{PARAM}}_i) & \frac{\partial \phi_{1,x}}{\partial E}(\overrightarrow{\text{PARAM}}_i) & \frac{\partial \phi_{1,x}}{\partial \eta}(\overrightarrow{\text{PARAM}}_i) \\ \frac{\partial \phi_{1,y}}{\partial \theta}(\overrightarrow{\text{PARAM}}_i) & \frac{\partial \phi_{1,y}}{\partial Ux_c}(\overrightarrow{\text{PARAM}}_i) & \frac{\partial \phi_{1,y}}{\partial Uy_c}(\overrightarrow{\text{PARAM}}_i) & \frac{\partial \phi_{1,y}}{\partial E}(\overrightarrow{\text{PARAM}}_i) & \frac{\partial \phi_{1,y}}{\partial \eta}(\overrightarrow{\text{PARAM}}_i) \\ \vdots & \vdots & \vdots & \vdots & \vdots \\ \frac{\partial \phi_{n,x}}{\partial \theta}(\overrightarrow{\text{PARAM}}_i) & \frac{\partial \phi_{n,x}}{\partial Ux_c}(\overrightarrow{\text{PARAM}}_i) & \frac{\partial \phi_{n,x}}{\partial Uy_c}(\overrightarrow{\text{PARAM}}_i) & \frac{\partial \phi_{n,x}}{\partial E}(\overrightarrow{\text{PARAM}}_i) & \frac{\partial \phi_{n,x}}{\partial \eta}(\overrightarrow{\text{PARAM}}_i) \\ \frac{\partial \phi_{n,y}}{\partial \theta}(\overrightarrow{\text{PARAM}}_i) & \frac{\partial \phi_{n,y}}{\partial Ux_c}(\overrightarrow{\text{PARAM}}_i) & \frac{\partial \phi_{n,y}}{\partial Uy_c}(\overrightarrow{\text{PARAM}}_i) & \frac{\partial \phi_{n,y}}{\partial E}(\overrightarrow{\text{PARAM}}_i) & \frac{\partial \phi_{n,y}}{\partial \eta}(\overrightarrow{\text{PARAM}}_i) \end{pmatrix} \quad \text{Eq. V-10}$$

At a given step  $i$ , each term of this Jacobian matrix can be numerically calculated using a predefined set of increments for each parameter to be optimized. The chosen values of these increments are summarized in Table V-1.

**Table V-1: Increment values added to the set of parameters defined in  $\overrightarrow{\text{PARAM}}$**

$dE$	0.1 GPa
$d\nu$	0.001
$d\theta$	$0.001^\circ$
$dX_c$	0.01 mm
$dY_c$	0.01 mm

When  $(J_i)$  is an invertible matrix, the Eq. V-8 can be resolved directly through the following equation:

$$\overrightarrow{\text{PARAM}}_{i+1} = \overrightarrow{\text{PARAM}}_i - (J_i)^{-1} \cdot \vec{\phi}(\overrightarrow{\text{PARAM}}_i) \quad \text{Eq. V-11}$$

However, in our case,  $(J_i)$  is a noninvertible matrix, thus, to solve this system a specific formulation is needed to convert this matrix into an invertible one. This can be obtained using the Moore-Penrose pseudo-inverse matrix  $[(J_i)^T \cdot (J_i)]^{-1} (J_i)^T$  where  $(J_i)^T$  is the transpose matrix. The Eq. V-11 can be rewritten as followed:

$$\overrightarrow{\text{PARAM}}_{i+1} = \overrightarrow{\text{PARAM}}_i - [(J_i)^T \cdot (J_i)]^{-1} \cdot (J_i)^T \cdot \vec{\phi}(\overrightarrow{\text{PARAM}}_i) \quad \text{Eq. V-12}$$

The resolution of the system expressed in the Eq. V-12 consists then on the determination of  $\overrightarrow{\text{PARAM}}_{i+1} - \overrightarrow{\text{PARAM}}_i$  using the Gaussian elimination adapted for solving systems of linear equations.

The numerical calculations explained above should be done at each iteration step. To fix a limit for these iterative calculations, a convergence criterion has been defined as follows:

$$\left\| \overrightarrow{\text{PARAM}}_{i+1} - \overrightarrow{\text{PARAM}}_i \right\| \leq \psi \quad \text{Eq. V-13}$$

where  $\psi$  value is chosen taking into account the DIC measurement noise.

The optimization process takes into account 5 variables included in  $\overline{\text{PARAM}}$ . However, only material parameters will be presented in the following parameters.

## IV. Applications

The first part of this chapter was devoted to the details of FEMU-U technique considered in this work. In the following paragraphs, this developed approach will be applied firstly, on aluminium which exhibits a linear elastic mechanical behaviour, then, on AT VF flexible refractory material supposed to exhibit a significant non-linear behaviour.

### IV.1. Case of aluminium

An aluminium alloy sample (8.5 x 10.5 x 85 mm) has been characterized using four-points bending test. The sample surface has been prepared thanks to the application of white droplets on a black paint layer. Windows of correlation are 32 x 32 pixels<sup>2</sup> in the ZOI limited by the axis of upper rolls as shown in Figure V-6.

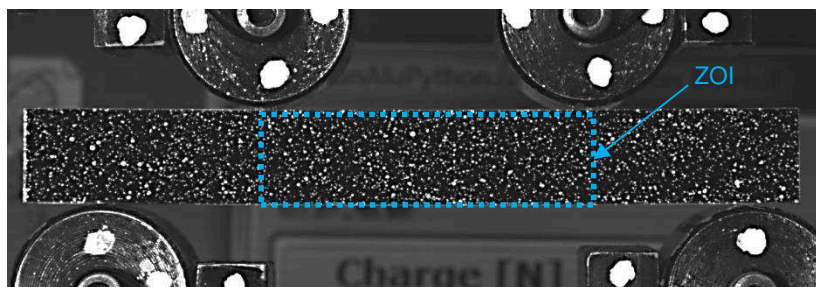
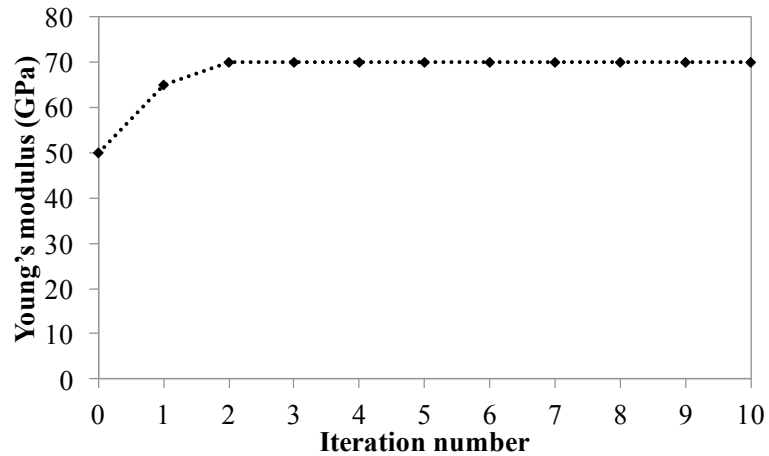


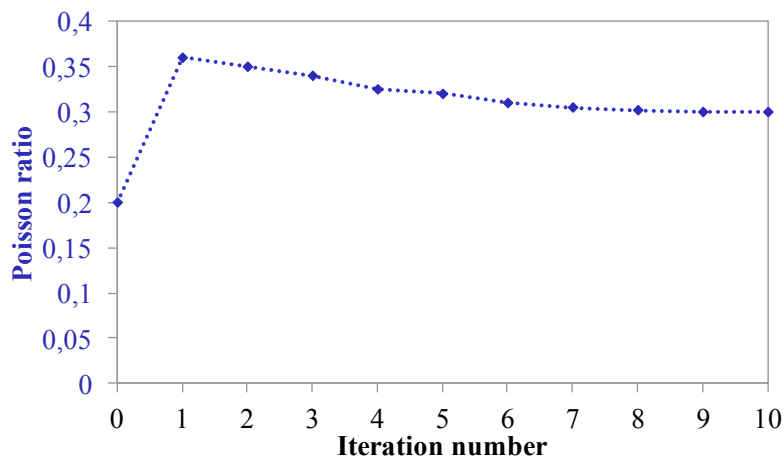
**Figure V-6: Sample image acquisition of aluminium sample during the test**

From displacement field obtained by DIC at a given applied load (2040 N corresponding to a stress level of 131 MPa at the bottom face) and after generating a similar geometry and meshing using Python script, the optimization process is computed and the results of optimization process are given in Figure V-7:





(a)



(b)

**Figure V-7: Young's modulus (a) and Poisson ratio (b) determination**

Young's modulus highly increases in the first iteration, then, rises until stabilization around 70 GPa value. The stabilization was reached in the 2<sup>nd</sup> iteration.

In a similar way, Poisson's ratio extremely strongly increases in the first iteration, then, decreases slightly until its value becomes steady around the value of 0.3 reached in the 8<sup>th</sup> iteration.

The aluminium material has been studied here in order to check the efficiency of FEMU-U. Elastic properties of such materials can be estimated correctly using the classical equations which are valid only for materials whose behaviour is pure elastic.

## IV.2. Case of AT VF sample

The main reason for FEMU-U development was initially to estimate mechanical properties of materials with specific non-linear behaviour as their characterization is often still done using classical equations as explained in chapter I. For this reason, the following application of FEMU-U will be on an AT VF sample (10.5 x 12.5 x 85 mm) introduced in chapter II and characterized using DIC developed in chapter III.

For such material with a non-linear mechanical behaviour, it is more relevant to use a non-linear stress-strain law that takes into account damage evolution during loading.

In order to represent material damage in Code Aster, it is possible to use “softening” behaviours in which, after reaching a threshold (stress or strain), stress decreases as strain values increase. In Code Aster, such behaviour may be obtained by:

- using elasto-plastic models with negative hardening such as BETON\_DOUBLE\_DP and DRUCK\_PRAGER laws.
- taking into account the growth of cavities with plasticity such as the ROUSSELIER law which describes an elasto-plastic behaviour.
- adding an interne variable  $D$  which vary between 0 and 1 and represents the decrease of material Young’s modulus compared to its initial values  $E_0$ :

$$E = (1 - D) \times E_0 \quad \text{Eq. V-14}$$

This variable was introduced by Kachanov (Kachanov, 1958) who pioneered the concept of the effective (undamaged) configuration and introduced the basis for the continuum damage mechanics theories. From the Eq. V-14, the material is completely damaged for  $D=1$ . Followed by his pioneering work, many researchers have used the effective configuration concept to model the irreversible damage processes in engineering materials (Lemaitre et al., 1990).

As an example, damage law of Lemaître-Chaboche (VENDOCHAB law) has been used by Leplay (Leplay, 2011) to simulate damage in a similar material and might has been interesting in our case for AT VF. This VENDOCHAB law is expressed by the following equation:

$$D(\varepsilon_{\text{eq}}) = a.(1 - \exp(-\frac{\varepsilon_{\text{eq}}}{b})) \quad \text{Eq. V-15}$$

where  $a$ ,  $b$  are parameters of the damage law,  $\varepsilon_{\text{eq}}$  is the equivalent strain which may be obtained by :

$$\varepsilon_{\text{eq}} = \langle \varepsilon_1 \rangle_+ + \langle \varepsilon_2 \rangle_+ + \frac{\nu}{1-\nu} \langle -\varepsilon_1 - \varepsilon_2 \rangle_+ \quad \text{Eq. V-16}$$

where  $\varepsilon_1$  and  $\varepsilon_2$  are the principal strains and  $\langle \rangle_+$  are Macaulay brackets.

This would have required to take into account, in the previous python development, additional parameters ( $a$ ,  $b$  and  $E_0$ ). However, due to the lack of time for further script development during the PhD, the computation in the case of AT VF has been managed only considering the 5 parameters contained in the vector  $\overrightarrow{\text{PARAM}}$  which has been defined previously (Eq. V-2) for a linear elastic behaviour. Nevertheless, in order to consider the change in elastic property during loading, different steps (from A to E in Figure V-8) corresponding to increasing level of load have been analysed. Such approach will only allow us to estimate an average damage parameter at each step.

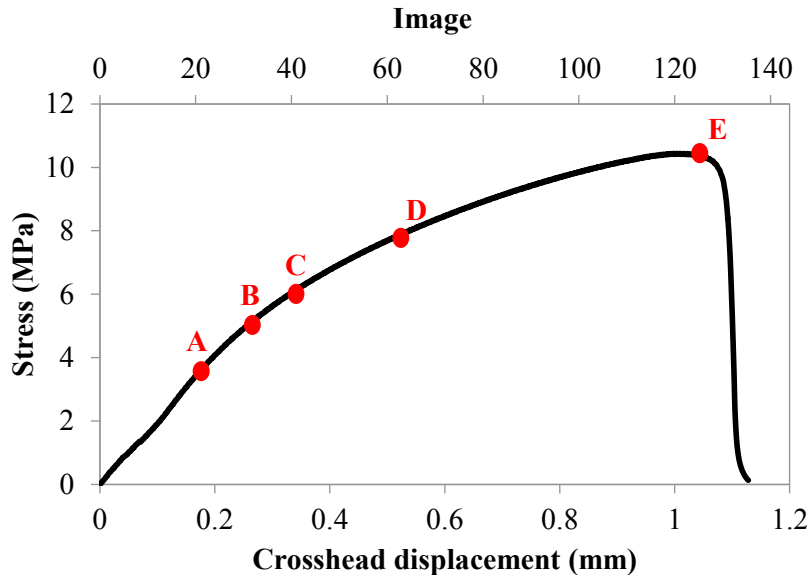
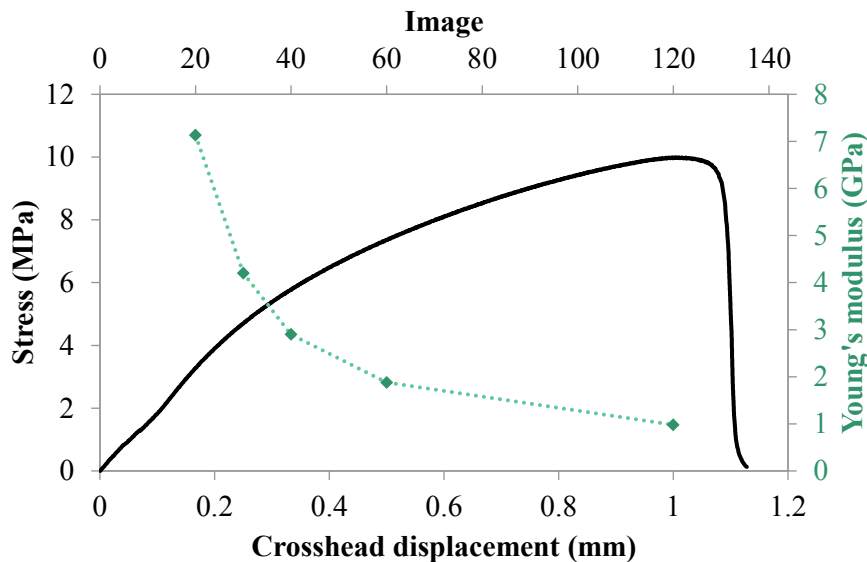


Figure V-8: Stress-displacement curve of AT VF with the analyzed stages by FEMU-U

From displacement fields obtained by DIC at these steps, a simulated geometry and meshing identical to the experimental one has been generated using Python script (as explained before), then, the optimization process of  $\overline{\text{PARAM}}_{\text{ATVF}}$  was computed. The evolution of the obtained Young's modulus, which represents material rigidity, values for these five stages is represented in Figure V-9.

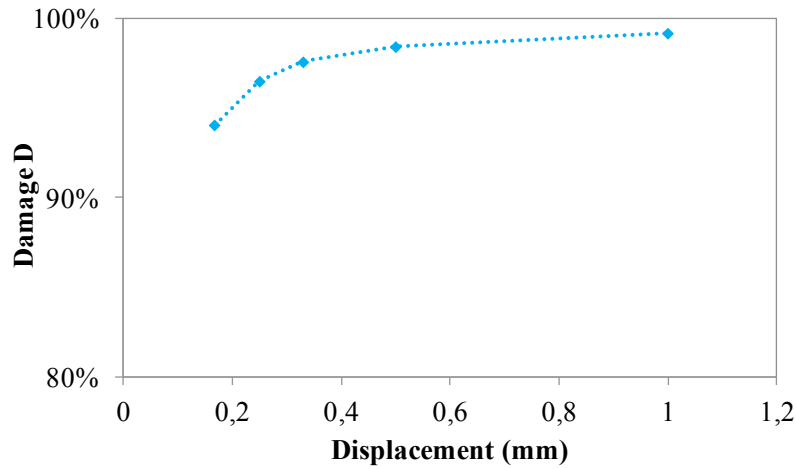


**Figure V-9: Evolution of Young's modulus values obtained by FEMU-U**

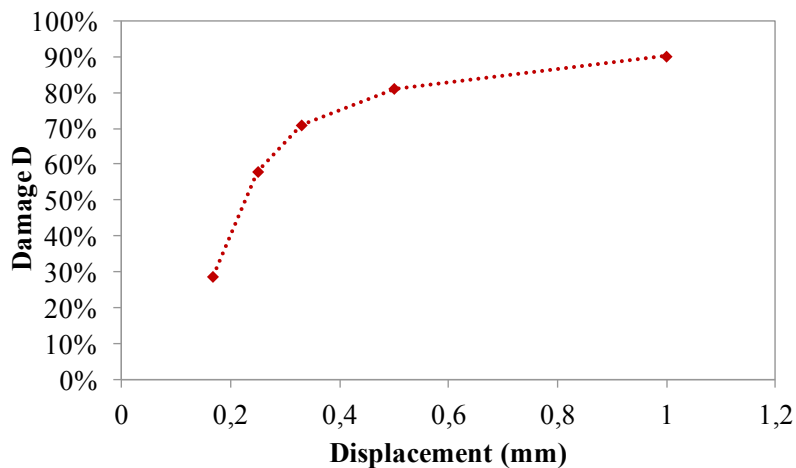
In fact, as the applied load increases, Young's modulus decreases due to the development of micro-cracks network already present in the AT VF (chapter III: § II.2) and so, damage level is enhanced.

From Young's modulus values, the evolution of damage  $D$  was obtained using the Eq. V-14 and an initial Young's modulus value at room temperature  $E_0^d \sim 10$  GPa (chapter III: Figure III-4). This evolution has been represented with the red curve in Figure V-10b. However,  $E_0^d$  value takes into account the pre-existing damage within the microstructure of AT VF material induced by cooling. In order to consider this damage, another evolution of damage has been calculated based on this  $E_0^{nd}$  value which has been chosen for a state in which micro-cracks are closed and the value considered is around

$E_0^{\text{nd}} \sim 160$  GPa (chapter III: Figure III-4). From this, a second curve (blue one) has been represented in Figure V-10a.



(a)



(b)

**Figure V-10: Evolution of damage for AT VF material: (a) referred to an initial Young's modulus without any damage, (b) referred to an initial Young's modulus taking into account the damage induced during cooling**

From the evolution of damage for AT VF without any damage (Figure V-10a), there is only 5% of damage induced by the applied stresses. This confirms that the majority of damage is induced during thermal treatment and especially during cooling. Besides, in the case of AT VF with damage, the damage represented in Figure V-10b corresponds mainly to damage induced by the mechanical solicitation.

## V. Conclusion

The main objective here was to describe and to apply FEMU-U which is a numerical tool that allows determining material properties from displacement fields obtained by DIC.

Due to the lack of FEMU-U skills in the laboratory, the first step was to acquire enough knowledge in this field and to develop numerically the adopted technique using Python. The adopted approach has been detailed in the first part of this chapter.

Using experimental four-points bending test, FEMU-U method has been applied first on aluminium that exhibits a linear elastic behaviour. This first step has allowed us to validate the efficiency of the developed FEMU-U tool. Then, in a second step, this developed approach has been applied on AT VF material and allows determining elastic properties at different load level. From these values, damage evolution was then deduced.

## Conclusion and perspectives

High local thermal stresses induced by thermal shocks can be catastrophic in many cases for industrial refractory installations. Thermal shock resistance of materials is known to be closely related to their crack growth resistance behaviour. For this reason, acquiring better knowledge in the field of thermomechanical properties of refractories is of a prime importance to improve this thermal shock resistance. This latter is linked to the ability of refractory materials to exhibit a specific non-linear mechanical behaviour promoted by a voluntary micro-cracked initial microstructure.

In order to characterize such non-linear behaviour, stress-strain laws determination during uniaxial loading is required. For this purpose, specific tensile tests were developed in different laboratories during the past 15 years. Recently, the occurrence of optical techniques like digital image correlation (DIC), that allows recording strain fields on sample surface during a mechanical test, has found a very interesting application in the characterization of refractory materials.

The aim of the present thesis was to apply digital image correlation as a support for the experimental characterization of refractory materials with specific non-linear behaviour using quite common mechanical tests for refractories.

To do so, different types of materials were chosen as they exhibit such behaviour thanks to an initial network of micro-cracks voluntary generated within their microstructure:

- A single phase model flexible aluminium titanate (AT VF) material developed for academic purposes by improving the grain growth. Its non-linear mechanical behaviour was obtained thanks to the thermal expansion mismatch of its grains according to the different crystallographic axis.
- Multi-phased industrial magnesia materials that exhibit a non-linear mechanical behaviour (less accentuated than AT VF), thanks to the mismatch between thermal expansion coefficients of its different phases.

The experimental part allowed, in a first step, to acquire enough expertise about the optical techniques such as DIC and mark tracking method thanks to cooperation with Pprime laboratory (Poitiers - France).

In a second step, DIC has been applied on an AT VF material during four-points bending test at room temperature. The obtained results in this part allowed to underline an asymmetric mechanical behaviour which induces a significant shift of the neutral fibre. Besides, using mark tracking method, the relative variations of the distance between rolls and their individual rotations (avoiding friction) were quantified.

After the validation of the efficiency of DIC on AT VF, the following step was to apply this optical technique on industrial refractory materials (magnesia spinel and magnesia hercynite) which are characterized by lower strain-to-rupture level. To do so, an optimisation of the experimental testing conditions and of the images treatments, in order to improve DIC measurements accuracy, was required. In addition to four-points bending, other common mechanical tests for refractories were also investigated: Brazilian test and Wedge Splitting test.

The experimental study using Brazilian test combined to DIC confirms clearly that tensile stresses, which are acting horizontally in the central part of the sample, are behind the occurrence of the vertical crack which appears in the central part of the sample and which induces material failure. Besides, Wedge Splitting test associated to DIC allows to underline the presence of crack branching phenomenon in such multi-phased material which is promoted thanks to initial micro-cracks network voluntarily introduced by thermal expansion mismatch between the different phases (magnesia, spinel and hercynite). Since these initial micro-cracks promote crack branching, they enhance the non-linearity of the mechanical behaviour. Additionally, at each stage, from the evolution of strain fields during the test, crack's length has been estimated using DIC during Brazilian test and Wedge splitting test. Even if Brazilian test is not dedicated for such purpose, crack's length evolution has been combined to the dissipated energy in the aim to represent the R-curves behaviour in both cases.

The numerical part was focused on the development of finite element method updating (FEMU-U) which couples displacement fields obtained by DIC with finite element method in the aim to determine material properties. Similarly to DIC, the first step was to acquire



enough knowledge for the development of this method at SPCTS laboratory. In a second step, the adopted approach was programmed using python language, then, firstly applied on an aluminium material whose mechanical behaviour is well known (linear elastic) and whose Young's modulus is in the same range of refractory materials. The chosen experimental test for this application was the four-points bending test as induced displacement values are higher in comparison with Brazilian test and Wedge Splitting test.

After validation of the FEMU-U using aluminium, the developed technique was applied on AT VF material in the purpose of elastic properties determination at different load levels. This allows the quantification of Young's modulus decrease (increase of material damage) with the increase of the applied stress.

The perspectives of this work could be numerous. First, concerning the experimental part, the optimisation of DIC may allow this technique to be extended for other applications from macro-scale strains characterization to micro-scale one. Indeed, strains are usually measured at macroscopic level because of the need of homogeneous material equivalent properties. However, due to anisotropy of individual grains (as in the case of aluminium titanate) and or due to heterogeneities of phases (as in the case of industrial refractory materials), it could also be very interesting to record strain field at local scale (combining DIC with microscope) to study in more details the influence of microstructure organisation during loading.

In the present work, DIC has been only applied at room temperature. But, in the case of refractories, it could be also useful to do similar experiments at high temperature (similar conditions to industrial applications). Image acquisition for accurate strain measurement at high temperature is not an easy task since many additional parameters can disturb the data: thermal expansion of the sample itself due an unstable temperature, luminosity variation due to working conditions within the furnace above 600°C, thermal convection flux which can modify local optical properties of the air between the sample and the camera.

Concerning the numerical part, the work on the developed approach of FEMU-U has to be continued in order to take into account a non-linear strain-stress law for identification of the material properties. To do so, other stress-strain law has to be investigated and additional parameters have to be considered in Newton Raphson optimization. Besides, this developed approach can also be adapted to other mechanical tests such as Brazilian test and Wedge

Splitting tests. Finally, from the eventual displacement fields obtained at high temperature by DIC, the identification of material properties may be evaluated also at high temperature.

# Appendix A

## EDS analysis on MS, MST1 and MST2 materials

These analyses were done in the aim to investigate the microstructure of the industrial materials processed by RHI.

The results show that the main difference between MS (Figure A-1), MST1 (Figure A-2) and MST2 (Figure A-3) materials is the type of spinel inclusions inside magnesia matrix. In fact, MST1 contains hercynite grains ( $\text{FeAl}_2\text{O}_4$ ) in addition to spinel grains ( $\text{MgAl}_2\text{O}_4$ ) present in MS sample. Besides, MST2 is mainly composed of hercynite and magnesia.

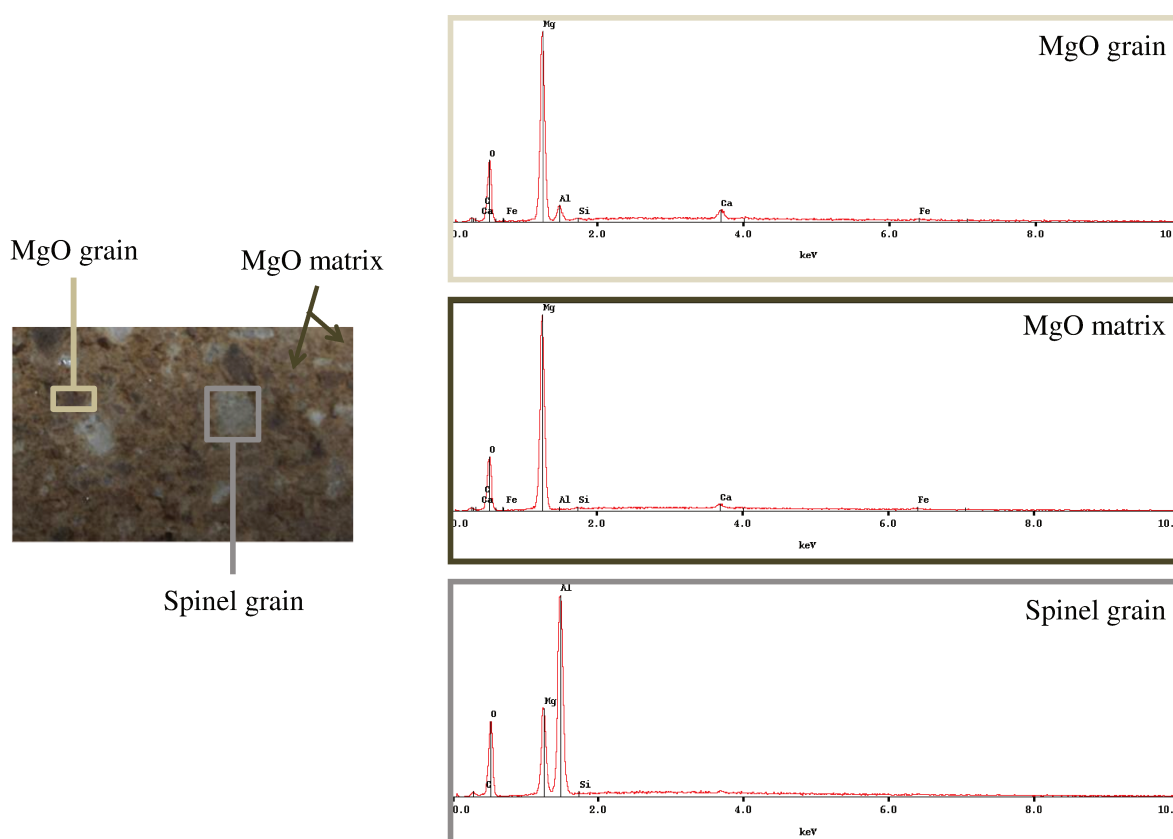


**Figure A-1: An example of the EDS analysis on a MS sample**

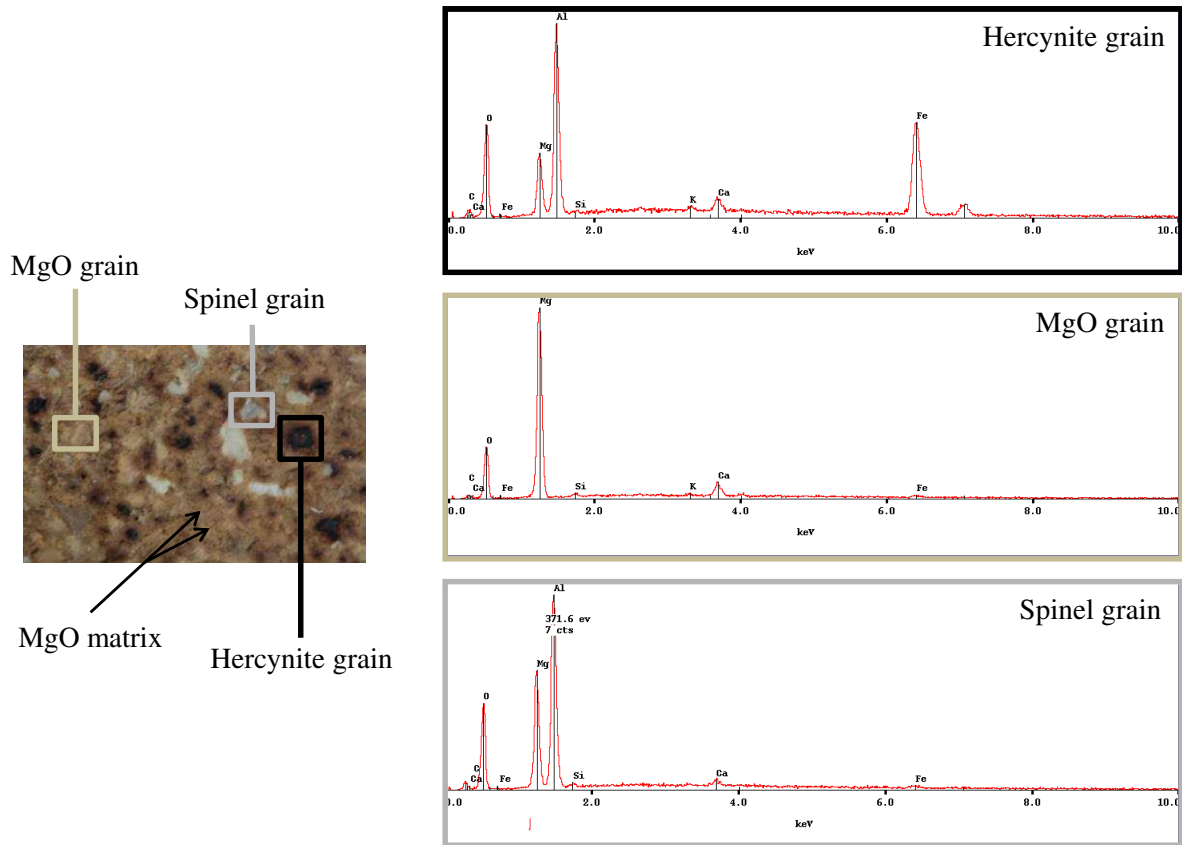


Figure A-2: An example of the EDS analysis on a MST1 sample

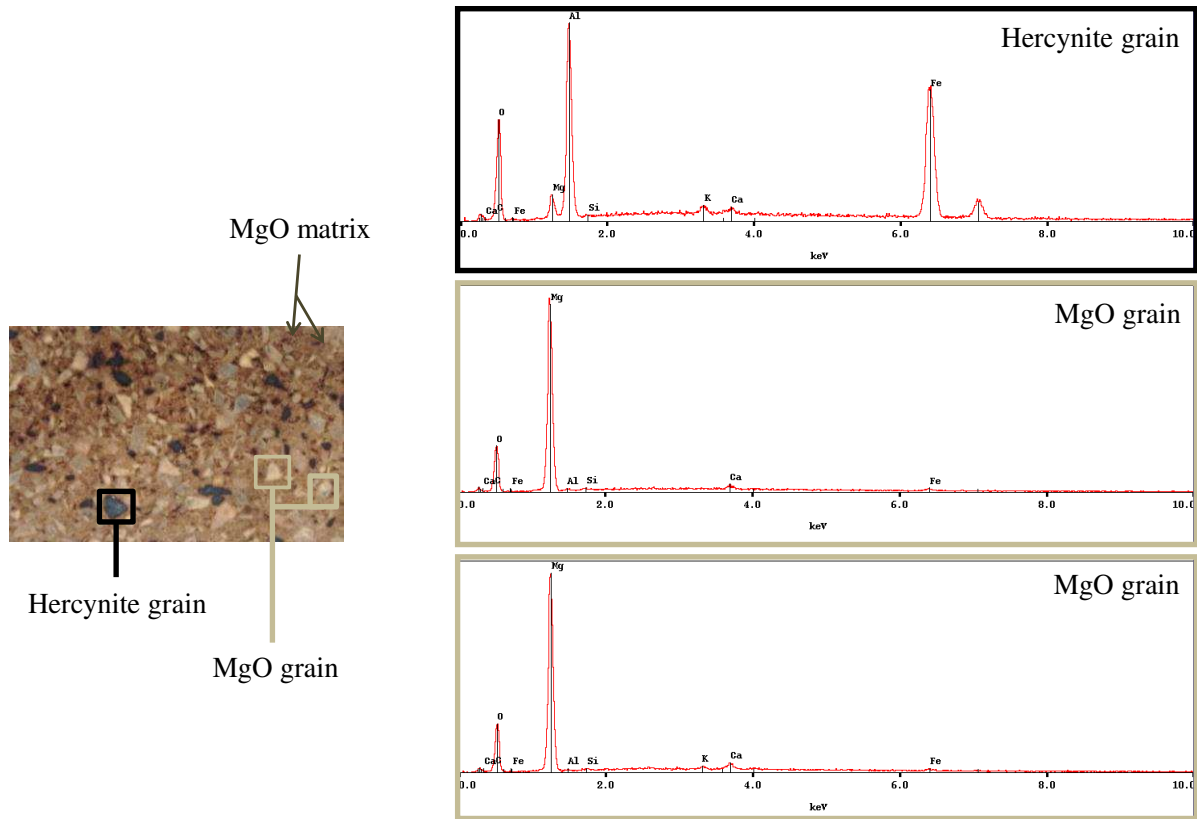


Figure A-3: An example of the EDS analysis on a MST2 sample

# Appendix B

## Influence of carbon rate, binder type and antioxidant addition on the non-linear mechanical behaviour of magnesia refractories

### **B.1. Materials selection**

The initial purpose of the work described in this part was to obtain some information about the thermo-mechanical behaviour of magnesia carbon refractories used in steelmaking vessels. The idea was to focus on different process parameters that could affect materials properties. Five types of magnesia carbon bricks were provided by RHI. Starting from similar magnesia aggregates, the aim was to evaluate the effect of carbon content, binder type and additives presence.

#### ❖ **Pitch bonded magnesia carbon:**

- 5% of carbon (MgO-5%C-PB)
- 10% of carbon (MgO-10%C-PB)
- 14% of carbon (MgO-14%C-PB)

#### ❖ **Resin bonded magnesia carbon:**

- 10% of carbon (MgO-10%C-RB)
- 10% of carbon with an antioxidant (Aluminium) (MgO-10%C-RB-AL)

Due to materials anisotropy, all mechanical characterizations (stresses during four-points bending tests) have been managed along the pressing direction (Figure B-1).

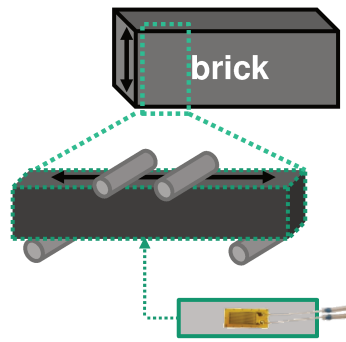


**Figure B-1: Scheme of the characterized direction which is parallel to pressing direction**

## B.2. Microstructure analysis

Density and porosity were calculated according to ASTM C830-00. From these results, and thanks to ultrasonic technique at room temperature in transmission mode, elastic properties were calculated and presented in Table B-1.

**Table B-1: Density, porosity and elastic properties of the different magnesia carbon studied materials**

	Pitch Bonded (PB)			Resin Bonded (RB)	
	5% C	10% C	14% C	10% C	10% C+Al
Density (g.cm <sup>-3</sup> )	3.13 (+/- 0.01)	2.99 (+/- 0.02)	2.92 (+/- 0.02)	3.02 (+/- 0.06)	3.08 (+/- 0.01)
Porosity (%)	7.43 (+/- 0.32)	8.82 (+/- 0.24)	7.63 (+/- 0.26)	8.78 (+/- 0.26)	1.55 (+/-0.16)
Young's modulus					
E (GPa)	30.36 (+/- 1.54)	11.67 (+/-0.06)	9.69 (+/- 1.14)	12.35 (+/- 0.70)	30.36 (+/- 1.54)
Shear modulus G					
(GPa)	12.69 (+/- 0.65)	4.60 (+/- 0.05)	3.77 (+/- 0.62)	4.61 (+/- 0.23)	12.69 (+/- 0.65)
Poisson ratio $\nu$	0.20 (+/- 0.08)	0.27 (+/- 0.02)	0.29 (+/- 0.05)	0.33 (+/-0.02)	0.20 (+/- 0.08)

### B.3.Mechanical behaviour characterization

#### B.3.1. Stress-strain curves obtained using four-points bending test

Figure B-2 represents the evolution of stress-strain curves obtained during four-points bending test using strain gages for the different studied materials.

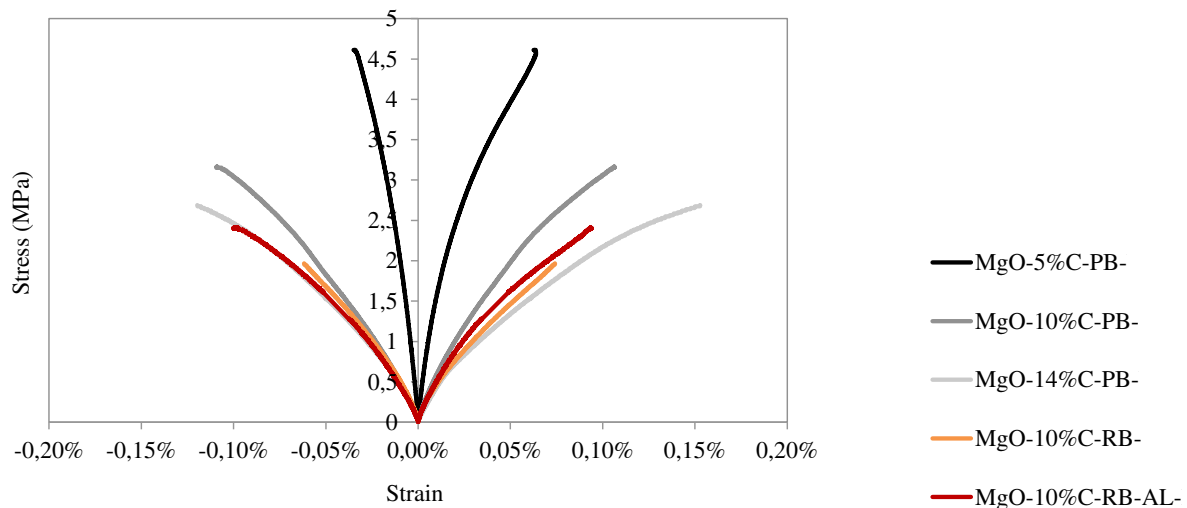


**Figure B-2: Stress-strain curves of the different MgO-C samples**

The observed stress-strain laws are nonlinear for all materials (Figure B-2). The addition of carbon (MgO-5%C-PB, MgO-10%C-PB and MgO-14%C-PB) seems to increase strain-to-rupture and to decrease stress-to-rupture. Pitch binder allows getting higher stress-to-rupture and low strain-to-rupture in comparison with resin binder (MgO-10%C-PB and MgO-10%C-RB). Besides, the addition of the antioxidant to resin samples improves stress-to-rupture and strain-to-rupture (MgO-10%C-RB and MgO-10%C-RB-AL).

From the maximum value of the applied load, the stress-to-rupture values are calculated using the Eq. II-6 that assumes symmetry between tension and compression behaviours. Young's modulus values were evaluated at the beginning of these curves. The values are given in Figure B-2.



**Table B-2: Mechanical parameters obtained during four-points bending test**

	Pitch bonded			Resin bonded	
	5% C	10% C	14% C	10% C	10% C+Al
$E_{\text{compression}}$ (GPa)	28.57	7.90	6.37	9.81	9.44
$E_{\text{tension}}$ (GPa)	27.04	6.86	5.80	8.78	7.38
$\sigma_{\text{max}}$ (MPa)	4.61	3.17	2.69	1.97	2.21

### B.3.2. Asymmetrical behaviour thanks to DIC approach

These materials have different levels of asymmetry between tension and compression. For this reason, their asymmetrical behaviour was underlined using DIC by plotting the evolution of the neutral fiber. Figure B-3 represents the behaviour of two samples: MgO-5%C-PB and MgO-14%C-PB.

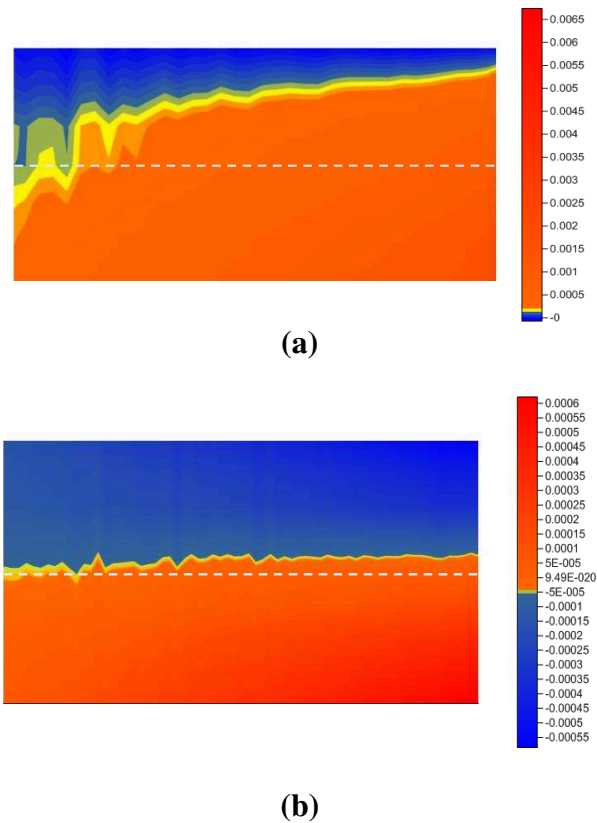


**Figure B-3: Evolution of neutral fiber for MgO-5%C-PB (a) and MgO-14%C-PB (b)**

In both samples, at the beginning of the test, the neutral fibre is localized in the central part of sample. As the load applied increases, it shifts highly in the case of MgO-5%C-PB due to the asymmetrical behaviour in tension and compression and it moves up slightly in the case MgO-14%C-PB due to a quite symmetry between tensile and compressive levels. The high symmetrical behaviour of MgO-5%C-PB in comparison with the other samples was not predicted as it exhibits a less accentuated nonlinear mechanical behaviour.

# Appendix C

## Scanning approach of FEMU-U

As a first step of numerical implementation, a determination of elastic properties was managed by a scanning of elastic parameters in a predefined interval. This method was applied on an aluminum alloy sample with the dimensions 10.22 x 20.11 x 139.05 mm during four-points bending test. The sample surface has been prepared using black droplets on a white paint layer. The ZOI is limited by the upper rolls. Windows of correlation are 32 x 32 pixels<sup>2</sup>. Simulated meshing has been created to be similar to the representation in Figure V-2 (chapter V). The analyzed step (A) chosen for elastic properties determination is represented in Figure C-1.

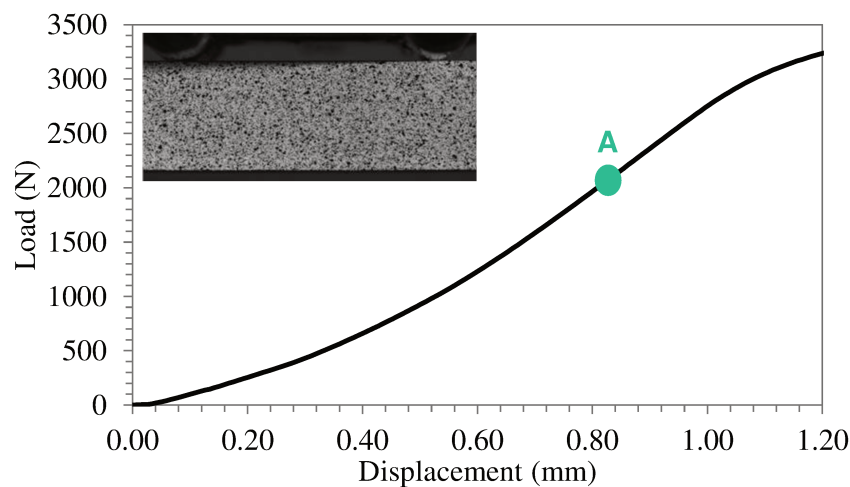


**Figure C-1: Load-displacement curve of aluminum alloy and the analyzed stage for elastic properties determination**

A first scanning of elastic properties has been done in a defined interval so as to determine the localization of the parameters that minimize the gap between experimental and simulated displacements. Unlike Poisson ratio, Young's modulus has a great influence on this difference, for this reason Poisson ratio has been here considered fixed. The first chosen interval of Young's modulus variation can be large and high value for calculation step is usually chosen in order to minimize computation time (for instance, a first scanning can be

obtained in few hours for a large interval [0 GPa – 100 GPa] with a calculation step of 10 GPa).

From this first scanning, an idea about the minimum localization is obtained. Then, a refinement of the interval of Young's modulus variation is set and lower calculation step is chosen. The evolution of the gap between experimental and simulated results with a refined scanning window is represented versus Young's modulus variation in Figure C-2.

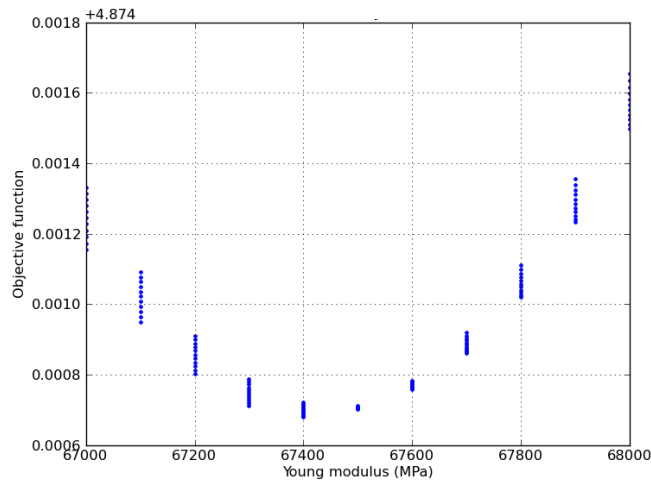


**Figure C-2: The evolution of the gap between experimental (non-corrected values of  $U_{EXP}$ ) and simulated results obtained for different Young's modulus values for loading in the stage A**

The minimum of this function corresponds to the parameter allowing a best matching between  $U_{SIM}$  and  $U_{EXP}$  obtained using DIC.

These results did not take into account the influence of rigid body motion parameters on  $U_{EXP}$ . For this reason, an estimation of these last parameters has been obtained using a least squares minimization taking into account displacement results calculated with a simulated state for which elastic properties have been chosen closed to well-known values for an aluminum ( $E=73$  GPa and  $\nu=0.33$ ). From this evaluation,  $U_{EXP}$  has been corrected using the following equations:

$$U_{YEXP\_cor} = U_{XEXP} \cdot \cos \theta - U_{YEXP} \sin \theta + X_c \quad \text{Eq. C-1}$$

$$U_{YEXP\_cor} = U_{XEXP} \cdot \sin \theta + U_{YEXP} \cos \theta + Y_c \quad \text{Eq. C-2}$$

Using these corrected experimental displacements, a new scanning to estimate the gap between experimental and simulated results has been managed again as explained previously within a large, and then refined Young's modulus values interval, and results obtained for this last refined interval are presented in Figure C-3.

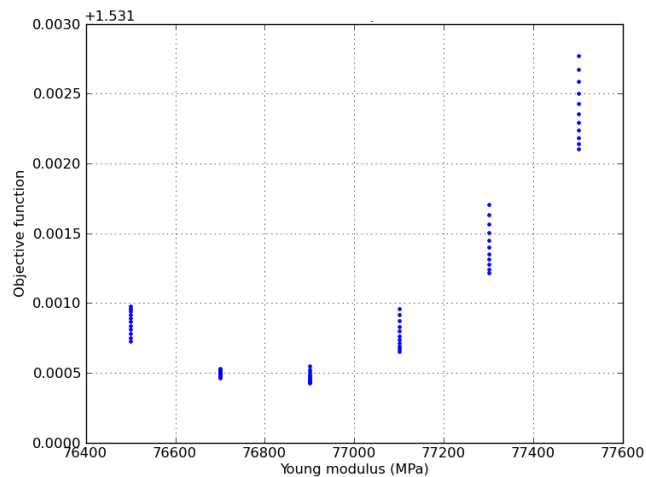


**Figure C-3: Objective function estimation versus Young's modulus after  $U_{EXP}$  correction**

Table C-1 summarizes the Young's modulus and the rigid body motion parameters obtained with this here presented scanning approach on the studied aluminium sample.

**Table C-1: Young's modulus and rigid body motion parameters obtained by scanning approach**

	Before correction	After correction
E (GPa)	67.40	76.90
$T_x$ (mm)	-	0.41
$T_y$ (mm)	-	-0.09
$\theta$ (degree)	-	0.0020

The obtained value of Young's modulus after rigid body motion correction is then not so far from the well-known value of 73 GPa.

## Publications and presentations

**Journal of the European Ceramic Society, Volume 32, Issue 16, Pages 4073-4081, December 2012**

**Application of optical methods to investigate the non-linear asymmetric behavior of ceramics exhibiting large strain to rupture by four-points bending test**

Y. Belrhiti, A. Gallet-Doncieux, A. Germaneau, P. Doumalin, J.C. Dupré, A. Alzina, P. Michaud, I.O. Pop, M. Huger, T. Chotard

**Journal of the European Ceramic Society, Volume 35, Issue 2, Pages 823–829, February 2014**

**Investigation of the impact of micro-cracks on fracture behavior of magnesia products using wedge splitting test and digital image correlation**

Y. Belrhiti, O. Pop, A. Germaneau, P. Doumalin, J.C. Dupré, H. Harmuth, M. Huger, T. Chotard

**International Journal of Applied Ceramic Technology, volume 11, Issue 6, pages 1025-1029, December 2014**

**Characterization of the mechanical behavior of magnesia spinel refractories using image correlation**

Y. Belrhiti, M. Huger, T. Chotard, O. Pop, A. Germaneau, P. Doumalin, J.C. Dupré

**IOP Conference Series: Materials Science and Engineering, 119 (2016) 012010**

**Refinement of digital image correlation technique to investigate the fracture behaviour of refractory materials**

Y. Belrhiti, O. Pop, A. Germaneau, P. Doumalin, J.C. Dupré, M. Huger, T. Chotard

**Journées annuelles GFC, 3-5 April 2012, Mittelwihr, France**

***Application de la technique de corrélation d'images numériques pour étudier le comportement non linéaire de céramiques flexibles***

Y. Belrhiti, A. Gallet-Doncieux, P. Doumalin, J.C. Dupré, A. Germaneau, A. Alzina, P. Michaud, O. Pop, M. Huger, T. Chotard

**ALAFAR 2012, 5 – 8 November 2012, Cancun, Mexico**

**Investigation of the non-linear behavior of flexible ceramics thanks to digital image correlation**

Y. Belrhiti, A. Germaneau, P. Doumalin, J.C. Dupré, A. Alzina, P. Michaud, I.O. Pop, M. Huger, T. Chotard

**Journées Spécialisées sur les Céramiques Réfractaires, 28-29 November 2012, Mons, Belgium**

**Studying the Nonlinear Mechanical Behaviour of Flexible Ceramics Thanks To Digital Image Correlation**

Y. Belrhiti, A. Germaneau, P. Doumalin, J.C. Dupré, A. Alzina, P. Michaud, I.O. Pop, M. Huger, T. Chotard

**PhotoMechanics 2013, May 27 - 29, 2013, Montpellier University, France**

**Study of the Mechanical Behaviour of a Flexible Ceramic by Optical Methods (Poster)**

Y. Belrhiti, A. Germaneau, P. Doumalin, J.C. Dupré, A. Alzina, P. Michaud, I.O. Pop, M. Huger, T. Chotard

**13th International Conference on Fracture ICF, 16-21 June 2013, Beijing, China**

**The Mechanical Fracture Characterization of Non-Linear Flexible Ceramics Using Digital Image Correlation**

Y. Belrhiti, I.O. Pop, P. Doumalin, J.C. Dupré, T. Auer, D. Gruber, H. Harmuth, M. Huger, T. Chotard

**13<sup>th</sup> International Conference of the European Ceramic Society ECERS, 23-27 June 2013, Limoges, France**

**Studying the non-linear mechanical behavior of refractories thanks to digital image correlation**

Y. Belrhiti, A. Germaneau, P. Doumalin, J.C. Dupré, I.O. Pop, M. Huger, T. Chotard

**Unified International Technical Conference on Refractories, UNITECR, 10-13 September 2013, Victoria, Canada**

**The use of digital imaging technique to support mechanical behavior analysis for evaluation of the thermal shock ability of refractories**

Y. Belrhiti, A. Germaneau, P. Doumalin, J.C. Dupré, I.O. Pop, M. Huger, T. Chotard

**Matériaux 2014, Montpellier, France**

**Caractérisation du comportement mécanique de céramiques flexibles à base de titanate d'aluminium en utilisant la corrélation d'images et le recalage par éléments finis**

Y. Belrhiti, A. Germaneau, P. Doumalin, J.C. Dupré, I.O. Pop, M. Huger, T. Chotard

**International Conference on Materials, Processing and Product Engineering, 03-05 November 2015, Leoben, Austria**

**Refinement of digital image correlation technique to investigate the fracture behaviour of refractory materials**

Y. Belrhiti, I.O. Pop, A. Germaneau, P. Doumalin, J.C. Dupré, M. Huger, T. Chotard

## References

- Abanto-Bueno, J., Lambros, J., 2002. Investigation of crack growth in functionally graded materials using digital image correlation. *Eng. Fract. Mech.* 69, 1695–1711.
- Adams, T.E., Landini, D.J., Schumacher, C.A., Bradt, R.C., 1981. Micro and macrocrack growth in alumina refractories. *Am. Ceram. Soc. Bull.* 60, 730–735.
- Akazawa, T., 1943. Méthode pour l'essai de traction de bétons. *Jpn. Civ. Eng. Inst.* 1943. Republished *Fr. Bull. RILEM* 16 Paris 1953 13–23.
- Aksel, C., Rand, B., Riley, F.L., Warren, P.D., 2002. Mechanical properties of magnesia-spinel composites. *J. Eur. Ceram. Soc.* 22, 745–754.
- Andreev, G.E., 1991. A review of the Brazilian test for rock tensile strength determination. Part I: calculation formula. *Min. Sci. Technol.* 13, 445–456.
- Avril, S., Bonnet, M., Bretelle, A.S., Grédiac, M., Hild, F., Jeny, P., Latourte, F., Lemosse, D., Pagano, S., Pagnacco, E., Pierron, F., 2008. Overview of identification methods of mechanical parameters based on full-field measurements. *Exp. Mech.* 48, 381–402.
- Babelot, C., Guignard, A., Huger, M., Gault, C., Chotard, T., Ota, T., Adachi, N., 2010. Preparation and thermomechanical characterisation of aluminum titanate flexible ceramics. *J. Mater. Sci.* 46, 1211–1219.
- Babelot, C., Guignard, A., Michaud, P., Tessier-Doyen, N., Gault, C., Huger, M., Chotard, T., 2009. Aluminium titanate as model material to promote thermal shock resistance of refractory materials, in: *Proceedings UNITECR*. Salvador, Brasil, p. 55.
- Barla, G., Innaurato, N., 1973. Indirect tensile testing of anisotropic rocks. *Rock Mech.* 5, 215–230.
- Barranger, Y., Doumalin, P., Dupré, J.C., Germaneau, A., 2012. Strain measurement by digital image correlation: Influence of two types of speckle patterns made from rigid or deformable marks. *Strain* 48, 357–365.
- Barthelat, F., Wu, Z., Prorok, B.C., Espinosa, H.D., 2003. Dynamic torsion testing of nanocrystalline coatings using high-speed photography and digital image correlation. *Exp. Mech.* 43, 331–340.
- Bastawros, A.-F., Bart-Smith, H., Evans, A.G., 2000. Experimental analysis of deformation mechanisms in a closed-cell aluminum alloy foam. *J. Mech. Phys. Solids* 48, 301–322.
- Baxendale, S., 2004. Testing of refractory materials, in: *Refractories Handbook*. CRC Press, pp. 435–74.
- Bay, B.K., 1995. Texture correlation: A method for the measurement of detailed strain distributions within trabecular bone. *J. Orthop. Res.* 13, 258–267.
- Bing, P., Hui-min, X., Tao, H., Asundi, A., 2009. Measurement of coefficient of thermal expansion of films using digital image correlation method. *Polym. Test.* 28, 75–83.
- Bornert, M., Brémand, F., Doumalin, P., Dupré, J.-C., Fazzini, M., Grédiac, M., Hild, F., Mistou, S., Molimard, J., Orteu, J.-J., Robert, L., Surrel, Y., Vacher, P., Wattrisse, B., 2008. Assessment of digital image correlation measurement errors: Methodology and results. *Exp. Mech.* 49, 353–370.
- Boyle, R.W., 1962. A method for determining crack growth in notched sheet specimens. *Mater. Res. Stand.* 2, 646–651.
- Bradt, R.C., 1981. Problems and possibilities with cracks in ceramics, in: *Science of Ceramics*. pp. 349–360.
- Bradt, R.C., 2004. Fracture of refractories, in: *Refractories Handbook*. CRC Press, pp. 11–38.
- Brémand, F., Cottron, M., Doumalin, P., Dupre, J.C., Germaneau, A., Valle, V., 2011. Mesures en mécanique par méthodes optiques. *Tech. Ing.* R1850.

- Bretagne, N., Valle, V., Dupré, J.-C., 2005a. Recent developments of the mark tracking technique: application to strain field and volume variation measurements. *NDT E Int.* 38/4, 290–298.
- Bretagne, N., Valle, V., Dupré, J.C., 2005b. Development of the marks tracking technique for strain field and volume variation measurements. *NDT E Int.* 38, 290–298.
- Brühwiler, E., Wittmann, F.H., 1990. The wedge splitting test, a new method of performing stable fracture mechanics tests. *Eng. Fract. Mech.* 35, 117–125.
- Buessem, W.R., Thielke, N.R., Sarakauskas, R.V., 1952. Thermal expansion hysteresis of aluminum titanate. *Ceram. Age* 60, 38.
- Carneiro, F.L.L.B., 1943. A new method to determine the tensile strength of concrete, in: *Proceedings of the 5th Meeting of the Brazilian Association for Technical Rules.* pp. 126–129.
- Chen, R., Dai, F., Qin, J., Lu, F., 2013. Flattened Brazilian disc method for determining the dynamic tensile stress-strain curve of low strength brittle solids. *Exp. Mech.* 53, 1153–1159.
- Chevalier, L., Calloch, S., Hild, F., Marco, Y., 2001. Digital image correlation used to analyze the multiaxial behavior of rubber-like materials. *Eur. J. Mech. ASolids* 20, 169–187.
- Chiang, F.-P., 2008. Micro-/nano-speckle method with applications to materials, tissue engineering and heart mechanics. *Strain* 44, 27–39.
- Cho, S., Chasiotis, I., Friedmann, T.A., Sullivan, J.P., 2005. Young's modulus, Poisson's ratio and failure properties of tetrahedral amorphous diamond-like carbon for MEMS devices. *J. Micromechanics Microengineering* 15, 728.
- Chu, T.C., Ranson, W.F., Sutton, M.A., 1985. Applications of digital-image-correlation techniques to experimental mechanics. *Exp. Mech.* 25, 232–244.
- Cooreman, S., Lecompte, D., Sol, H., Vantomme, J., Debruyne, D., 2008. Identification of mechanical material behavior through inverse modeling and DIC. *Exp. Mech.* 48, 421–433.
- Darvell, B.W., 1990. Uniaxial compression tests and the validity of indirect tensile strength. *J. Mater. Sci.* 25, 757–780.
- Decultot, N., 2009. Formage incrémental de tôle d'aluminium : étude du procédé à l'aide de la mesure de champs et identification de modèles de comportement (PhD thesis). Université Paul Sabatier – Toulouse 3.
- Doncieux, A., Stagnol, D., Huger, M., Chotard, T., Gault, C., Ota, T., Hashimoto, S., 2008. Thermo-elastic behaviour of a natural quartzite: Itacolumite. *J. Mater. Sci.* 43, 4167–4174.
- Doumalin, P., 2000. Microextensométrie locale par corrélation d'images numériques ; Application aux études micromécaniques par microscopie électronique à balayage (PhD thesis). Ecole Polytechnique, France.
- Dusseault, M.B., 1980. Itacolumites: the flexible sandstones. *Q. J. Eng. Geol.* 13, 119–128.
- Dusserre, G., Nazaret, F., Robert, L., Cutard, T., 2013. Applicability of image correlation techniques to characterise asymmetric refractory creep during bending tests. *J. Eur. Ceram. Soc.* 33, 221–231.
- Evans, A.G., 1990. Perspective on the development of high-toughness ceramics. *J. Am. Ceram. Soc.* 73, 187–206.
- Fairhurst, C., 1964. On the validity of the "Brazilian" test for brittle materials. *Int. J. Rock Mech. Min. Sci. Geomech. Abstr.* 1, 535–546.
- Feissel, P., Henry, J., Aboura, Z., Villon, P., 2012. Strain reconstruction from DIC through diffuse approximation - Application to damage detection, in: *Proceedings of the 15th ECCM European Conference on Composite Materials.* Venice, Italy.



- Feissel, P., Schneider, J., Aboura, Z., 2009. Estimation of the strain field from full-field displacement noisy data: filtering through Diffuse Approximation and application to interlock graphite/epoxy composite, in: Proceedings ICCM17, International Conferences on Composite Materials. Edinburgh, Scotland, pp. 27–31.
- Feissel, P., Schneider, J., Aboura, Z., Villon, P., 2013. Use of diffuse approximation on DIC for early damage detection in 3D carbon/epoxy composites. *Compos. Sci. Technol.* 88, 16–25.
- Forman, M., 1966. Experimental program to determine effect of crack buckling and specimen dimensions on fracture toughness of thin sheet materials (Technical report No. AFFDL-TR-65-146).
- Gallet-Doncieux, A., Michaud, P., Huger, M., Chotard, T., Ishizawa, N., Ota, T., 2011. Characterization of the anisotropic grain coarsening, in: Proceedings UNITECR 2011, Kyoto. Japon, p. 114.
- Gaudette, G.R., Todaro, J., Krukenkamp, I.B., Chiang, F.-P., 2001. Computer aided speckle interferometry: a technique for measuring deformation of the surface of the heart. *Ann. Biomed. Eng.* 29, 775–780.
- Ghosh, A., Sarkar, R., Mukherjee, B., Das, S.K., 2004. Effect of spinel content on the properties of magnesia-spinel composite refractory. *J. Eur. Ceram. Soc.* 24, 2079–2085.
- Gogotsi, G.A., 1993. The significance of non-elastic deformation in the thermal shock fracture of heterogeneous ceramic materials, in: Schneider, D.G.A., Petzow, P.D.D. (Eds.), *Thermal Shock and Thermal Fatigue Behavior of Advanced Ceramics*, NATO ASI Series. Springer Netherlands, pp. 279–291.
- Gogotsi, G.A., Groushevsky, Y.L., Strellov, K.K., 1978. The significance of non-elastic deformation in the fracture of heterogeneous ceramic materials. *Ceramurg. Int.* 4, 113–118.
- Grasset-Bourdel, R., 2011. Structure/property relations of magnesia-spinel refractories: experimental determination and simulation (PhD thesis). Université de Limoges.
- Grédiac, M., Hild, F., 2011. Mesures de champs et identification en mécanique des solides. Lavoisier.
- Green, D.J., 1998. An introduction to the mechanical properties of ceramics. Cambridge University Press.
- Guinea, G.V., El-Sayed, K., Rocco, C.G., Elices, M., Planas, J., 2002. The effect of the bond between the matrix and the aggregates on the cracking mechanism and fracture parameters of concrete. *Cem. Concr. Res.* 32, 1961–1970.
- Guo, H., Aziz, N.I., Schmidt, L.C., 1993. Rock fracture-toughness determination by the Brazilian test. *Eng. Geol.* 33, 177–188.
- Haddadi, H., Belhabib, S., Gaspérini, M., Vacher, P., 2005. Identification of the parameters of swift law using strain field measurements, in: Proceeding 8th European Mechanics of Materials Conference on Material and Structural Identification from Full-Field Measurements.
- Harmuth, H., Rieder, K., Krobath, M., Tschegg, E., 1996. Investigation of the nonlinear fracture behaviour of ordinary ceramic refractory materials. *Mater. Sci. Eng. A* 214, 53–61.
- Harmuth, H., Tschegg, E.K., 1997. A fracture mechanics approach for the development of refractory materials with reduced brittleness. *Fatigue Fract. Eng. Mater. Struct.* 20, 1585–1603.
- Hasselmann, D.P.H., 1963. Elastic energy at fracture and surface energy as design criteria for thermal shock. *J. Am. Ceram. Soc.* 46, 535–540.

- Hasselmann, D.P.H., 1969. Unified theory of thermal shock fracture initiation and crack propagation in brittle ceramics. *J. Am. Ceram. Soc.* 52, 600–604.
- Hiramatsu, Y., Oka, Y., 1966. Determination of the tensile strength of rock by a compression test of an irregular test piece. *Int. J. Rock Mech. Min. Sci. Geomech. Abstr.* 3, 89–90.
- Hobbs, D.W., 1965. An assessment of a technique for determining the tensile strength of rock. *Br. J. Appl. Phys.* 16, 259.
- Homeny, J., Bradt, R.C., 1985. Aggregate distribution effects on the mechanical properties and thermal shock behavior of model monolithic refractory systems., in: *Advances in Ceramics*. pp. 110–130.
- Huang, S.-H., Lin, L.-S., Fok, A.S.L., Lin, C.-P., 2012. Diametral compression test with composite disk for dentin bond strength measurement – Finite element analysis. *Dent. Mater.* 28, 1098–1104.
- Huger, M., Tessier-Doyen, N., Chotard, T., Gault, C., 2007. Microstructural effects associated to CTE mismatch for enhancing the thermal shock resistance of refractories: Investigation by high temperature ultrasounds. *CFI Ceram. Forum Int.* 84, E93–E102.
- Irwin, G.R., Kies, J.R., 1954. *Welding research supplement* 19, 193–198.
- Jianhong, Y., Wu, F.Q., Sun, J.Z., 2009. Estimation of the tensile elastic modulus using Brazilian disc by applying diametrically opposed concentrated loads. *Int. J. Rock Mech. Min. Sci.* 46, 568–576.
- Jonsén, P., Häggblad, H.-Å., Sommer, K., 2007. Tensile strength and fracture energy of pressed metal powder by diametral compression test. *Powder Technol.* 176, 148–155.
- Jonsson, F., Johnson, D., 2007. Finite element model updating of the New Svinesund bridge (Master's Thesis). Chalmers University Of Technology, Göteborg, Sweden.
- Kachanov, L.M., 1958. On time to rupture in creep conditions (in russian). *Izvestia Akad. Nauk SSSR Otd. Tekhnicheskikh Nauk* 8, 26–31.
- Kakroudi, M.G., 2007. Comportement thermomécanique en traction de bétons réfractaires : influence de la nature des agrégats et de l'histoire thermique (PhD thesis). Université de Limoges.
- Kamio, H., 2011. Digital image correlation method for analyzing the deformation behavior of the refractories, in: *Proceedings UNITECR 2011*. pp. 689–692.
- Kamio, H., Sasatani, Y., Sugawara, M., 2011. Analyses of the thermal deformation behavior of the Al<sub>2</sub>O<sub>3</sub>-MgO castables by digital image correlation method, in: *Proceedings UNITECR 2011*. pp. 512–515.
- Kavanagh, K.T., Clough, R.W., 1971. Finite element applications in the characterization of elastic solids. *Int. J. Solids Struct.* 7, 11–23.
- Kim, I.J., 2010. Thermal stability of Al<sub>2</sub>TiO<sub>5</sub> ceramics for new diesel particulate filter applications-A literature review. *J. Ceram. Process. Res.* 11, 411–418.
- Kingery, W.D., 1955. Factors affecting thermal stress resistance of ceramic materials. *J. Am. Ceram. Soc.* 38, 3–15.
- Laszlo, F., 1943. Tessellated stresses. *J. Iron Steel Inst.* 147, 173.
- Lauta, F.J., Steigerwald, E.A., 1965. Influence of work of hardening coefficient on crack propagation in high-strength steels. *Tech. Rep. AFML-TR-65-31* Air Force Mater. Lab.
- Lecompte, D., 2007. Elastic and elasto-plastic material parameter identification by inverse modeling of static tests using digital image correlation (PhD thesis). Ecole polytechnique de Bruxelles.
- Lecompte, D., Smits, A., Bossuyt, S., Sol, H., Vantomme, J., Van Hemelrijck, D., Habraken, A.M., 2006. Quality assessment of speckle patterns for digital image correlation. *Opt. Lasers Eng.* 44, 1132–1145.

- Lee, W.E., Zhang, S., 1999. Melt corrosion of oxide and oxide–carbon refractories. *Int. Mater. Rev.* 44, 77–104.
- Lemaitre, J., Chaboche, J.-L., 1990. *Mechanics of solid materials*. Cambridge University Press, Cambridge.
- Leplay, P., 2011. *Identification de comportements mécaniques et à rupture par corrélation d'images 2D et 3D : Application aux filtres à particules Diesel à base de titanate d'aluminium* (PhD thesis). Université de Lyon.
- Leplay, P., Réthoré, J., Meille, S., Baietto, M.-C., 2010. Damage law identification of a quasi brittle ceramic from a bending test using Digital Image Correlation. *J. Eur. Ceram. Soc.* 30, 2715–2725.
- Leplay, P., Réthoré, J., Meille, S., Baietto, M.-C., 2012. Identification of asymmetric constitutive laws at high temperature based on Digital Image Correlation. *J. Eur. Ceram. Soc.* 32, 3949–3958.
- Liu, G., Li, N., Yan, W., Tao, G., Li, Y., 2012. Composition and structure of a composite spinel made from magnesia and hercynite. *J. Ceram. Process. Res.* 13, 480–485.
- Löfgren, I., Stang, H., Olesen, J.F., 2007. The WST method, a fracture mechanics test method for FRC. *Mater. Struct.* 41, 197–211.
- Lyons, J.S., Liu, J., Sutton, M.A., 1996. High-temperature deformation measurements using digital-image correlation. *Exp. Mech.* 36, 64–70.
- Marshall, D.B., Swain, M.V., 1988. Crack resistance curves in magnesia-partially-stabilized zirconia. *J. Am. Ceram. Soc.* 71, 399–407.
- Marzagui, H., 2005. *Etude de deux bétons réfractaires silico-alumineux : microstructures et comportements thermomécaniques en traction et en flexion* (PhD thesis). Université de Toulouse III.
- Mat, Y., Lawn, B.R., 1986. Crack stability and toughness characteristics in brittle materials. *Annu. Rev. Mater. Sci.* 16, 415–439.
- McNeill, S.R., Peters, W.H., Sutton, M.A., 1987. Estimation of stress intensity factor by digital image correlation. *Eng. Fract. Mech.* 28, 101–112.
- Norton, F.H., 1925. A General Theory of Spalling. *J. Am. Ceram. Soc.* 8, 29–39.
- Orteu, J.-J., Cutard, T., Garcia, D., Cailleux, E., Robert, L., 2007. Application of stereovision to the mechanical characterisation of ceramic refractories reinforced with metallic fibres. *Strain* 43, 96–108.
- PEM, 2015. *Photomécanique & analyse Expérimentale en Mécanique des solides – PEM* <http://www.pprime.fr/?q=fr/recherche-scientifique/d3/photomecanique>.
- Périer, J.-N., Calloch, S., Cluzel, C., Hild, F., 2002. Analysis of a multiaxial test on a C/C composite by using digital image correlation and a damage model. *Exp. Mech.* 42, 318–328.
- Peruzzi, S., 2000. *Simulation numérique du comportement thermomécanique de pièces réfractaires de coulée continue* (PhD thesis). Université de Limoges.
- Peters, W.H., Ranson, W.F., 1982. Digital imaging techniques in experimental stress analysis. *Opt. Eng.* 21, 213427.
- Peters, W.H., Ranson, W.F., Sutton, M.A., Chu, T.C., Anderson, J., 1983. Application Of Digital Correlation Methods To Rigid Body Mechanics. *Opt. Eng.* 22, 226738.
- Pop, O., 2013. *Caractérisation du comportement en fissuration des milieux isotropes et orthotropes par couplage méthodes optiques-éléments finis* (Habilitation à diriger des recherches HDR). Limoges.
- Popov, E.P., 1999. *Engineering mechanics of solids*. Prentice Hall.
- Pottier, T., 2010. *Identification paramétrique par recalage de modèles éléments finis couplée à des mesures de champs cinématiques et thermiques* (PhD thesis). Université de Savoie.

- Ribeiro, S., Rodrigues, J.A., 2010. The influence of microstructure on the maximum load and fracture energy of refractory castables. *Ceram. Int.* 36, 263–274.
- Robert, L., Nazaret, F., Cutard, T., Orteu, J.-J., 2007. Use of 3-D digital image correlation to characterize the mechanical behavior of a fiber reinforced refractory castable. *Exp. Mech.* 47, 761–773.
- Robin, J.M., Berthaud, Y., Schmitt, N., Poirier, J., Themines, D., 1998. Thermomechanical behaviour of magnesia-carbon refractories. *Br. Ceram. Trans.* 97, 1–11.
- Rodríguez, J., Navarro, C., Sánchez-Gálvez, V., 1994. Splitting tests: an alternative to determine the dynamic tensile strength of ceramic materials. *J. Phys. IV* 04, C8–101–C8–106.
- Rotinat, R., Tié, R., Valle, V., Dupré, J. -C., 2001. Three optical procedures for local large-strain measurement. *Strain* 37, 89–98.
- Roux, S., Hild, F., 2006. Stress intensity factor measurements from digital image correlation: post-processing and integrated approaches. *Int. J. Fract.* 140, 141–157.
- Saadaoui, M., 1991. Etude de la résistance à la propagation de fissures dans les céramiques monolithiques de types alumine et zircon (PhD thesis). Institut National des Sciences Appliquées de Lyon.
- Sabate, N., Vogel, D., Gollhardt, A., Keller, J., Cane, C., Gracia, I., Morante, J.R., Michel, B., 2007. Residual Stress Measurement on a MEMS Structure With High-Spatial Resolution. *J. Microelectromechanical Syst.* 16, 365–372.
- Sabate, N., Vogel, D., Gollhardt, A., Marcos, J., Gracia, I., Cane, C., Michel, B., 2006. Digital image correlation of nanoscale deformation fields for local stress measurement in thin films. *Nanotechnology* 17, 5264.
- Sjödahl, M., Benckert, L.R., 1993. Electronic speckle photography: analysis of an algorithm giving the displacement with subpixel accuracy. *Appl. Opt.* 32, 2278–2284.
- Steinbrech, R.W., 1992. Toughening mechanisms for ceramic materials. *J. Eur. Ceram. Soc.* 10, 131–142.
- Sun, Z., Lyons, J.S., McNeill, S.R., 1997. Measuring microscopic deformations with digital image correlation. *Opt. Lasers Eng.* 27, 409–428.
- Sutton, M.A., Mingqi, C., Peters, W.H., Chao, Y.J., McNeill, S.R., 1986. Application of an optimized digital correlation method to planar deformation analysis. *Image Vis. Comput.* 4, 143–150.
- Tessier-Doyen, N., Glandus, J.C., Huger, M., 2006. Untypical Young's modulus evolution of model refractories at high temperature. *J. Eur. Ceram. Soc.* 26, 289–295.
- Tschegg, E.K., 1986. Equipment and appropriate specimen shapes for tests to measure fracture values. Austrian Pat. Off., Austrian Patent Office AT no. 390328.
- Wachtman, J.B., Cannon, W.R., Matthewson, M.J., 2009. *Mechanical properties of ceramics*. John Wiley & Sons.
- Wang, Q., Jia, X., Kou, S., Zhang, Z., Lindqvist, P., 2004. The flattened Brazilian disc specimen used for testing elastic modulus, tensile strength and fracture toughness of brittle rocks: analytical and numerical results. *Int. J. Rock Mech. Min. Sci.* 41, 245–253.
- Wang, T., Yamaguchi, A., 2001. Oxidation protection of MgO–C refractories by means of Al<sub>8</sub>B<sub>4</sub>C<sub>7</sub>. *J. Am. Ceram. Soc.* 84, 577–582.
- Wattrisse, B., Chrysochoos, A., Muracciole, J.-M., Némoz-Gaillard, M., 2001. Analysis of strain localization during tensile tests by digital image correlation. *Exp. Mech.* 41, 29–39.
- Xiang, G.F., Zhang, Q.C., Liu, H.W., Wu, X.P., Ju, X.Y., 2007. Time-resolved deformation measurements of the Portevin–Le Chatelier bands. *Scr. Mater.* 56, 721–724.

- Zhang, D., Luo, M., Arola, D.D., 2006. Displacement/strain measurements using an optical microscope and digital image correlation. *Opt. Eng.* 45, 033605–9.
- Zhang, D., Zhang, X., Cheng, G., 1999. Compression strain measurement by digital speckle correlation. *Exp. Mech.* 39, 62–65.
- Zhang, S., Lee, W., 2004. Spinel-containing refractories, in: *Refractories Handbook*. CRC Press, pp. 215–257.

## Abstract:

The present thesis aimed to apply digital image correlation (DIC) used for kinematic fields' measurements as a support for the experimental characterization of refractory materials with specific non-linear behaviour. Model and industrial materials with different degrees of flexibility were studied. The first type of materials was a single phase model flexible aluminium titanate material (AT VF) developed for academic purposes by improving the grain growth. Its non-linear mechanical behaviour was obtained thanks to the thermal expansion mismatch of its grains according to the different crystallographic axis. The second one is multi-phased magnesia based industrial materials, whose flexibility is less accentuated, and for which the non-linear mechanical behaviour is obtained thanks to the thermal expansion coefficients mismatch between spinel aggregates and magnesia matrix. In order to apply the optical methods on these materials which exhibit lower strain-to-rupture, it was necessary to optimize the accuracy of these techniques by improving experimental conditions.

In the case of AT VF, DIC and mark tracking method have been applied on four-points bending test at room temperature to underline the material asymmetric mechanical behaviour which induces a significant shift of the neutral fibre and to evaluate the relative displacement of rolls. The application of DIC has been extended to other experimental testing method such as Brazilian and Wedge Splitting test using the multi-phased magnesia based materials. This highlighted fracture mechanisms (crack occurrence and propagation) and the presence of crack branching phenomenon promoted thanks to an initial micro-cracks network voluntarily introduced by thermal expansion mismatch between the different phases so as to improve their thermal shock resistance. From displacement experimentally obtained by DIC, a finite element method updating (FEMU-U) has been developed to determine material properties.

Keywords: Digital image correlation, Refractories, Thermal shock resistance, Asymmetric non-linear mechanical behaviour, Aluminium titanate, Crack branching phenomenon, Magnesia-spinel materials, Finite element method updating.

## Résumé:

Cette thèse avait pour objectif de mettre en place et d'appliquer les techniques de mesure de champs de déplacements et de déformations (corrélation d'images numériques CIN) pour caractériser le comportement mécanique non linéaire de matériaux réfractaires. L'étude a été réalisée sur différents types de matériaux présentant des degrés variables de flexibilité : un matériau modèle monophasé à base de titanate d'aluminium (TA VF) et des matériaux industriels multi-phasés à base de magnésie. La flexibilité dans le cas du TA VF est obtenue grâce à l'anisotropie de la dilatation thermique entre les trois axes cristallographiques, et dans le cas des matériaux industriels grâce à la différence de coefficients de dilatation entre les agrégats de spinelle et la matrice magnésienne. Ces matériaux industriels ayant une déformation à rupture plus faible, la technique de corrélation d'images a dû être optimisée en ajustant au mieux les conditions expérimentales.

La CIN et la méthode de suivi de marqueurs ont permis de mettre en évidence le caractère dissymétrique du comportement mécanique en flexion du TA VF entre la zone de l'éprouvette sollicitée en traction et celle en compression et d'investiguer le déplacement relatif des rouleaux du dispositif de flexion. Cette dissymétrie de comportement engendre un déplacement progressif de la fibre neutre au fur et à mesure que la charge appliquée augmente. Cette technique a ensuite été étendue à d'autres essais tels que l'essai brésilien et le Wedge Splitting appliqués aux matériaux industriels magnésiens. La CIN a ainsi permis d'illustrer les mécanismes de rupture (initiation et propagation de fissures) et de mettre en évidence la présence de phénomènes de « crack branching » obtenus grâce au réseau initial de microfissures volontairement généré au sein du matériau par différentiel de dilatation entre phases dans le but d'améliorer sa résistance aux chocs thermiques. Enfin, à partir des champs de déplacements obtenus par corrélation d'images, la méthode de recalage par éléments finis a été développée et utilisée pour déterminer l'évolution des propriétés élastiques du matériau pendant l'essai.

Mots clés: Corrélation d'images numériques, Matériaux réfractaires, Résistance aux chocs thermiques, Comportement non linéaire dissymétrique, Titanate d'aluminium, phénomène de « Crack Branching », Magnésie spinelle, Méthode de recalage par éléments finis.

La durabilité de matériaux réfractaires par rapport à leur environnement de travail est aujourd'hui un défi à la fois technologique et économique majeur. Par la nature de leurs domaines d'application les matériaux réfractaires sont souvent soumis à des sollicitations thermomécaniques cycliques extrêmes et/ou à des agents fortement agressifs de l'environnement de travail. Parmi les domaines d'applications, nous pouvons rappeler ici l'utilisation de matériaux réfractaires comme revêtements de fours rotatifs de cimenterie ou en sidérurgie, applications dans lesquels la température d'utilisation peut atteindre  $1450\text{ }^{\circ}\text{C} - 1700\text{ }^{\circ}\text{C}$ . L'industrie automobile est un autre domaine qui utilise ces matériaux dans fabrication de filtres à particules. Cette multitude d'applications techniques nécessite d'orienter l'élaboration du matériau réfractaire en conformité avec les exigences d'un cahier de charge strict en termes de réfractarité, tenue à la corrosion et résistance aux chocs thermiques. Cette dernière propriété, qui est fortement reliée aux mécanismes de fissuration, est parmi les paramètres clefs de l'optimisation de la durée de vie de ces matériaux. C'est pour cette raison que la génération volontaire d'un réseau de microfissures au sein de la microstructure en jouant sur les coefficients de dilatations va permettre d'obtenir un comportement mécanique non-linéaire caractérisé par une faible contrainte et une forte déformation à la rupture. Ces deux paramètres sont primordiaux dans l'amélioration de la résistance aux chocs thermiques et permettent de retarder la dégradation du matériau. D'où l'intérêt d'étudier ce comportement mécanique non-linéaire. Jusqu'à présent, la caractérisation de ce type de comportement se fait dans certains laboratoires en utilisant des essais uniaxiaux qui sont valides uniquement pour des matériaux dont le comportement mécanique est linéaire élastique afin de déterminer les lois de comportement qui seront utilisées par la suite dans le calcul par éléments finis. Ces essais consomment un temps fastidieux pour la préparation et la mise en place des éprouvettes. C'est pour cette raison, que l'apparition des méthodes optiques telles que la corrélation d'images

numériques (CIN) a permis de faire réfléchir par rapport à la caractérisation des comportements mécaniques non-linéaires.

Cette thèse avait pour objectif de mettre en place et d'appliquer les techniques de mesure de champs de déplacements et de déformations telles que la CIN pour caractériser le comportement mécanique non linéaire de différents matériaux réfractaires à faible déformation à la rupture, présentant des degrés variables de flexibilité : un matériau modèle monophasé à base du titanate d'aluminium (TA) et des matériaux industriels à base de magnésie spinelle (MSp).

Le TA est utilisé dans plusieurs applications dans l'industrie automobile pour sa bonne résistance aux chocs thermiques à des températures inférieures à 1000 °C. Cette propriété est obtenue grâce à l'anisotropie des coefficients de dilatations suivant les 3 axes cristallographiques. Dans le cadre d'une collaboration avec NITECH au Japon, différentes nuances du TA ont été développées en travaillant sur les conditions de préparation. Parmi ces nuances, le TA VF (TA très flexible) a été choisi pour cette étude. La magnésie pure est réputée pour sa bonne résistance à la corrosion, par contre, sa résistance aux chocs demeure moyenne, c'est pour cette raison que l'incorporation des grains de spinelle permet d'améliorer leur résistance aux chocs thermiques permettant ainsi de prolonger deux fois la durée de vie des fours rotatifs à ciment et de remplacer les matériaux à base de chrome qui sont interdits pour des raisons environnementales. La flexibilité de ces matériaux est obtenue grâce à la différence de coefficients de dilatation entre les agrégats de spinelle et la matrice magnésienne. Différents essais ont été utilisés et mis en place pour évaluer le comportement mécanique de ces matériaux, certains d'entre eux sont connus dans le domaine des matériaux tels que l'essai de flexion 4 points, d'autres le sont moins tels que l'essai brésilien et l'essai du Wedge Splitting. Ces différentes techniques ont été associées à la CIN qui permet d'obtenir les champs de déformations et de déplacements à la surface du matériau. Ce travail a été réalisé avec une



étroite collaboration avec l'équipe Photomechanics & Experimental Mechanics de l'institut Pprime de l'université de Poitiers.

Le développement des méthodes optiques de mesures de déplacements et de déformations est d'une grande importance dans la caractérisation du comportement mécanique des matériaux hétérogènes à différentes échelles.

Parmi les techniques optiques utilisées, la méthode de corrélation d'images numériques CIN (Digital image correlation DIC), apparue au début des années 80 grâce à Chu et Sutton, connaît un développement remarquable et n'arrête pas de séduire les mécaniciens des solides en général et les chercheurs et les industriels dans le monde des réfractaires en particulier.

C'est une technique réputée par sa rapidité, sa précision et son économie. Elle exploite des images numériques issues majoritairement des moyens d'acquisitions optiques sans contact qui sont devenus de plus en plus performants et moins coûteux. A titre d'exemple, certains d'entre eux peuvent présenter une bonne tolérance aux conditions agressives telles que la variation de la température. D'autres peuvent être utilisées suivant une gamme d'échelle de temps très large et permettent l'acquisition d'une image par un millier de seconde voire une microseconde. En plus, grâce à des systèmes multi caméras, on peut accéder au champ de déplacement tridimensionnel à la surface d'un objet (la stéréo corrélation) ou encore à des images tridimensionnelles de tomographie.

La corrélation d'images numériques repose sur le principe que la quantité imagée est associée à une propriété physique de la matière de la zone étudiée.

En effet, les données d'entrée de cette technique sont des niveaux de gris (valeurs entières positives) de deux images numériques de la partie du matériau étudié. Une image de référence qui correspond à un état non déformé, et une seconde qui correspond à un état déformé.

Le principe de la CIN est de comparer le degré de similarité entre les différentes images de la surface du matériau acquises en utilisant une caméra numérique lors d'un essai mécanique.

Ces images sont comparées avec l'image de référence qui correspond à un état auquel le matériau est au repos.

Un grand intérêt est porté à la texture de la surface filmé du matériau qui doit satisfaire certains critères. En effet, chaque élément de la surface doit avoir une texture ou une signature unique. De plus, comme l'identification a lieu grâce aux niveaux de gris des pixels, il faut que les niveaux de gris aient une large dynamique couvrant le mieux possible la profondeur des niveaux de gris de l'encodage des images. Il est préférable aussi que l'image présente un fort contraste d'un pixel à l'autre pour pouvoir être sensible à de faibles déplacements.

Dans certains cas, il est possible d'appliquer la méthode directement en utilisant la texture naturelle du matériau si elle satisfait ces deux hypothèses. Par contre l'existence d'un tel contraste n'est toutefois pas garantie. Afin de résoudre le problème, une préparation artificielle de la surface des éprouvettes appelée « mouchetis » a lieu sur la surface à l'aide d'une bombe aérosol, d'un aérographe ou d'autres moyens. Pour ceci, une couche de peinture noire (ou blanche) est déposée sur la surface de l'éprouvette et après séchage, des gouttelettes fines de peinture blanche (ou noire) sont déposées dessus pour garantir un bon contraste. Ceci peut être obtenu en utilisant des bombes à peinture ou un aérographe qui permet de former un aérosol dont la taille des gouttelettes peut être ajustée par une buse adaptée. Dans certains cas, comme des cas de forte déformabilité, le dépôt de poudre permet une bonne stabilité de la texture jusqu'à plusieurs centaines de pourcents de déformation.

La qualité et la précision des mesures de déplacements et des déformations de la corrélation d'images sont liées directement à la qualité des conditions expérimentales et au calcul numérique. En effet, avec de bonnes conditions expérimentales et un bon choix des paramètres de calcul, on peut mesurer des déplacements de l'ordre de  $1/100^{\text{ème}}$  à  $1/1000^{\text{ème}}$  de pixels.

D'une manière générale, nombreuses sont les sources d'erreurs qui affectent les résultats de corrélation d'images, parmi ces sources d'erreurs on peut citer :

- La préparation de la surface de l'échantillon
- Un défaut de parallélisme entre le capteur de la caméra CCD et la surface de l'échantillon et les déplacements hors plans
- Des bruits pendant l'enregistrement des images
- La taille des fenêtres de corrélation

Dans le cadre de la thèse aussi, la méthode de recalage par éléments finis a été développée. Cette technique permet de déterminer les propriétés des matériaux à partir des champs des déplacements obtenus par CIN. Le principe de la méthode est de comparer ces champs avec les champs de déplacements calculés par simulation avec un jeu initial de paramètres matériaux en utilisant une fonction objective. Si le résultat obtenu par cette fonction satisfait le critère de convergence, les paramètres utilisés pour la simulation vont correspondre aux paramètres matériaux, si non, un deuxième jeu de paramètres sera calculé en utilisant la méthode de Newton-Raphson.

La caractérisation du comportement mécanique non-linéaire du TA VF a été réalisée grâce à un essai de flexion 4-points en utilisant la corrélation d'images. L'évolution des champs de déformations a mis en évidence qu'au début de l'essai, il y'a un équilibre entre les efforts de traction et les efforts de compression. La fibre neutre de déformation nulle est représentée par le contour noir, qui malgré le bruit de mesure, est localisé au milieu de l'éprouvette. Au fur et à mesure que la charge appliquée va augmenter, la partie sous traction devient de plus en plus importante par rapport à la partie en compression jusqu'à l'amorçage de la fissure et sa propagation. D'un autre côté, la fibre neutre avait tendance à se déplacer vers le haut.

L'évolution de cette fibre neutre a été étudiée et comparée avec celle d'un matériau dont le comportement est linéaire élastique (aluminium) pour mettre en évidence le comportement non linéaire du TA VF.

Pendant ce test, les rouleaux du montage de flexion se déplacent. En effet, les rouleaux supérieurs ont tendance à se rapprocher contrairement aux rouleaux inférieurs à cause de la dissymétrie entre la traction et la compression. Ceci peut engendrer des erreurs de l'ordre de 2% sur les valeurs calculées des contraintes à rupture. Par contre, ce déplacement n'a pas d'influence significative sur le comportement dissymétrique du matériau.

A partir des champs de déplacements obtenus par CIN, la méthode de recalage par éléments finis a permis de mettre en évidence la diminution de la rigidité du matériau (module d'Young) au cours de cet essai à cause du réseau de microfissures qui s'est créé et s'est développé au fur et à mesure que la charge appliquée devient de plus en plus importante.

Après avoir mis en place la technique de corrélation d'images en utilisant un échantillon du TA VF, il a fallu optimiser la précision de mesure de cette dernière pour s'adapter au niveau de déformation de d'autres types de matériaux. La deuxième catégorie des matériaux de l'étude contient des matériaux à base de MgO-Spinelle dans le but d'étudier l'influence de la spinelle sur le comportement mécanique non-linéaire et les mécanismes de fissuration. Grâce à l'essai du Wedge splitting, nous avons confirmé que la spinelle dégrade la contrainte à rupture et augmente l'énergie de fissuration. Les valeurs élevées de l'énergie sont dues au réseau de microfissures créé pendant l'initiation et la propagation de la macrofissure.

Afin d'étudier la complexité de la microfissuration dans ces matériaux hétérogènes, la CIN a été appliquée sur ces matériaux pendant cet essai. Différentes cartographies de déformations à différents instants ont été représentées.

Contrairement à la MgO pure, nous constatons que dans le cas des matériaux à base de MgO-Spinelle, en plus des déformations liées à la propagation de la fissure principale, nous constatons la présence de déformations liées au réseau de microfissures créé et qui se développe

au fur et à mesure que la macrofissure se propage. C'est ce qu'on appelle le phénomène du « crack branching ».

Des échantillons de MgO-Spinelle ont été soumis à un essai brésilien. C'est un essai de compression diamétrale dans lequel les contraintes de compression vont se transformer en contraintes de traction au milieu de l'éprouvette. Ceci a été confirmé par la CIN.

Une analyse visuelle nous permet de dire que la fissure commence à partir des zones de contact et se propage. Grâce à la CIN, la déformation en traction qui apparaît au milieu de l'éprouvette a été mise en évidence par l'amorçage de la fissure et sa propagation jusqu'à la rupture du matériau. Les zones du matériau en contact avec les appuis sont soumises à la compression.